Title
Tackling Measurement Uncertainties in Field-effect Transistor-based Biosensors

Author
Gao, Wuran

Publication Date
2022

Peer reviewed|Thesis/dissertation

UNIVERSITY OF CALIFORNIA

Los Angeles

Tackling Measurement Uncertainties in Field-effect Transistor-based Biosensors

A dissertation submitted in partial satisfaction

of the requirements for the degree

Doctor of Philosophy in Electrical and Computer Engineering

by

Wuran Gao

2022

ABSTRACT OF THE DISSERTATION

Tackling Measurement Uncertainties in Field-effect Transistor-based Biosensors

by

Wuran Gao
Doctor of Philosophy in Electrical and Computer Engineering
University of California, Los Angeles, 2022
Professor Wentai Liu, Chair

Field-effect transistor (FET) based biosensors have emerged as a promising candidate to provide quick, convenient, accurate, and label-free biological analytes quantization outside conventional laboratories. They sense intrinsic charges carried by the target analytes and therefore avoid time-consuming sample labeling processing. Label-free detection of the specific target analytes is achieved by coupling immunological receptor probes with FET. They specifically capture the target analytes, change the surface charging state, and the underlying transistor transduces such surface charge into electrical signals that could be directly fed to an electronic readout system. Over the past decades, FET-based biosensors have demonstrated high sensitivity and low limit of detection (LLOD) in detecting a plethora of targets, including proteins, volatile organic compounds, nucleotides, and viruses.

Measurement uncertainties, the fluctuation of the measurable quantities, are crucial for high-performance biological assays. It must be kept small enough to allow the signal from ultra-low concentration target analytes to stand out of the background. Measurement uncertainties in FET-based biosensors originate from multiple sources, including noise, device instability, device-to-device variation, sample preparations, etc. Among these sources, noise

sets a fundamental lower limit of fluctuations for a specific device and shall be minimized. Meanwhile, other factors may contribute more significant measurement uncertainties than the characterized noise limit in practical analytical assays. The lack of understanding and control of the measurement uncertainty sources becomes one critical challenge preventing FET-based biosensors from generating larger impacts in the biomedical industry despite their tremendous success in research laboratories.

This dissertation is to enhance our understanding of measurement uncertainties in FET-based biosensors and propose strategies to mitigate them.

In the first part of this work, we analyzed the low-frequency noise of dual-gated silicon field-effect transistor (DG-FET) biosensors with Schottky contacts. We found the flicker noise at the sensing insulator-semiconductor interface to be the major noise source while employing Schottky contacts to have minimal noise contribution with a sufficiently large back-gate bias voltage. The measured noise dependence on transconductance further indicated the presence of non-uniform energy distribution of interface trap density at the said sensing interface. Based on these findings, we argued that the DG structure is advantageous over its single-gated (SG) counterpart – although they possess the same intrinsic LLOD, the former could offer a larger signal gain at the optimum LLOD thanks to sufficient channel carrier supply through back-gating instead of biasing the sensing interface toward band edge with higher trap density.

In the second part of this work, we studied the instability of the same DG-FET biosensor. FET biosensors are exposed to electrolyte solution and therefore more prone to device instability issues like characteristic drifting compared with conventional devices used in integrated circuits (IC), which are often well passivated from the ambient. Such time-varying behavior leads to a longer waiting time to stabilize the sensor as well as larger measurement uncertainties if multiple measurements are conducted. We analyzed the instability behavior observed in DG-FET sensing experiments and hypothesized it was a result of redistributed protons inside dielectrics at the silicon/oxide interface of the back-gate. Two improved mea-

surement techniques, pulsed IV and pulse resetting, were proposed and demonstrated to mitigate their effects in the measurement data.

In the third part of this work, we examined the nonlinearity in FET-based binding assay response. While the dose-response curve of an affinity-based bioanalytical assay generally shows a nonlinear relationship, any distortion due to the FET transducers has not been well understood. We showed that the nonlinear transduction mechanism of FET sensors plays an important role in shaping their dose-response curves when operating in the nonlinear regime. Negligence of such nonlinearity would introduce errors in the extracted affinity properties of the analyte-receptor pair. This work provides useful guidelines for designing FET-based binding assays and interpreting their measurement data.

The dissertation of Wuran Gao is approved.

Chi On Chui

Subramanian S. Iyer

Aydin Babakhani

Sam Emaminejad

Wentai Liu, Committee Chair

University of California, Los Angeles

2022

To my family,

who are always supportive,

To my lovely wife,

who lights up my life.

TABLE OF CONTENTS

LIST OF FIGURES

LIST OF TABLES

ACKNOWLEDGMENTS

I am forever indebted to my advisor Professor Chi On Chui whose support, guidance, and wisdom have guided my education and personal developments in the past eight years. The inspiration and encouragement from him have carried me through the challenging time of my graduate study. He sets an extraordinary example as a researcher, educator as well as a life mentor that I can always look up to.

I am sincerely grateful to Professor Wentai Liu for serving as my committee chair, and Professor Subramanian S. Iyer, Professor Sam Emaminejad, and Professor Aydin Babakhani for their time and efforts spent as part of my thesis committee and valuable advice to help my research advances.

I would like to thank Dr. Marko Sokolich and Dr. You-Sheng (Wilson) Lin for their guidance in my Teaching Apprenticeship at UCLA. I would also like to thank all Nanolab staff for their strong support in both my classes and research.

I would like to thank Deeona Columbia and the extraordinary team of the ECE Office of Graduate Student Affairs (ECEOGSA) who have always made themselves available to help graduate students like myself. I should give a special thank to Ryo Arreola who helped me arrange my qualification exam in the last minute. He has always been a professional supporter and a genuine friend. Too unfortunate he could not see my graduation. I will be ever grateful for his assistance.

I would like to acknowledge and thank all my wonderful labmates Dr. Andrew Pan, Dr. Yufei Mao, Dr. Kaveh Shoorideh, Dr. Ablaikhan Akhazhanov, and Xin Li, for their constant support and life sharing experience in my progress towards my Ph.D degree.

VITA

2014	B.S. in Electrical Engineering, Shanghai Jiao Tong University, Shanghai, China
2016	M.S. in Electrical Engineering, University of California Los Angeles, California
2015–2021	Graduate Student Researcher in Nanoelectronic Device and Technology Laboratory, University of California Los Angeles, California
2016–2021	Teaching Assistant (EE121DA, EE121DB: Semiconductor Processing and Device Design), University of California Los Angeles, Los Angeles, CA

PUBLICATIONS

W. Gao and C.O.Chui, "On Nonlinearity in Field-effect Transistor-based Binding Assay Response," *Applied Physics Letters*, vol. 120, no. 3, Jan. 2022, p. 033701.

W. Gao, Y. Mao, and C.O.Chui, "On Noise Performance of Dual-Gated Silicon FET Biosensors With Schottky Contacts," *IEEE Transactions on Electron Devices*, vol. 68, no. 6, May 2021, pp. 2965–2970.

L. Song, J. Chiang, **W. Gao**, and Y. Rahmat-Samii, "Liquid Metal-based Tunable Coaxial Antenna for Microwave Ablation", *Proceedings of the IEEE Antenna and Propagation Society International Symposium*, July 2020, pp. 1691-1692.

L. Song, **W. Gao**, and Y. Rahmat-Samii, "3D Printed Microfluidics Channelizing Liquid Metal for Multi-Polarization Reconfigurable Extended E-Shaped Patch Antenna," *IEEE Transactions on Antennas and Propagation*, vol. 68, no. 10, Oct. 2020, pp. 6867-6878.

L. Song, **W. Gao**, and Y. Rahmat-Samii, "3D Printing-based Liquid Metal Patch Antennas with Wide-Band Frequency and Multi-Polarization Reconfigurations", *International Symposium on Electromagnetic Theory*, 2019.

L. Song, **W. Gao**, C. O. Chui and Y. Rahmat-Samii, "Wideband Frequency Reconfigurable Patch Antenna With Switchable Slots Based on Liquid Metal and 3-D Printed Microfluidics," *IEEE Transactions on Antennas and Propagation*, vol. 67, no. 5, March 2019, pp. 2886–2895.

CHAPTER 1

Introduction

1.1 Field-effect Transistor as Biosensors

Quantitative assessment of chemical and biological species are essential tasks generating crucial information for clinical disease diagnosis, drug screening, public health, environmental biology, etc. Some of the established assay methodologies include liquid chromatography [1], surface plasma resonance (SPR) [2, 3], polymerase chain reaction (PCR) [4], and enzyme-linked immunoassays (ELISA) [5–7]. These conventional assays are sensitive but require highly trained personnel, sophisticated instrument, and sufficient power supplies in maintaining their performance. As of today, the majority high performance assays are running in biological laboratories at centralized medical centers. Collecting and transporting samples lead to delays which may affect the patient diagnosis and postpone the public response to emerging pathogenic threats. The prolonged transportation and storage of the specimen may also cause sample degradation and deteriorate their results. These disadvantages have been observed in the troubles of building the test capabilities in the COVID-19 pandemic that happened when this dissertation was written. While these limits in the current testing scheme may only hinder the reopening speed in developed societies, they have caused lives in resource-limited developing countries. At the same time, portable biosensors, for example, lateral flow assay (LFA), have low sensitivity and can not provide as accurate and valuable information for doctors and public health officials. Despite tremendous efforts by global researchers, reliable point-of-care testing (POCT) devices still have a wide performance gap compared with laboratory assays. New tools that could be quickly deployed to the field run

with less resources and provide sensitive detecting results are critical to form a de-centralized medical system and save lives in the future [8].

Field-effect transistor (FET)-based biosensors could be a good candidate to fulfill such a vision in providing a rapid low-cost accurate biological analyte quantization in resource-limited locations. These sensors evolved from conventional metal-oxide-semiconductor FET (MOSFET) by replacing its metal (or polysilicon) gate terminal with a reference electrode in the electrolyte, as shown in Fig. 1.1. Electrical current flows between the source and drain

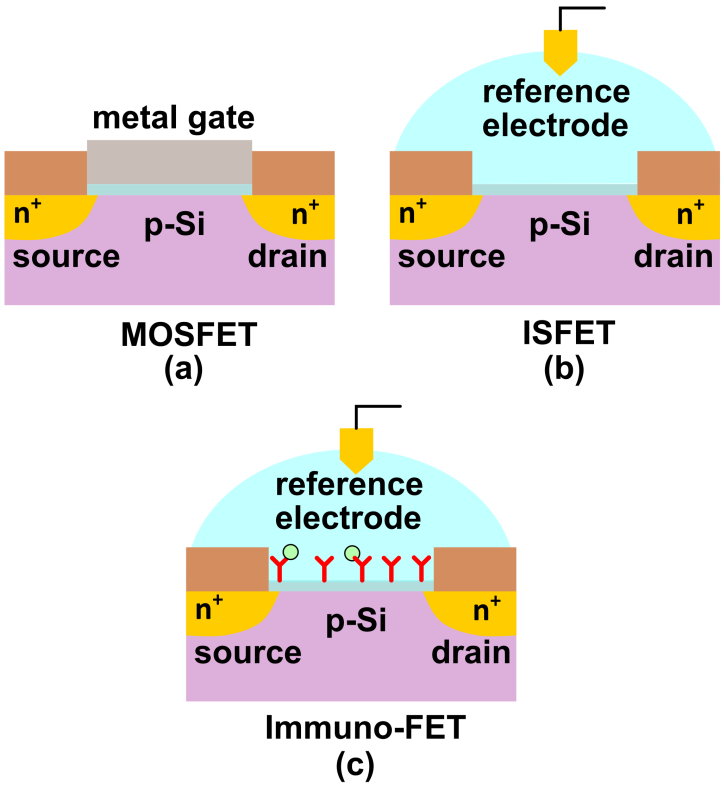

Figure 1.1: Schematic representation of a (a) MOSFET, (b) ISFET, and (c) ImmunoFET.

terminals when a conduction channel is formed at the dielectric-semiconductor interface under the appropriate gate bias. The channel conductivity is electrostatically controlled by the gate terminal voltage through the field across the insulating dielectric layer. For an

n-type MOSFET operated in its linear regime, the drain current I_D is

$$I_D = C_{ox}\mu_n \frac{W}{L}\left[(V_{GS} - V_{th})V_{DS} - \frac{1}{2}V_{DS}^2\right], \tag{1.1}$$

where C_{ox} is the gate capacitance per unit area, μ_n is the electron mobility, and W and L are the width and length of the channel, respectively. V_{th} is the threshold voltage and could be written as:

$$V_{th} = \frac{\phi_M - \phi_{Si}}{q} - \frac{Q_{ox} + Q_{it} + Q_D}{C_{ox}} + 2\psi_B, \tag{1.2}$$

where ϕ_M and ϕ_{Si} are the work function of the metal gate and semiconductor bulk, respectively, Q_{ox} is total oxide charge density in the gate dielectric, Q_{it} is the dielectric-semiconductor interface charge density, and Q_D is the depletion region charge, ψ_B is the built-in potential of the substrate. The MOSFET has a constant threshold as its geometry and doping profiles are fixed for a specific design. Its current is uniquely controlled by the electrical biases as intended for designing integrated circuits.

Once the metal gate is replaced with a reference electrode, the threshold voltage becomes sensitive to the electrochemical system formed by the reference electrode, electrolyte, and dielectric insulator. On the basis of electrochemistry, we could write its threshold voltage as:

$$V_{th} = E_{ref} + \chi^{sol} - \psi_0 - \frac{\phi_{Si}}{q} - \frac{Q_{ox} + Q_{it} + Q_D}{C_{ox}} + 2\psi_B, \tag{1.3}$$

where E_{ref} is the reference electrode potential, ψ_0 is the interface potential at the dielectric-electrolyte interface, χ^{sol} is the surface dipole momentum across the reference electrode and electrolyte. We can treat $E_{ref} + \chi^{sol} - \psi_0$ as the effective work function determined by the electrochemical system. The first embodiment of such a FET sensor was the ion-sensitive FET (ISFET), of which the interface potential ψ_0 was designed to be sensitive to the bulk hydrogen ion activity, i.e.,its pH values. Physically, the surface hydroxyl groups on the dielectric surface maintain a chemical equilibrium with the hydrogen ions through protonation and deprotonation that leads to different surface charge density and therefore

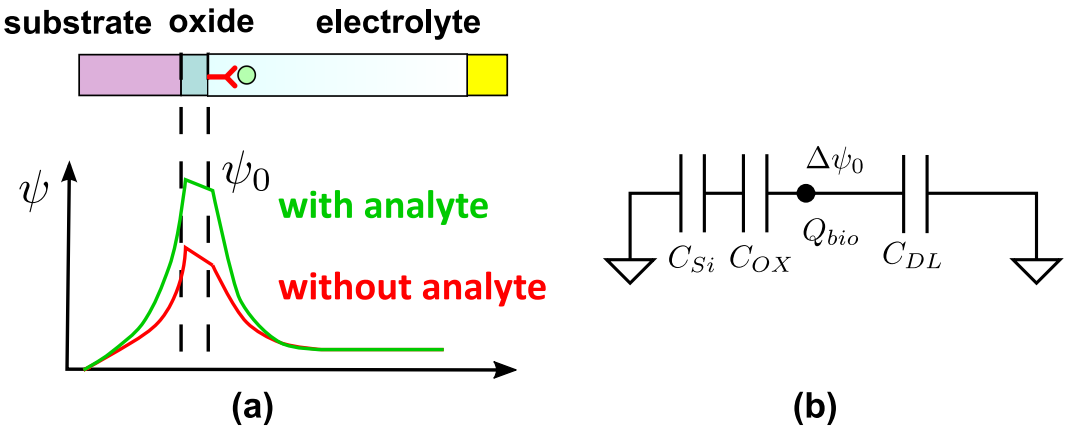

Figure 1.2: Detection principle of FET biochemical sensors.

interface potentials $\Delta\psi_0$. An output drain current signal could be registered if the ISFET is biased with a constant voltage bias.

Following the same principle, FET biosensors are constructed. Capturing probes that are capable of specifically recognizing and binding to the target analyte, for example, antibody, are chemically coupled to the sensing gate forming an ImmunoFET [9], as illustrated in Fig. 1.1(c). They capture the target analyte with high specificity and selectivity through immunoreactions and keep them close to the sensing surface. As most biomolecules are intrinsically charged in the electrolyte, they induce opposite charges appearing in both electrolyte solution and semiconductor, disrupt the electrostatics close to the sensing surface and change the interface potential ψ_0 as illustrated in Fig. 1.2. The charge density in the semiconductor region change is then conveyed in the drain current or channel conductivity change of the FET. It is worth noting that such capacitive coupling through electric field has unique advantages from a sensor platform development perspective. It provides high isolation between the FET and the electrochemical system above as no faradic current passing through the dielectric is required for signal generation, which reduces the risk of potential degradation of the capturing receptors due to electrochemical reactions. In the DC biasing condition, the non-faradic current is also eliminated at the interface, minimizing any disturbance to the immunoreactions in the electrolyte.

FET-based biosensors hold an advantageous proposition to become a portable, affordable and easy-to-use analytical assay with high accuracy because of its following features. First, the sensor signal arises from the intrinsic charge carried by the target analyte but not labels, avoiding skill-demanding and time-consuming labeling processes, which shortens the sample processing time for detection on the field and avoids labeling reagent storage in the POCT device. Second, the FET sensor generates the electric signal, avoiding complex, delicate and expensive optics required in optical assays like fluorescent immunoassays and surface plasma resonance. Electric output signal significantly simplifies the readout circuit design and reduces the cost of the complete system. Third, it has excellent potential in miniaturization. The active sensing area could be, in theory, as small as the gate area of the FET as the sensing signal comes from local electrostatic potential change that is directly amplified by the underlying transistor. In contrast, amperometric electrochemical sensors relying on electron transfer in reactions may need a large electrode surface to generate sufficient signal magnitude. Reduced sensing area demands less reagent for surface treatment and receptor probe immobilization, which lowers the overall cost. FET sensors detecting a few molecules have been demonstrated [10]. However, it is worth noting that the entire sensor chip area of today's FET-based biosensors is often limited by its extended electric contacts and microfluidic packages.

1.2 Development of Field-effect Transistor Biosensors

The endeavor of employing a FET to sense biological relevant species starts from the invention of the ISFET. In the 1970s, Dr. Bergveld worked on a measurement system to sense the local sodium activity change for electrophysiology. They first connected a well-established ion-selective glass electrode (ISE) to a state-of-art solid-state amplifier with cables but soon identified two drawbacks: the system was prone to pick up environmental noise with long connecting wires, and the glass electrode was cumbersome. In addressing these two issues,

Dr. Bergveld moved the amplifying transistor directly underneath the sensing dielectric and devised the ISFET [11]. The transistor locally converted the potentiometric signal to an amperometric current, which is more robust to the electromagnetic interference in long wiring connections. More importantly, replacing the glass electrode with a MOSFET significantly reduced the probe size. Fig. 1.3 shows the original design of the ISFET. The device was demonstrated to be sensitive to the sodium and hydrogen activities and then used in recording the spontaneous activity of a guinea pig muscle.

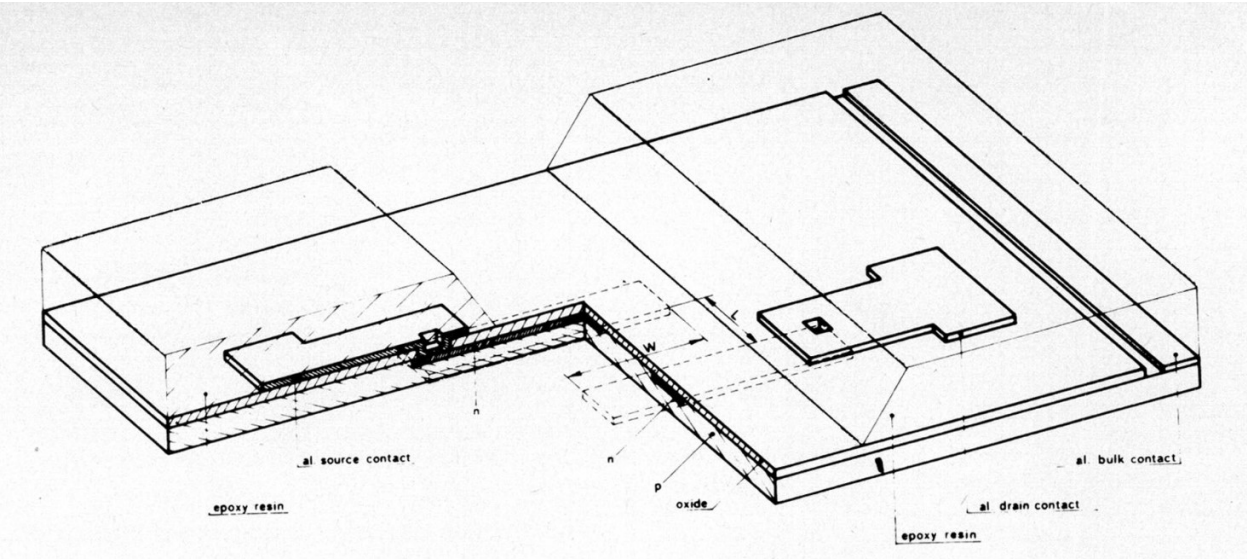

Figure 1.3: Schematic representation of the original ISFET [11].

The new sensor was, however, initially not well perceived due to its lack of stability, which has become a challenge accompanying these devices since then. It was not surprising that engineers thought that immersing a transistor in an aqueous physiological buffer solution was not a good idea. They had spent tremendous effort to isolate semiconductor chips from moister and sodium to improve the device reliability by following stringent clean room fabrication requirements and using encapsulating packages. The device drifting rendered the new sensors less welcomed than the glass electrodes, and ISFETs have never replaced the bulky pH electrode. Still, they have become a valuable tool for applications where miniaturization is more important than the measurement quality and long-term stability.

Table 1.1: Ionic strength and Debye length of different concentrated phosphate buffer solutions.

	Ionic strength (mM)	Debye length (nm)
1x PBS	162.7	0.76
0.1x PBS	16.27	2.41
0.01x PBS	1.627	7.61

Shortly after the invention of ISFETs, researchers started to consider detecting charged proteins and devised the ImmunoFET. Schenck first proposed to anchor immunoreactive probes onto the surface of the FET dielectrics and sense captured charged analyte with the underlying transistor [12]. Gotoh demonstrated the detection of human serum albumin in early 1990 [13]. Early experiments were, however, ambiguous to claim success as the detected signal was small compared with the device signal drifting and instrument resolution.

Direct sensing proteins were not considered promising for two reasons. First, counter ions accumulate around the charged biomolecules in the electrolyte and screen out their signal. The characteristic length of such screening is the Debye length which is defined as the distance where the charge-induced electrostatic potential change is reduced by 1/e. In electrolytes, the Debye length could be estimated by

$$\lambda_d = \sqrt{\frac{\epsilon_w k_B T}{q^2} \frac{1}{\sum_j^N n_j z_j^2}}, \tag{1.4}$$

where ϵ_w is the permittivity of water, k_B is Boltzmann's constant, T is the absolute temperature, n_j is ion concentrations in bulk solution, and z_j is the and charge number for each type of ions. Table. 1.1 lists the ionic strength and corresponding Debye length of the phosphate buffer solution (PBS) with different dilution factors at room temperature. In a physiological buffer, which has the same ionic strength as 1xPBS, the Debye length is much smaller than a typical protein molecule (10 nm), which makes direct sensing of its intrinsic charge a challenging task. Second, the dielectric surface groups that are responsible for pH

sensitivity form another buffering mechanism. Countering charge is induced at the insulator-electrolyte interface instead of inside the semiconductor, which further reduces the expected signal magnitudes. [14]. To overcome the second challenge, it has been attempted to develop an insensitive FET sensor as a REFET by passivating the dielectric surface with different inert layers. However, they lead to thicker dielectric that reduced the coupling between FET and charged biomolecules and, therefore, its sensitivity.

The breakthrough came in 2001 when Cui *et al.* showed that FET biosensors in form of the nanowire FET (nwFET) were able to detect prostate-specific antigen, a clinically relevant biomarker to prostate cancer, down to femtomolar concentrations, which is lower than convention assays can achieve [15]. In addressing the Debye screening, a diluted buffer with low conductivity and longer Debye length was used. Target molecules of different concentrations were spiked into the micro well containing the nwFET and, a clear nwFET conductivity change was registered. The success was attributed to the high surface-to-volume ratio of nwFET, which is believed to have stronger interaction between the bulk of nanowire and the bound charged biomolecules [15,16]. When nwFETs have a similar conducting carrier density as the charge carried by the target biomolecules, the binding events could induce a significant fractional change in nwFET current ($\Delta I_D/I_D$). Based on the same criteria, Gao *et al.* determined the optimal biasing for the maximum sensitivity at its subthreshold regime [16].

A larger relative current change could not explain why nanowires could achieve better sensitivity than planar devices. FET biosensors detected the surface potential change, and planar FETs could have generated even larger current signal change with the same electrostatic potential change induced by the captured molecules. Shoorideh and Chui later clarified the issue by analyzing the counter ion screening around the structures of different geometries [17]. They showed that nwFETs have an improved surface potential sensitivity because of the concave structure formed between the nwFET and the underlying substrate. As shown in Fig. 1.4 B and E, charged biomolecules located at corners induce large local

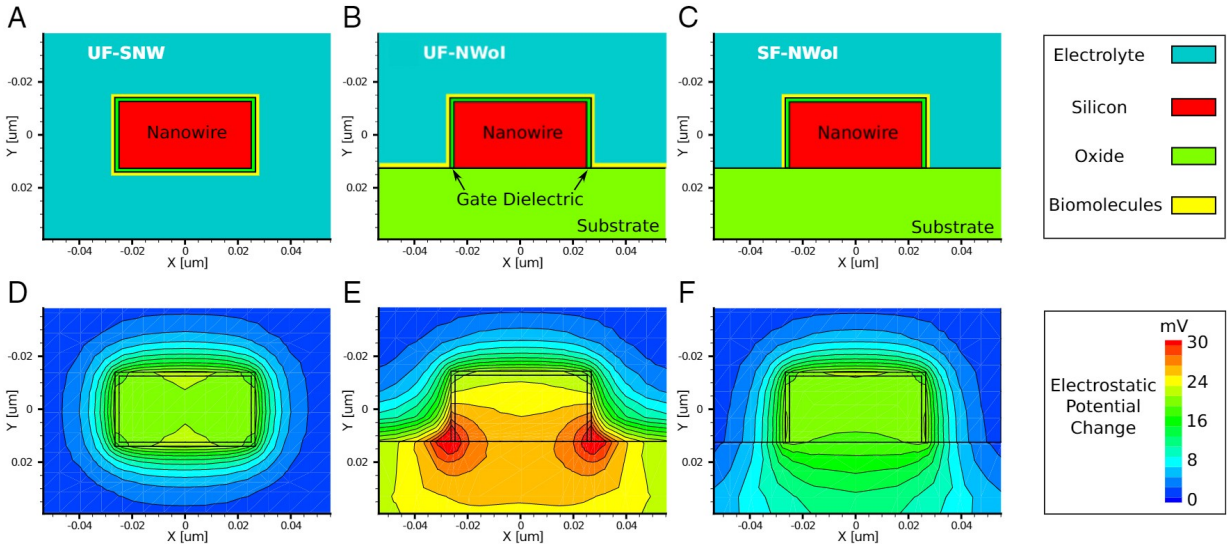

Figure 1.4: Simulation results showing reduced Debye screening due to the concave geometry at corners of nanowire FET sensor: Two-dimensional cross-sectional plots of the simulation structures (A–C) and the simulation results of the change in electrostatic potential due to the charge of the biomolecules, taken across the center of the channel (D–F) [17].

electrostatic potential change as the corner prevents as much screening counter ions to accumulate as in free space, which leads to a weaker screening. When molecules are located only on nanowire but not on the substrate (Fig. 1.4C and D), the geometry-dependent screening effect has less impact and will not enhance the electrostatic potential changes.

NwFETs unambiguously reignited the field and started a decade-long development of FET-based biosensors. They have thereafter been demonstrated outstanding sensitivity to quantify numerous clinically relevant biomarkers, including nucleic acids [18, 19], viruses [20, 21], and proteins [22–24]. FETs of other forms have also been proposed and used as biosensors, including nanoribbon [22, 25, 26], extended-gate FET [27, 28], dual-gated FET [29, 30], graphene [31–33], tunneling FET [34, 35], and negative capacitance FET [36]. To the author's view, the successful resurgence of FET-based biosensors should also be attributed to the improvement of semiconductor device characterization techniques. Early

nwFET biosensors only had a diameter of a few nanometers. They carried an AC baseline electrical current in the magnitude of less than a hundred nanoamperes with expected output current change of less than one nano ampere [37]. Employment of the high sensitivity lock-in amplifier was critical to reduce the noise level and capture tiny signals, which was not widely available in early ImunnoFET development. FET biosensors were often developed and characterized with matured modern semiconductor characterization system, which could measure the device current with a large dynamic range and high precision. The readiness of these measuring techniques laid an essential foundation for innovations in FET-based biosensor development.

1.3 Significance of the Measurement Uncertainties in FET-based Biosensors

We are to review some common figures of merits for a generic analytical assay before discussing the significance of measurement uncertainties in FET biosensors. In characterizing an assay, one calibrates its response to the analyte of different concentrations establishing a functional relationship, i.e., a calibration curve. The sensitivity of the assay is defined as the slope of this calibration curve. The Lower Limit of detection (LLOD) represents the smallest concentration of the target analytes the assay could reliably detect, which is one of the most concerning figures of merits. The capability to detect a specific biomarker at extremely low concentration enables early diagnosis of disease in preventative health care and is crucial in public health screening. LLOD is defined as the smallest target analyte concentration, c_L, generating signal x_L equals to $x_L = \bar{x}_{bl} + ks_{bl}$, where $\bar{x_{bl}}$ is the mean of measured values of blank samples, s_{bl} is its standard deviation and k is a numerical factor chosen from the confidence level [38]. Assuming the assay has a sensitivity S, LLOD can be written as

$$c_L = \frac{ks_{bl}}{S}.$$

In essence, LLOD is the amount of target analyte capable of generating signal change that is larger than the background measurement uncertainties. An assay should have its sensitivity S maximized and measurement uncertainties s_{bl} minimized to achieve a confident detection at low target analyte concentration levels. Efforts have been made in both directions to lower the LLOD of FET-based biosensors.

The sensitivity is intrinsically limited by the double layer screening from ions in the electrolyte and surface groups [39, 40]. In overcoming the Debye screening, FET sensors have been typically measured in diluted buffers. Though this strategy prevented its use in *in vivo* applications, a dedicated low conductivity measuring buffer works in analytical assays. To further reduce the screening limit, Shoorideh proposed to create a neutral dielectric-electrolyte interface where the double layer capacitance is minimized [40]. Efforts have also been made to use FET biosensors in high conductivity buffers, like 1xPBS. One approach is to use shorter capturing probes [41] and another is to deplete countering ions close to the surface with polyethylene glycol layer [42]. Enhancing the surface charge from the specific target binding reaction were also attempted. Existing efforts include coupling enzymatic reactions [43], and using highly charged capturing probes like aptamer [44, 45]. For FET biosensors with their drain current as the output signal, their sensitivity could also be promoted by increasing a device with higher signal gain.

Reducing the measurement uncertainties is the other direction to improve the performance of FET biosensors. Measurement uncertainties of FET biosensors originate from multiple sources, including noise, instability, device-to-device variation, sample preparation, etc. Many experiments demonstrating exceptionally low limit of detection managed to circumvent all these uncertainty sources but noise with a genuinely designed experiment protocol [15, 20, 22, 46]. Specifically, the sensor was first measured for an extended period of time till the sensor was stabilized before any target analytes being introduced into the system, as illustrated in Fig. 1.5(a). The blank sample measurements, x_{bk}, in such experiment were data recorded within a short period of time before introducing the target analytes, and the signal

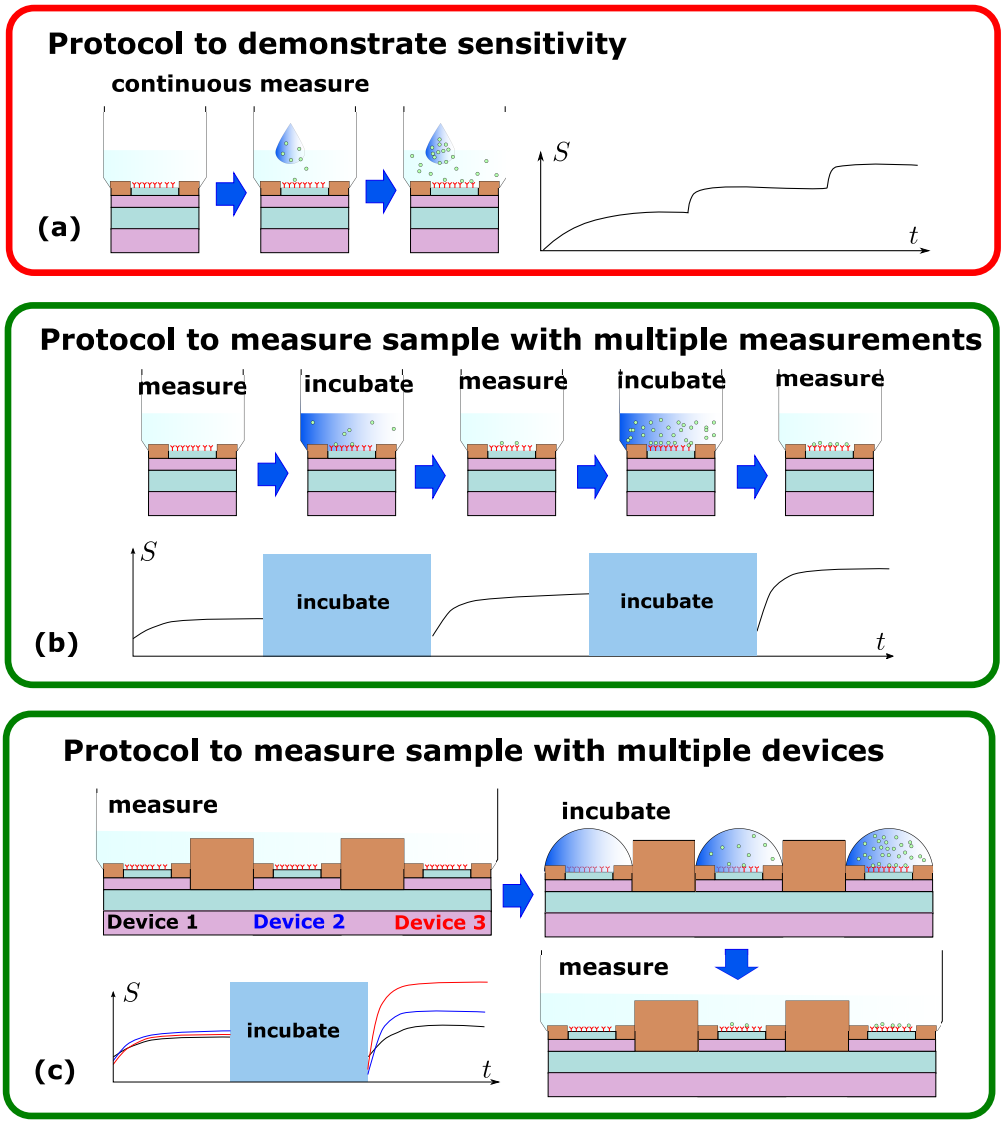

Figure 1.5: Comparison of protocols used in demonstrating high sensitivity of FET biochemical sensor and those required to measure clinical samples: (a) protocol used to demonstrate sensitivity in research laboratories; (b) protocol generating calibration data with multiple measurements using a single device; (c) protocol generating calibration data with multiple devices.

only needed to surpass the current fluctuations, i.e., noise, to declare a sensitive detection. Effects of the drifting is mitigated by the initial stabilization process, and the repeatability is neither of concern because the evaluation was completed within a single measurement. Noise has, therefore, long been regarded as the dominant measurement uncertainty source and extensively characterized. To some extent, noise performance sets a lower bound of the measurement uncertainties and is closely related to the ultimate low limit of detection of a FET biosensor [47–49].

Quantifying analyte concentrations in real samples is a more complicated task, and the above protocol can not be directly adopted for the following reasons. First, direct spiking patient samples during a continuous measurement is not realistic. Physiological buffer in a patient sample has a higher conductivity, and direct spiking them into the measurement buffer having lower conductivity changes its ion concentration and potentially induces a false signal. Using a high conductivity measurement buffer to match with patient samples seems a solution, but the increased screening may diminish the FET sensitivity [22, 50]. In addition, variation of the buffer properties like pH values among different patients will also introduce additional measurement uncertainties. FET biochemical sensors often have similar or even greater sensitivity to the buffer's pH and conductivity compared with its surface charge density [51]. Second, a calibration response needs to be established to infer the analyte quantity back from the sensor response, which is challenging to fit into a single continuous measurement.

In addressing the first issue, an incubation process was added, during which the sensor is exposed to the samples allowing its surface capturing probes to react with the target analytes [52]. After each incubation, the low conductivity measurement buffer is re-introduced into the system to provide a stable chemical environment for the measurement. The sensor response can no longer be defined as the signal change compared with the measured data points right before the analyte introduction as the measurement process was discontinued in incubation. The calibration data could be generated with two approaches, as illustrated

in Fig. 1.5(b) and Fig. 1.5(c). The first approach measures a single device multiple times to generate its calibration curve. The device response is characterized after incubating standard solutions with known target concentrations. The concentration of the standard solutions is intentionally chosen to be either much lower or higher than the interested target concentration range in patient samples. Those standards with low concentrations are measured before measuring the patient sample, and those with higher concentrations are measured afterward. The calibration curve is then established along with the patient sample measurement on the same device [24]. In the second approach, different devices are used to generate the calibration curve and measure sample simultaneously, which is similar to the protocol used in ELISA [53]. Each approach faces additional challenges in controlling measurement uncertainties. In the multiple measurements approach, the repeatability and stability, whether measurements of the same device give the same signal level, become an important issue [54]. In the multiple device approach, device-to-device variation apparently should be critically evaluated.

Such difference from the author's perspective is one critical reason behind the fact that FET biochemical sensors have not been widely adopted and generate practical impacts despite their tremendous success in research demonstrations. To develop the FET biochemical sensors into practical assays without much degrading their sensing performance, we need to gain a better understanding on critical sources of the measurement uncertainties and devise strategies that are both effective to eliminate their effects and feasible to be incorporated into protocols designed to measure clinical samples. Efforts have been made to improve the device instability, including optimizing device fabrication process [53, 55, 56], improving the reference electrode drifting [57, 58], and adding a pre-stressing process during the measurement [59]. Recently, Kuo *et al.* reported that the device stability could be improved by using high viscosity solution, lowering the detection temperature and, optimizing surface probe density [54]. Unfortunately, the measurement uncertainty from device instability was observed to be still much larger than the noise level. On reducing device-to-device varia-

tions, FET sensor array have been reported using mature CMOS processes [53,60,61]. With extensive process optimizations, the device-to-device threshold voltage variations have been reduced to a few tenths of millivolts, which is still considerably large considering the maximum potential interface potential changes are reported to be of only a few hundreds of millivolts.

1.4 Overview of the Presented Work

This dissertation aims to enhance our understanding of measurement uncertainties in FET-based biosensors and propose strategies to mitigate them. In this work, we first analyzed the low-frequency noise of dual-gated silicon field-effect transistor (DG-FET) biosensors with Schottky contacts, which sets their intrinsic LLOD. We identified the optimal biasing solution for such devices and found the flicker noise arising from traps with a non-uniform energy distribution at the sensing insulator-semiconductor to be the major noise source while employing Schottky contacts to have minimal noise contribution with a sufficiently large back-gate bias voltage. We argued that the DG structure is advantageous over its single-gated (SG) counterpart when a non-uniform trap energy distribution is presented. We then moved on to study the instability of the same DG-FET biosensor, which led to larger measurement uncertainties in sensing experiments that requires multiple measurements. In contrast to well-passivated devices in integrated circuits, FET-based biosensors are exposed to buffer electrolyte and, therefore, more prone to instability issues, including device characteristic drifting and irreproducible results. We analyzed the instability observed in DG-FET and hypothesized it was a result of redistributed protons inside dielectrics the back-gate oxide. Two improved measurement schemes, pulsed IV and pulse resetting, were proposed and demonstrated to mitigate its effects in the measurement data. In the last part of this work, we investigated the nonlinearity in FET-based binding assay responses. We showed that the nonlinear transduction mechanism of FET sensors plays an important role in shaping their

dose-response curves when operating in the nonlinear regime. Negligence of such nonlinearity would introduce errors in the extracted affinity properties of the analyte-receptor pair.

CHAPTER 2

On Noise Performance of Dual-gated Silicon FET Biosensors with Schottky Contacts

2.1 Overview

A field-effect transistor (FET) biosensor has its gate electrode replaced with an electrolyte and insulator surface modified for binding with target biomolecules. They have exhibited outstanding sensitivity in quantitating various biomolecular analytes [15, 22] and become promising sensing devices for next-generation genome sequencing [62], biomarker detection [63], single-cell analysis [64], environmental monitoring [65], and protein kinetics measurement [66]. As its lower limit of detection (LLOD) is intrinsically governed by the signal-to-noise ratio (SNR), the low-frequency noise (LFN) is an essential factor to understand in further improving its analytical performance [67–69].

Among other structures, silicon FET formed on silicon-on-insulator (SOI) wafer allows additional biasing freedom with the substrate acting as a back-gate and constitutes an asymmetric dual-gated FET (DG-FET). They have exhibited the "Super Nernstian" sensitivity via a front-back gate coupling effect [70–72]. They were later found having the same intrinsic LLOD as the single-gated FET (SG-FET) counterparts, and the usefulness of a second gate has been questioned [73, 74]. In establishing those findings, however, previous studies [29, 73–76] did not consider possible energy distribution of the interface trap density and often assumed a uniform energy distribution through the bandgap. The actual interface trap state energy distribution is determined by the employed dielectric material and fabri-

cation process. Both uniform [77] and non-uniform [78–80] trap state energy distribution have been reported in SG-FET sensors. Potential benefits of having the second gate when a non-uniform trap energy distribution is present have not been studied yet.

When such FET sensors are made with Schottky contacts instead of conventionally doped junctions, the overall thermal budget and dopant engineering complexity can be substantially reduced. Ambipolar conduction of Schottky Barrier FET biosensor can be used to simultaneously enhance its sensitivity to target analytes of different charge polarities [81]. Their nonlinear rectifying current-voltage characteristics also create design opportunities for novel sensors with intrinsic signal amplification capability [24, 82]. While the associated noise penalty has been identified with the SG-FET structures [83], it remains unclear for the DG-FETs.

In this work, we critically examine the LFN characteristics of Schottky-contacted DG-FET biosensors. We experimentally identified the dominant noise source and extracted the input-referred voltage noise power spectral density (PSD) under various biasing regimes and ambient. We analyze the data against a model incorporating the number fluctuation theory [84] and front-to-back gate coupling [85], attributing the optimum to arise from a non-uniform distribution of trap density at the front sensing interface. Considering such inherent noise-contributing source, we further scrutinize whether the DG-FET structure possesses any practical advantage over its SG-FET counterpart.

2.2 Modeling Low-frequency Noise in DG-FET

Isolating the dominant noise source in a DG-FET sensor system is crucial toward understanding and optimizing its noise performance. We assumed various noise contributors connected together as one circuit in Fig. 2.1 to subsequently analyze their effects on the detection limit in this section. The DG-FET sensor is biased by both back-gate from the substrate and front-gate with a reference electrode in the electrolyte solution. Specific bio-molecular

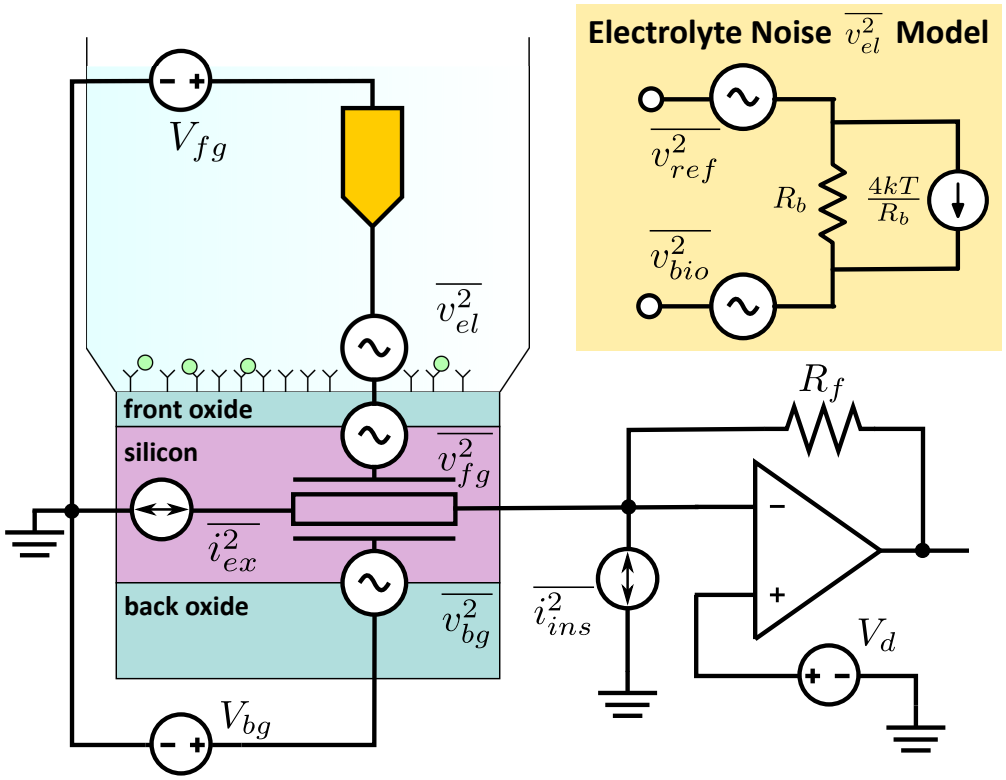

Figure 2.1: Schematic illustrating noise sources in a dual-gated FET biosensor including electrolyte associated noise $\overline{v_{el}^2}$, flicker noise $\overline{v_{fg}^2}$ and $\overline{v_{bg}^2}$, contact associated noise $\overline{i_{ex}^2}$, and instrument noise $\overline{i_{ins}^2}$. The inset shows the composition of electrolyte associated noise $\overline{v_{el}^2}$ in which R_b represents bulk electrolyte resistance.

probes are anchored at the electrolyte-dielectric sensing interface and induce electrostatic potential signal change on capturing charged target analytes.

We included various noise sources in Fig. 2.1 and assumed them uncorrelated with one another because of their different locations and physical origins. The DG-FET is biased by both the back gate from the substrate and front gate with a reference electrode in solution. Specific biochemical probes reside above the electrolyte/dielectric sensing interface, where binding reactions with charged analyte targets occur. We modeled the noise originated from the electrolyte with an equivalent voltage source $\overline{v_{el}^2}$ at the sensing interface. It is physically composed of three independent sources as illustrated in the inset: potential

fluctuation at the reference electrode-electrolyte interface $\overline{v_{ref}^2}$ [86], thermal noise of the bulk electrolyte $4kT/R_b$ where R_b is the electrolyte resistance, and noise induced by the surface bio-molecular probes $\overline{v_{bio}^2}$. Hassibi *et al.* have derived analytical expressions for $\overline{v_{ref}^2}$ and $\overline{v_{bio}^2}$ for different interface polarization and dominant ion transportation mechanism [87], and Deen *et al.* further discussed their implementation in SG-FET biosensors [47]. The origin of $\overline{v_{bio}^2}$ was initially attributed to the random adsorption and desorption at the sensing surface [88, 89] and later explained as a result of charge entering and exiting electrical double layer (EDL) causing local electrostatic potential fluctuation [90]. Both its magnitude and related Lorentzian time constant were found sensitive to the target analyte and proposed as alternative detection methodologies [89, 91]. In contrast to low frequency noise from FETs, which is independent of solution pH [77, 92] and ion concentrations [67, 93], $\overline{v_{bio}^2}$ was found sensitive to the analyte concentrations in solution and thus employed in frequency domain detection methodologies . From their analysis, the equivalent voltage noise source $\overline{v_{el}^2}$ is expected to possess a Lorentzian shaped power spectrum whose magnitude and time constant are sensitive to the bound molecules [47, 87, 89, 90].

Flicker noise at the dielectric-semiconductor interfaces are modeled with the carrier number fluctuation theory [76, 77] as

$$\overline{v_{fg,bg}^2} = \frac{q^2 \lambda k T N_t^{fg,bg}(E_f)}{W L C_{fg,bg}^2 f}, \tag{2.1}$$

where q is the electron charge, λ is the tunneling distance, k is the Boltzmann constant, T is the temperature, E_f is the Fermi level of the surface, $N_t(E_f)$ is the volume trap density at the energy level of E_f, W and L are width and length of the channel, $C_{fg,bg}$ is the unit area capacitance of gate dielectric, and f is the frequency. We explicitly wrote the equivalent trap density $N_t(E_f)$ as a function of the Fermi level E_f as only traps with energy close to E_f contribute to the carrier fluctuation, which has been often overlooked in previous noise analysis where a uniform trap energy distribution was assumed [29, 73–76]. The uniform assumption is more reasonable when the device is operated above the threshold voltage, where the surface potential is atcually pinned as in many analog circuits where FETs operate

[94]. However, this may not be the case in FET sensors and cautions must be applied in treating the trap energy distribution. Because of the front-back coupling, the two noise sources affect DG-FET current regardless of the carrier's physical location. Such coupling would only be screened when one surface is filled with the opposite carriers, where $\overline{v_{fg}^2}$ will be shorted to the signal ground [85]. We represented the noise possibly arising from the device access regions and contacts [76, 83] with a current noise source $\overline{i_{ex}^2}$. Lastly, an equivalent current source $\overline{i_{ins}^2}$ captures the noise from measurement instruments [95].

We summarized the contribution of each hypothesized noise source to the equivalent input-referred voltage noise PSD as

$$\frac{\overline{i_d^2}}{g_{m,fg}^2} = \overline{v_{el}^2} + \overline{v_{fg}^2} + \overline{v_{bg}^2}\frac{g_{m,bg}^2}{g_{m,fg}^2} + \frac{\overline{i_{ex}^2} + \overline{i_{ins}^2}}{g_{m,fg}^2}, \tag{2.2}$$

where $g_{m,fg}$ and $g_{m,bg}$ are front- and back-gate transconductance. The input-referred voltage noise magnitude indicates the minimum potential signal an FET sensor could resolve at its sensing interface and therefore equivalently determines the noise limit of the LLOD [67–69, 73]. Eq. 2.2 suggests that the measured input-referred voltage noise has different dependency on $g_{m,fg}$ when different noise source dominates. It is a convenient analyzing metric to identify and understand the DG-FET sensors' noise behavior since both quantities could be directly extracted from the measurement results.

2.3 Devices and Measurements

2.3.1 Device Fabrication and Surface Modification

We fabricated the Schottky-contacted DG-FET sensors in Integrated Semiconductor Nanofabrication Cleanroom (ISNC) and Nanoelectronic Research Facilities (NRF) at UCLA following the process flow previously developed in our lab [24], which is illustrated in Fig. 2.2. The process started with p-type $\langle 1\,0\,0 \rangle$ SOI wafers with 70 nm thick silicon layer and 145 nm buried oxide (SOITEC, France) [Fig. 2.2(a)]. We defined 150 nm wide silicon channel us-

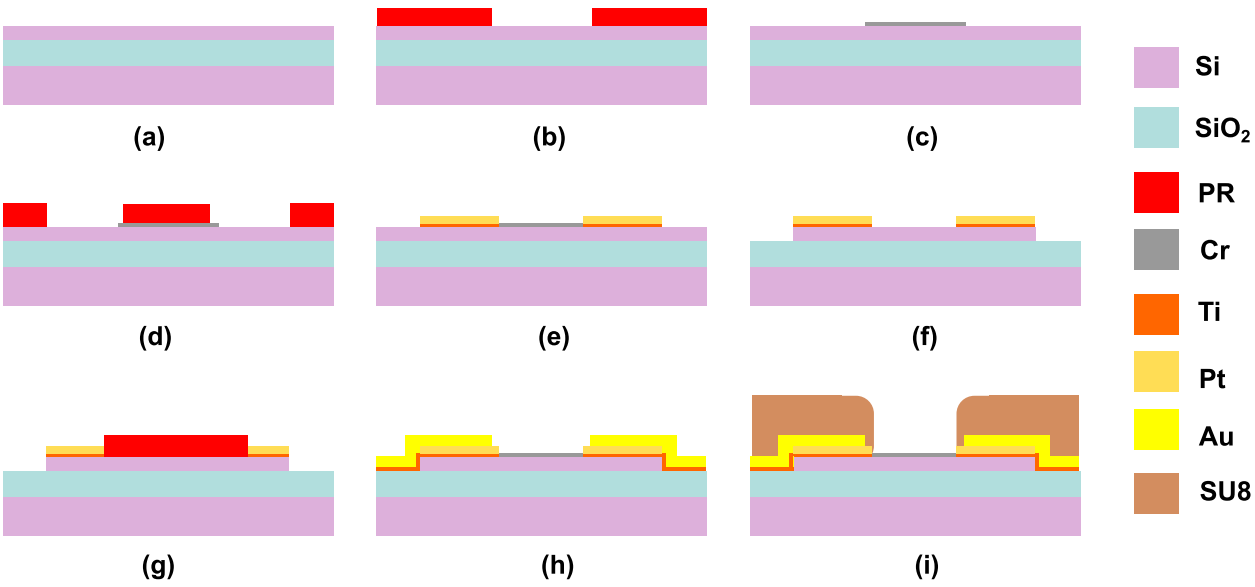

Figure 2.2: Fabrication process flow of the studied DG-FET with Schottky contacts.

ing e-beam lithography [Fig. 2.2(b)] and formed a hard mask by evaporating a chromium layer [Fig. 2.2(c)]. Source-drain contact pads were defined with the conventional lithography [Fig. 2.2(d)]. We then formed Pt-Si Schottky contacts above the contact pads by evaporating a Titanium/Platinum stack [Fig. 2.2(e)]. The active area containing silicon channel and contacts was etched out using hard masks defined in previous steps with the SF_6 reactive ion etching [Fig. 2.2(f)]. A lithography and lift-off were conducted to form Au leads which extended out for electrical probing [Fig. 2.2(g) and Fig 2.2(h)]. We conducted rapid thermal annealing at 450°C for 60 seconds to sintering the metal-silicon contacts. We then formed the isolation between metal leads and electrolyte with 1.5 μm SU-8 polymer and lithographically opened up the FET sensing region [Fig 2.2(i)].

A schematic of the fabricated device and its dimensions are shown in Fig. 2.3. The silicon channel is gated by both the front-gate from a reference electrode in the electrolyte and the back-gate through the silicon substrate. As no dopant was introduced in our fabrication process, we estimated the channel doping concentration to be 1.7×10^{15} cm^{-3} from the sheet resistance of the purchased SOI wafer. Vertical Pt-Si Schottky junctions with the area ($A_{S/D}$)

of $1.6{\times}10^4\,\mu m^2$ were formed on top of the silicon layer for the source and drain terminals. The front-gate length (L_{fg}) was defined by the SU-8 opening to be 15 μm. A 3 μm lateral spacing (L_{sp}) between the opening and contact pads was designed to prevent the front-gate from shorting to the source drain metal contacts.

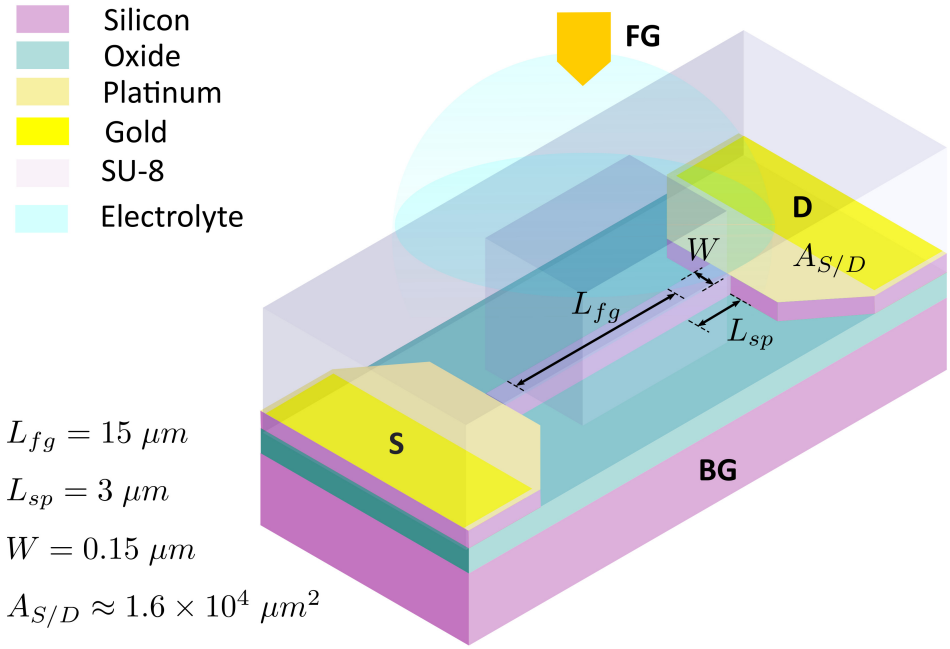

Figure 2.3: Schematic representation of the dual-gated silicon FET with Schottky contacts. The front-gate (FG) is biased from the electrolyte and the silicon substrate acts as the back-gate (BG). Schottky source (S) and drain (D) contacts are formed vertically between platinum and the active silicon layer.

3-Aminopropyltriethoxysilane (APTES) was conjugated to the native oxide surface on silicon channel to prepare a similar surface condition as in our previous sensing experiments [24,82]. Such silanization has been widely used for immobilizing biomolecule probe on sensing surface and helps to improve the device stability in aqueous condition [68]. We prepared 1% (v/v) APTES solution by diluting freshly purchased APTES (Sigma-Aldrich, United States) in pure ethanol (Sigma-Aldrich, United States). Fabricated chips were rinsed with deionized

(DI) water and ethanol, and then immersed in the APTES solution for 1 hour at room temperature. On completion, they were rinsed again with ethanol to remove unattached APTES molecules and blown dry with nitrogen.

2.3.2 Measurement Setup

Surface-modified chip was wire bonded to a ceramic dual-in-line carrier (Spectrum, United States) and loaded into an in-house built Faraday cage with zero insertion force (ZIF) connector (3M, United States). We measured device DC characteristics with Keithley 4200 semiconductor characterization system. For noise measurement, the drain current was amplified by a low noise preamplifier (SRS570) and fed to a dynamic signal analyzer (Agilent 35670A). In minimizing the noise from the biasing network, we employed batteries and potentiometers to bias the front- and back-gate terminals, and sourced the drain terminal voltage directly from the preamplifier. We measured the drain current noise power spectrum density (PSD) from 1 Hz to 800 Hz with a frequency resolution of 1 Hz.

2.4 Results and discussion

2.4.1 DC Characteristics of Schottky Contacted DG-FETs

First, we experimentally measured the DC characteristics of our Schottky-contacted DG-FET device. We observed decent back-gate transfer characteristics in air [Fig. 2.4(a)] showing that the device can be fully turned on with the back-gate biasing only. The measured transfer characteristic showed a relatively large subthreshold swing of 870 mV/dec. We extracted the back-gate threshold voltage of the characterized device to be 8.7 V using linear extrapolation method while it varies from 7 to 10 V among fabricated devices. Both relatively large subthreshold swing and threshold variation and can be attributed to the thick buried oxide associated with the back-gate.

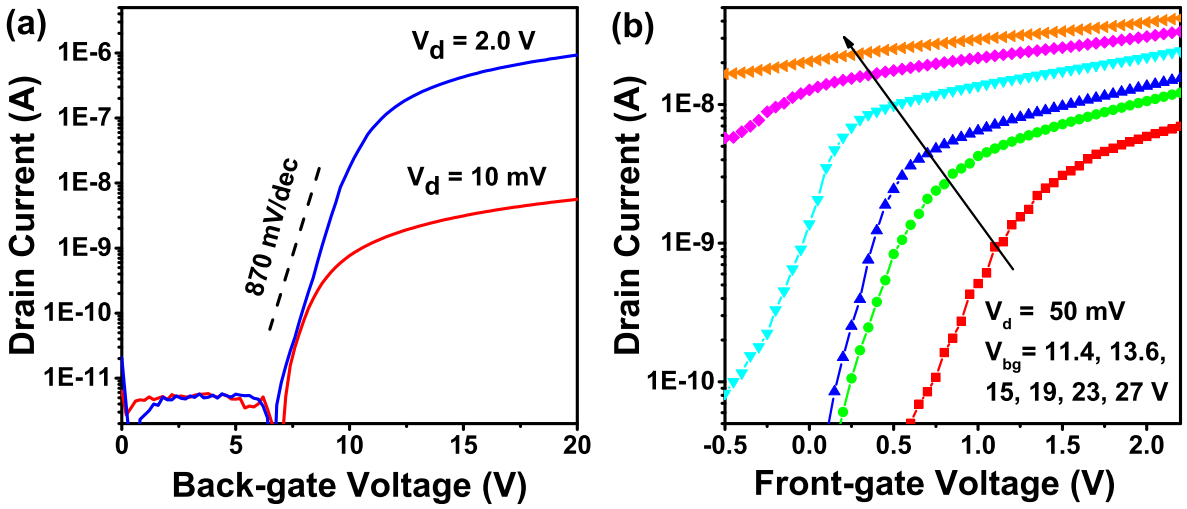

Figure 2.4: (a) Back-gate transfer characteristics of Schottky contacted DG-FETs measured in air. (b) Front-gate transfer characteristics in the dual-gated mode measured with different V_{bg} a fixed $V_d = 50$ mV.

We then examined the front-gate transfer characteristics under dual-gated operation in the electrolyte [Fig. 2.4(b)]. The front-gate threshold voltage shifts with different back-gate voltages because of the front-back gate coupling effect. An increasing back-gate voltage lowers the front-gate threshold voltage and leads to a larger drain current at the same V_{fg}. We also observed a lower front-gate subthreshold swing at higher V_{bg}, which is ascribed to the reduced contact resistance. With a positive back-gate bias voltage, electron carriers accumulate at the back-gate dielectric-silicon interface underneath the Schottky contact pads and access region covered by the SU8 passivation. Increased V_{bg} leads to higher electrostatic doping (n-type) in the silicon layer which helps reduce the contact resistance.

2.4.2 Low-frequency Noise under Back-gated Operation

We characterized the noise behavior of our Schottky contacted DG-FETs in air under back-gated operation to assess the noise contribution from Schottky contacts. From the current

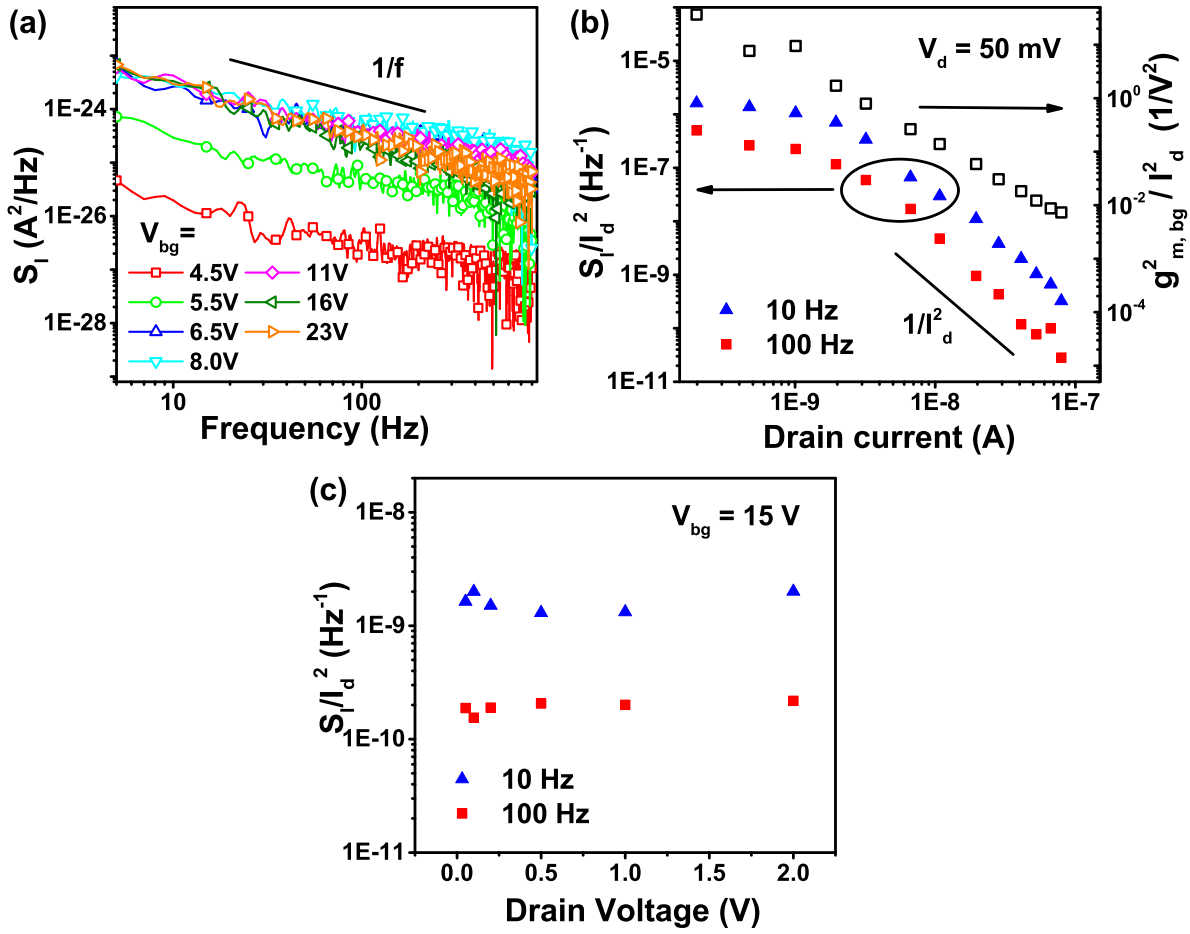

Figure 2.5: Low-frequency noise measurement in back-gated mode showing Schottky contact contribution to overall FET noise to be minimal: (a) drain current noise power spectral density with different V_{bg}. (b) Normalized current noise power spectral density at 10 Hz and 100 Hz and $g_{m,bg}^2/I_d^2$ plotted versus drain current with fixed $V_d = 50$ mV and increasing V_{bg}. (c) Normalized current noise power spectral density at 10 Hz and 100 Hz versus drain voltage with fixed $V_{bg} = 15$ V.

noise PSD at $V_d = 50$ mV and different V_{bg} [Fig. 2.5(a)], we observed a clear 1/f spectrum showing the flicker noise dominance. We plotted the normalized PSD versus drain current (with increasing V_{bg}) at a constant V_d of 50 mV and $g_{m,bg}^2/I_d^2$ in Fig. 2.5(b) . S_I/I_d^2 stayed flat in subthreshold and rolled off as $1/I_d^2$ above threshold. Such behavior along with its

relative parallelism with $g_{m,bg}^2/I_d^2$ agrees well with the number fluctuation theory for long-channel FETs [96]. Excess current noise related to Schottky junctions has been reported to be evident from an exponential increase of normalized current power spectral density towards small drain bias [83, 97]. We plotted the normalized PSD against varying V_d at a fixed V_{bg} = 15 V in Fig. 2.5(c) and observed a rather flat profile which suggests minimal $\overline{i_{ex}^2}$ from Schottky contacts in our devices. The foregoing results indicate that our devices under the back-gated mode operation behave like doped source-drain FETs from the noise performance perspective.

2.4.3 Low-frequency Noise under Dual-gated Operation

We examined our Schottky contacted DG-FET sensors under dual-gated operation in electrolyte. First we measured S_I at a fixed V_{bg} and different V_{fg}, and observed again 1/f spectra [Fig. 2.6(a)]. The absence of a Lorentzian spectrum suggests negligible $\overline{v_{el}^2}$ contribution. To identify the optimal bias, we measured the front-gate transconductance ($g_{m,fg}$) versus respective drain current at few specific V_{bg} [Fig. 2.6(b)]. Then we computed the input-referred voltage noise ($S_I/g_{m,fg}^2$) also versus respective drain current as shown in Fig. 2.6(c), with each curve tracking one particular V_{bg} under varying V_{fg} from 0 to 2 V. The optimal bias condition for the lower limit of detection corresponds to the lowest input-referred voltage noise.

Generally speaking, the input-referred voltage noise is lower at higher V_{bg} (e.g. 11.4 to 19 V). Larger back-gate bias enhances the vertical electric field through the silicon body which facilitates electron tunneling across the Schottky junction and lowers $\overline{i_{ex}^2}$ [83, 97] as illustrated in Fig. 2.7(a). Besides, higher electrostatic doping from back-gating could also contribute to the noise performance improvement by reducing the contact resistance [29]. Under sufficiently high V_{bg} (e.g. $\geq$ 19 V), the input-referred voltage noise minimums of respective V_{bg} appear at the low drain current regime or under low V_{fg}. The minimum input-referred voltage noise being achieved with multiple V_{bg} in Fig. 2.6(c) suggested $\overline{i_{ex}^2}$

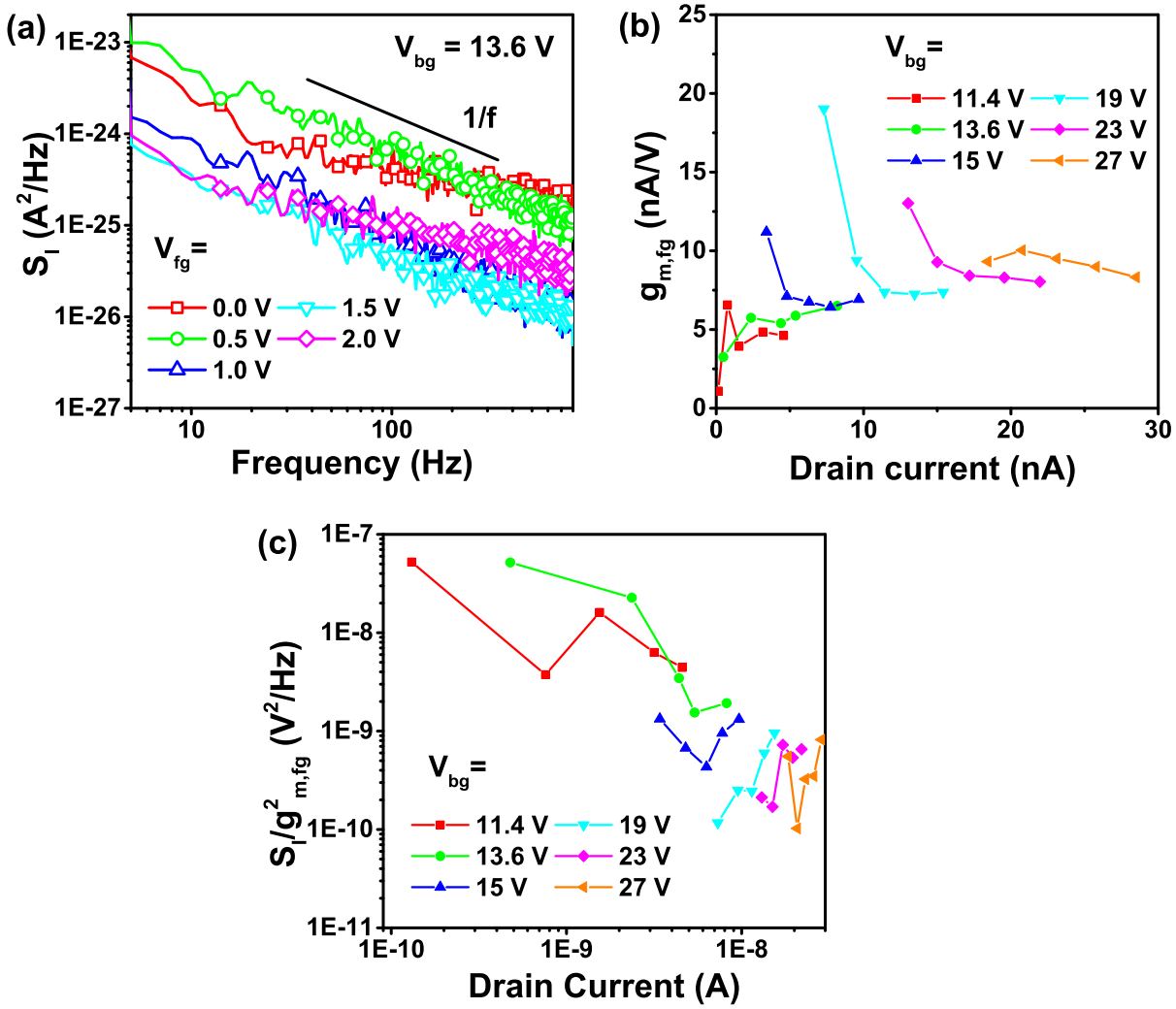

Figure 2.6: Low-frequency noise measurement in dual-gated mode: (a) Drain current noise power spectral density with V_{bg} = 13.6 V. (b) Front-gate transconductance and (c) input-referred voltage noise power spectral density at 100 Hz plotted against current with the labeled V_{bg}. Drain voltage was fixed at 50 mV in all above measurement.

has been sufficiently suppressed at these back-gate bias voltages as in the back-gated mode operation.

To further understand the physical origin of the measured noise behavior, we plotted the

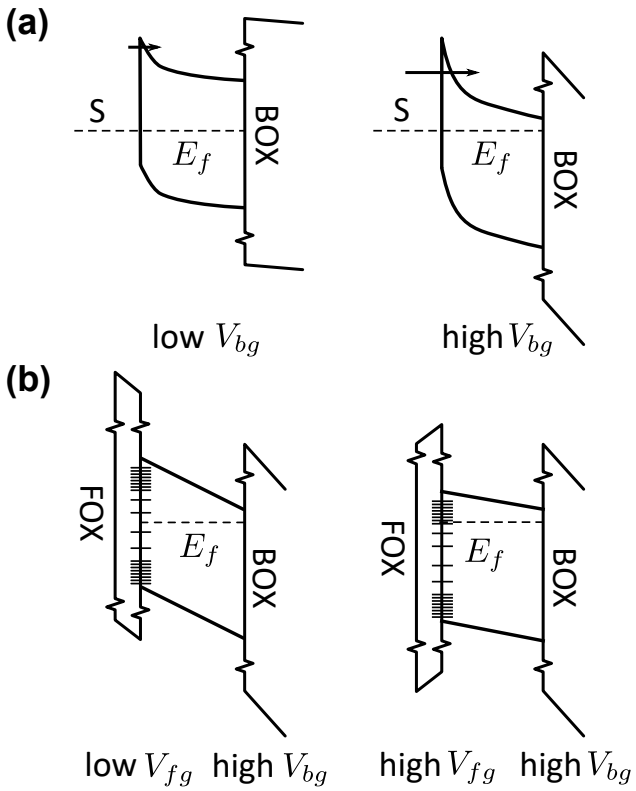

Figure 2.7: Ideal band diagrams in explaining the measured noise behavior: (a) ideal band diagram through Schottky contact pads with positive back-gate voltage. Higher back-gate bias voltage facilitates electron transfer across the reverse biased Schottky junction. Electron carriers accumulate at the back-gate buried oxide (BOX) interface forming n-type electrostatic doping. (b) Ideal band diagram in the active sensing channel region illustrating higher front-gate bias voltage moving Fermi level from midgap towards bandedge encountering more interface traps at the front-gate oxide (FOX) sensing interface.

input-referred voltage noise against the front-gate transconductance (Fig. 2.8) following our LFN analysis in the last section. Their relationship takes different shapes as a different noise source in Eq. (2.2) dominates. The input-referred voltage noise decreased with $g_{m,fg}$ and had its minimum at the maximum $g_{m,fg}$. The equivalent PSD showed a quadratic roll-off with $V_{bg} = 11.4$ V, which agrees with our hypothesis that $\overline{i_{ex}^2}/g_{m,fg}^2$ dominates at low V_{bg} under dual-gated operation. However, the rate of roll-off was much higher than $1/g_{m,fg}^2$ at

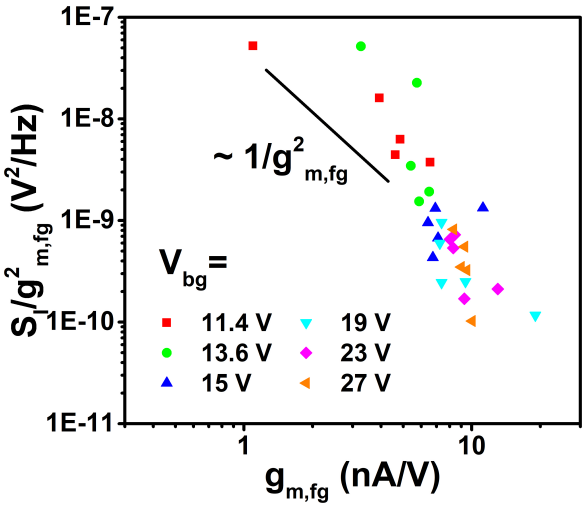

Figure 2.8: Measured input-referred voltage noise power spectral density versus front-gate transconductance with the labeled back-gate voltages.

higher V_{bg}.

The steep slope of the input-referred voltage noise ($\partial S_{v,fg}/\partial g_{m,fg}$) could be understood as a result of a non-uniform U-shape distribution of interface trap density, which is low near the middle of the bandgap and high towards the bandedges at the sensing front-gate interface. Such trap energy distribution profile has in fact been reported before on native oxide-silicon interface [78] and single-gated ion-sensitive FET (SG-ISFET) with a thermal grown oxide sensing surface [80]. Physically, increasing V_{fg} lifts the surface Fermi level from midgap toward the bandedge, encountering progressively more interface traps, which is illustrated in Fig. 2.7(b). The front-gate transconductance does not change much though [Fig. 2.6(b)] as carriers are mostly at the inverted back-gate channel interface under such high V_{bg}, leading to a steep slope in Fig. 2.8. The input-referred voltage noise minimum is therefore attained by biasing the back-gate channel interface in inversion to suppress $\overline{i_{ex}^2}$ and $\overline{v_{bg}^2}$ with considerable $g_{m,fg}/g_{m,bg}$, and the front sensing interface in depletion, where $\overline{v_{fg}^2}$ is low.

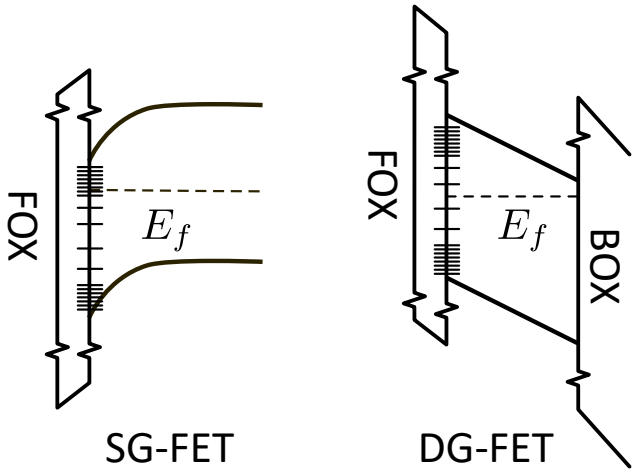

Figure 2.9: Ideal band diagrams illustrating the advantage of DG-FET over SG-FET when traps with a non-uniform energy distribution is present at the front-gate oxide sensing interface.

2.4.4 Practical Advantage of DG-FET over SG-FET for Noise Immunity

These mechanisms arguably suggest a practical advantage of DG-FET biosensors in noise immunity over SG-FETs when a non-uniform trap energy distribution $N_t(E_f)$ is present at the sensing interface. DG-FET is able to achieve both low noise PSD and high signal gain at the same time, though its minimum noise PSD remains the same. As illustrated in Fig. 2.9, SG-FET needs to be biased above threshold where noise performance is compromised to obtain considerable signal gain. In contrast, DG-FET could keep the front interface near the middle of the band gap where trap density is low and maintain a considerable signal gain with sufficient carriers at the back oxide-silicon interface. For FET sensors having a different sensing dielectric stack, the optimal biasing may not be the same as in the characterized devices because of the different trap density energy distribution. However, the hypothesized advantage of using the back-gate to bias the sensing interface at the energy level having lower trap density without compromising the signal gain would still hold true for the DG-FET.

2.5 Summary

We have studied the low-frequency noise of Schottky-contacted dual-gated FET biosensors. Our measurement revealed that noise associated with the Schottky contacts could be suppressed with a large back-gate bias while the flicker noise at the sensing insulator/semiconductor interface would dominate. The optimal bias for LLOD was attained with a low front-gate voltage together with a high back-gate bias to minimize the interface traps encountered by the front sensing interface given a non-uniform U-shape energy distribution. We further suggested that DG-FET possesses a practical advantage over SG-FET as the former can leverage the back channel to supply sufficient carrier to improve transconductance and thus overall signal gain without compromising noise performance.

CHAPTER 3

On Instabilities of Dual-gated Silicon FET Biochemical Sensors

3.1 Overview

Field-effect transistor (FET)-based biochemical sensors have shown promising performance in detecting various biological and chemical species [15,22,98]. Instability, the device characteristics changing over time, has been found accompanying FET-based biochemical sensors due to their exposure to salty electrolyte solutions. The instability leads to a drifting output sensor signal, for example, in its drain current, and poses a major challenge in developing these sensitive FET sensors into practical bio-analytical assays. Stabilizing the sensor requires extra time and prolongs the detection procedure. Besides, the time-varying sensor characteristics could lead to different signal levels in multiple measurement runs, i.e., a run-to-run variation, resulting in a repeatability issue. As multiple measurements of the same device are reasonably expected in developing practical diagnostic assays, for example, to establish the calibration curve, such run-to-run variation generates a measurement uncertainty degrading the sensors' LLOD, compromising their reproducibility, and even leading to false detection. Reducing the drifting is critical for long-term monitoring biological quantities, for example, the blood pH monitoring during surgeries requires the employed pH sensor to have a maximum drifting rate of 0.02 pH over 10 hours [99]. Repeatability issue, however, is more concerning for analytical assays. Understanding the origin of the instability behaviors and developing techniques to counteract their effects remain a crucial task.

The instability of FET biochemical sensors has been attributed to many sources including dielectric instability [100–103], reference electrode drifting [57,104,105], and electrostatic discharging [106, 107]. Dielectric instability arises from the charge movement in the dielectrics. Fernandes *et al.* suspected that the mobile alkali ions in the dielectric stack was the dominant instability mechanism in an ISFET system. They observed their devices having less hysteresis when used in potassium-based buffers than in sodium-based buffers, suggesting that the sodium ions have caused the device drifting and hysteresis [101]. Dielectric hydroxylation and proton movement were also identified as major factors affecting the device instability. Jamasb *et al.* postulated that a defective oxide layer having less dielectric constant forms when the sensor is immersed in the aqueous solution and reduces the gate capacitance of the studied ISFET, causing its drain current drift [100]. Kwon *et al.* further considered the electrostatics of the redistributed protons inside the defective layer and developed an equivalent circuit model to describe the observed signal drifting [59, 102, 103]. Reference electrode drifting has also been found a significant contributor especially when a miniaturized pseudo reference electrode was used [57, 104, 105]. As the instability could come from multiple sources, a careful evaluation was required to identify the dominant instability mechanism in a specific sensing system.

Many EFT-based biochemical sensor demonstrations circumvented the instability issues by waiting as the time-varying signal transients often pronounced at the beginning of a measurement and its changing rate reduced over time. Target molecules were introduced into sensing system after the sensor was sufficiently stabilized [41,108,109]. As long as the baseline drifting is significantly slower than the instantaneous change rate of the expected signal from the target analyte, one could recognize the signal and claim a successful detection [110]. The strategy worked well for applications requiring only a single continuous measurement such as the blood pH monitoring in surgery, despite the added time. In reducing the FET signal drifting, Welch *et al.* proposed to use a cycling electric field in the gate dielectric during the measurement [111]. Kwon *et al.* showed that a high-to-low two-step solution

gate biasing could suppress the ISFET drifting [59]. Differential readouts, which measured the output signal difference bewtween the sensitive sensor and an insensitive reference FET, have been proposed to compensate common-mode drifting experienced by two devices [30, 112–114]. Besides, adding the self-assembled monolayer at the dielectric electrolyte interface surface also helped reduce the signal drifting associated with the sodium infusion [68, 115]. Existing techniques mostly worked with the SG-FET sensors, while few results with DG-FET structures have been reported. Besides, neither did them address the repeatability issue.

In this chapter, we studied the instability of our dual-gated silicon FET biochemical sensors. We observed both drifting and repeatability issues when the device was measured with a normal time-domain measurement scheme. We analyzed the transients in their drain current, gate current, and the reference electrode stability to identify instability sources. We simulated the instability behavior induced by the proton redistribution with a macroscopic physical-based model using Finite-Difference Time-Domain (FDTD) methods and compared the simulated results with those observed in our experiments. Our results suggested that the drifting could arise from the charge redistribution inside the back oxide under different electric bias. Its failure to recover to the initial spatial distribution could cause the repeatability issue. We determined that an alternating biasing scheme is preferred compared with conventional DC biasings. We proposed two pulse biasing techniques, pulsed IV measurement and pulse resetting, to counteract the device instability and validated their effectiveness.

3.2 Experimental Methods

3.2.1 Sensor Chip Preparation

The device under investigation was the dual-gated FET with Schottky contacts. Its detailed structure and fabrication process are described in the last chapter. The fabricated chips were diced into silicon dies having a dimension of 0.7 mm $\times$ 0.5 mm. We performed the surface treatment following the optimized protocol in all reported devices [24]. Fabricated

chips were thoroughly rinsed with deionized (DI) water and ethanol and then immersed in freshly prepared 1% (v/v) APTES solution for 1 hour at the room temperature. Chips were rinsed again with ethanol to remove unattached APTES and then blown dry with nitrogen. APTES converts the hydroxyl-terminated surface group on oxide to amine group, which is often employed as the first step to conjugate receptor probes on the sensing surface. Besides, such silanization process has been reported to improve the dielectric stability in aqueous solutions [68] and suppress the hysteresis caused by the sodium infusion [101]. Prepared chips were packaged with an in-house designed microfluidic cartridge as described in the following section and stored at 4 °C in a fridge if not being measured.

3.2.2 Microfluidic Module Integration

Stability evaluation requires a robust microfluidic system to avoid extrinsic instability factors associated with the fluid delivery and electrical connections. Conventional polydimethylsiloxane (PDMS) based microfluidic modules were found inapplicable in our study as they often leaked out during the evaluation, which was due to the small chip area and its SU8 surface passivation. Fully cross-linked SU8 on the top of the chip surface did not provide high enough hydroxyl group density required to form strong chemical bonds with the PDMS. We, therefore, developed a xurographic microfluidic cartridge to provide stable buffer supplies over the sensing area and reliable electrical contacts.

The microfluidic cartridge design for the studied FET sensor is illustrated in Fig. 3.1(a), and an assembled cartridge is shown in Fig. 3.1(b). The xurographic module was composed of three layers of double-sided adhesive (DSA) films made with a desktop cutter. The top and bottom layers contained openings for inlets/outlets and device sensing areas, respectively, and the middle layer defined the fluid channel. The top and bottom layers were made of polyester release liner of DSA tapes, and the middle layer was made of the adhesive film, which set the channel height to be 50 μm. The entire xurographic microfluidic module had a size of 2 cm^2. Cautions were applied in designing these xurographic stacks. No

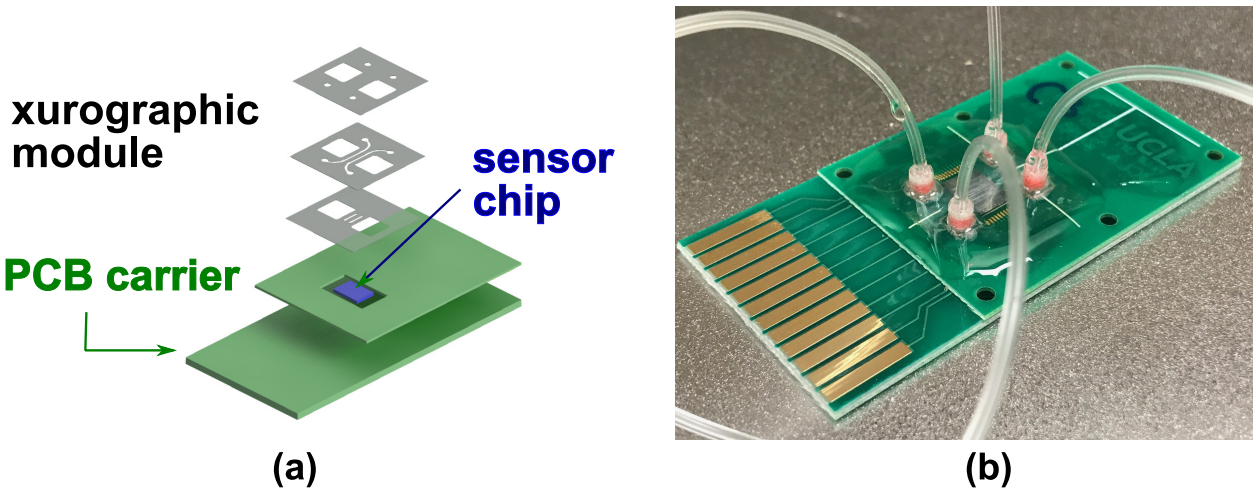

Figure 3.1: Design of the xurographic microfluidic cartridge for the studied DG-FET sensor. (a) The schematic representation of the microfluidic cartridge design and (b) the photograph of an assembled cartridge.

adhesive film was left at the top or the bottom of the fluid channel, which avoids the channel roof and floor collapsing and sticking together during the assembling process. Any residual adhesive could also be exfoliated by the passing fluid and clogs the channel during the sensing experiment. We designed two 0.5 mm wide channels with a separation of 1 mm to deliver buffers to different groups of devices. The chip was housed in a carrier composed of two layers of printed circuit boards (PCB) which provided additional sealing area and extended the electrical signals. The top panel was designed to have a similar height as the sensor chip to provide a leveled extension to land the xurographic module. The cartridge was designed to be inserted into the measurement using an edge connector.

We illustrate the cartridge assembly process in Fig. 3.2. Chip carriers were designed using EAGLE (Autodesk, United States). Two types of boards were used, as shown in Fig. 3.2(a). The bottom one served to extend the electrical connections and the top one to level up with the sensor chip and provide an extra footprint to attach the xurographic microfluidic module. Two boards were stacked together using superglue (LOCTITE 43903). We attached the sensor chip to the carrier with a silver epoxy (SPI supplies, United States) to

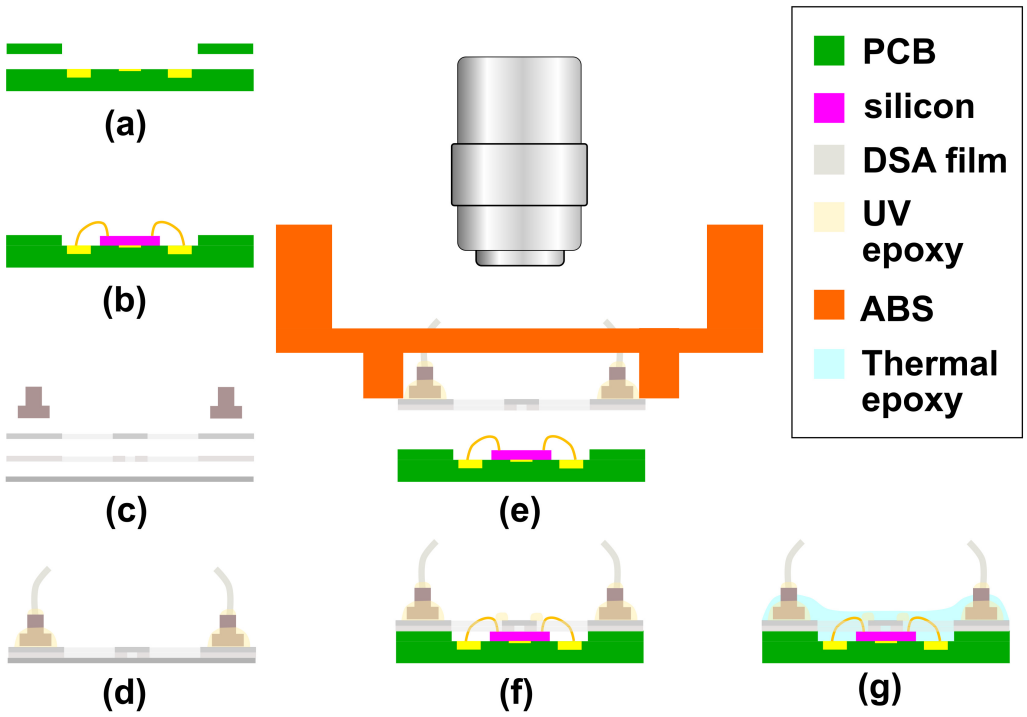

Figure 3.2: Process flow of integrating the xurographic microfluidic module with the sensor chip. (a) Top and bottom PCB boards were assembled together forming a chip carrier; (b) The prepared chip was attached and wire bonded to the carrier; (c) The xurographic model was separately cut and assembled. (d) Inlets and outlets were attached and tested;(e) Known-good xurographic model was assembled to the chip carrier with the assistant of a 3D printed fixture under the microscope; (f) The assembled cartridge went through a first UV epoxy sealing and a second (g) thermal epoxy potting process to improve their robustness.

make electrical contact with the chip substrate. Other contacts were wire bonded to the PCB chip carrier at the Center for High Frequency Electronics (CHFE) at UCLA [Fig. 3.2(b)].

Microfluidic modules were designed with AutoCAD (Autodesk, United States). Each layer was then made by cutting DSA films (3M Optically Clear Laminating Adhesive 8146-2) with a desktop cutter (Silhouette Inc., United States) and manually aligned and assembled as shown in Fig. 3.2(c). Customized inlets and outlets were 3D printed by an online service (Fictiv, United States) using photopolymer VeroClear (Stratasys, United States). They could also be replaced with PDMS stubs or Luer adapters if desired. Inlet/outlet was designed of the same size as holes on the DSA film to minimize the dead-volume. To install the inlets, printed connectors were first plugged with a short segment of PTFE tube, and then temporarily anchored to its designed position with the help of the adhesive layer on the top of the xurographic module. A Ultraviolet (UV) light cure epoxy (LOCTITE 325) was applied and cured to seal both the tube/connector and connector/film interfaces [Fig. 3.2(d)]. The constructed module was individually tested by passing dyed water through channels to check the sealing before assembling to the chip carrier. Failed modules were discarded.

We then manually aligned the microfluidic module to the sensor chip under a microscope with the help of a 3D printed fixture [Fig. 3.2(e)]. The xurographic module was temporarily attached to the fixture using the adhesive layer on the top, and the bottom layer was released to attach to the chip carrier. The fixture prevented the deformation of the flexible xurographic model during the manipulations and facilitated the alignment handling. After attaching the xurographic module to the chip carrier, the fixture was carefully removed. A two-step potting process was followed to encapsulate the fluid channel and electrical wires. The light cure epoxy was first applied to the edges of microfluidic modules and immediately cured [Fig. 3.2(f)] by applying UV light. We then encapsulated the sensor with a thermal epoxy compound (3M Scotch-Weld DP270 Clear), which had strong adhesion to the PCB board and formed a hard shell around the sensor chip [Fig. 3.2(g)]. The fully cured potting compound isolated the sensor chip from the outside environment, restricted the deformation

of the xurographic module, and prevented the degradation of electrical connections.

3.2.3 Electrical Measurement

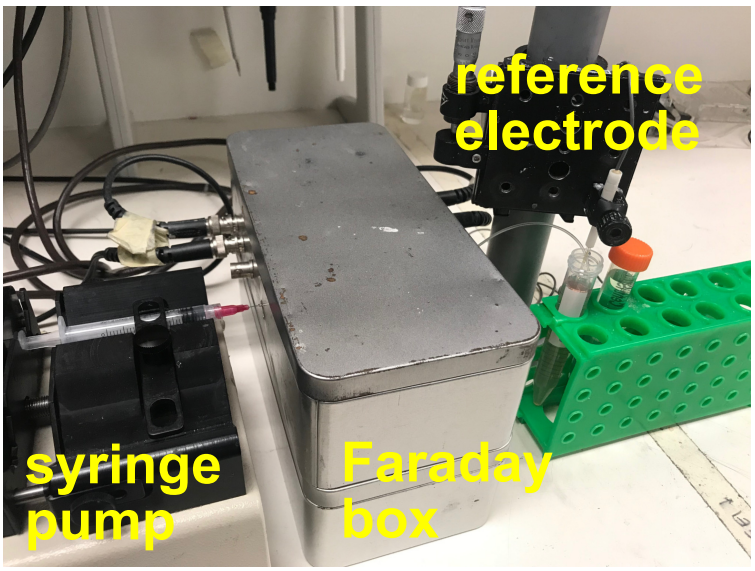

Figure 3.3: Photograph of the experiment setup in characterizing the sensor stability.

Packaged chip was loaded into a Faraday box and electrically connected to the semiconductor characterization system (Keithley 4200, Keithley Instruments, United States) with coaxial cables. Fig. 3.3 shows a photograph of the experimental setup. The FET front-gate was biased using a bulky Ag/AgCl electrode (Microelectrode Inc., United States) through the electrolyte reservoir. The buffer solution was transported to the sensing area using a syringe pump (KD Scientific, United States) in the withdrawing mode.

3.2.4 Pulsed IV Measurement System

In examining the pulsed IV measurement technique, a dedicated system was developed. Its schematic is shown in Fig. 3.4. The system was built around an FPGA-based USB multi-function device (Analog Discovery 2, Analog Devices, United States) which essentially served here as a handheld signal generator and high-speed oscilloscope. It was able to generate pulse

train signal having a pulse width as short as 20 μs and sample the FET response with a sampling rate up to 10 MHz. Low voltage (5 V) pulses were produced from the signal generator and fed to a MOSFET gate driver (ADuM4121, Analog Devices, United States) to generate high voltage pulses that were required to bias the back-gate of the DG-FET sensor. The developed system was able to provide a biasing voltage up to 30 V using a boost converter from a 9 V battery set. FET drain terminal bias was directly sourced from the output of an onboard digital to analog converter (DAC). We converted the drain current of the FET sensor to a voltage signal with a high bandwidth (1.6 GHz) transimpedance amplifier (OPA675, Texas Instruments, United States), and fed it to the oscilloscope input. Pulses at the gate terminal was sensed as the triggering signal. The entire measurement was coordinated using in-house developed control software on a PC through the USB port. The device under test was kept in the same Faraday box as in the normal measurement to provide a good electromagnetic shielding.

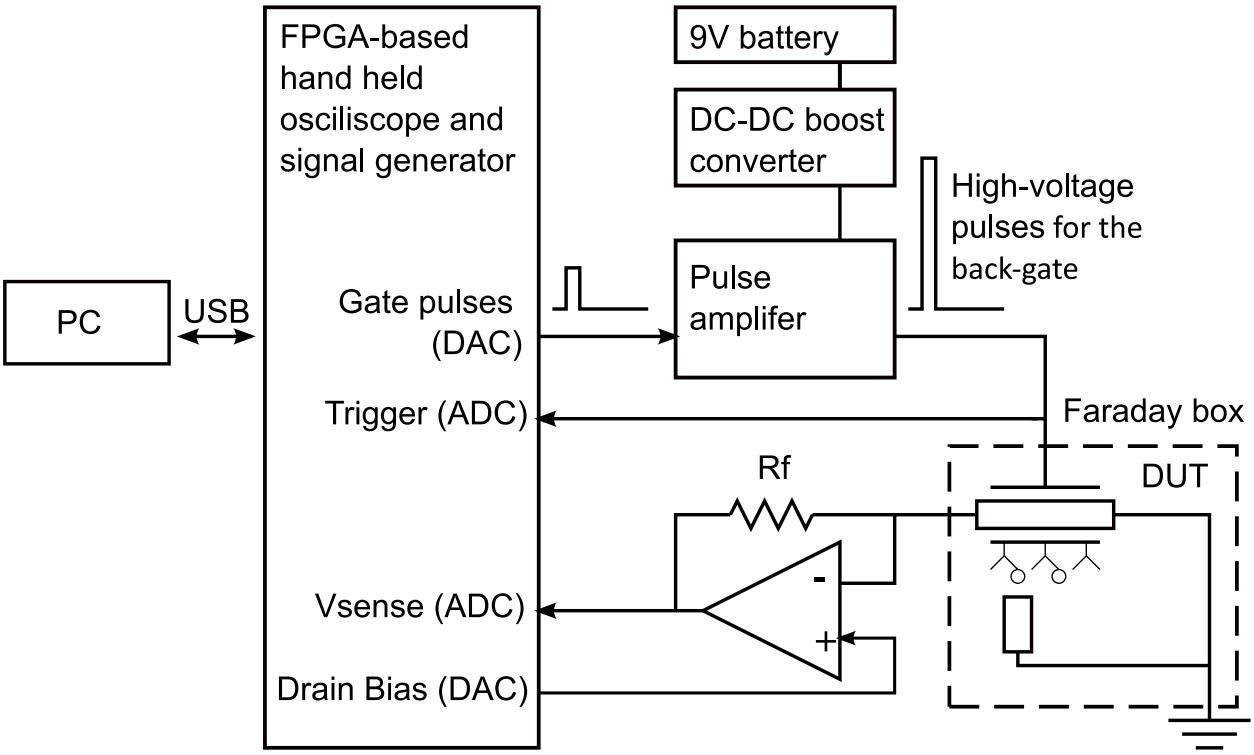

Figure 3.4: Schematic representation of the pulsed IV measurement system.

3.3 Results and Discussion

3.3.1 Drain Current Instability in a Normal Measurement

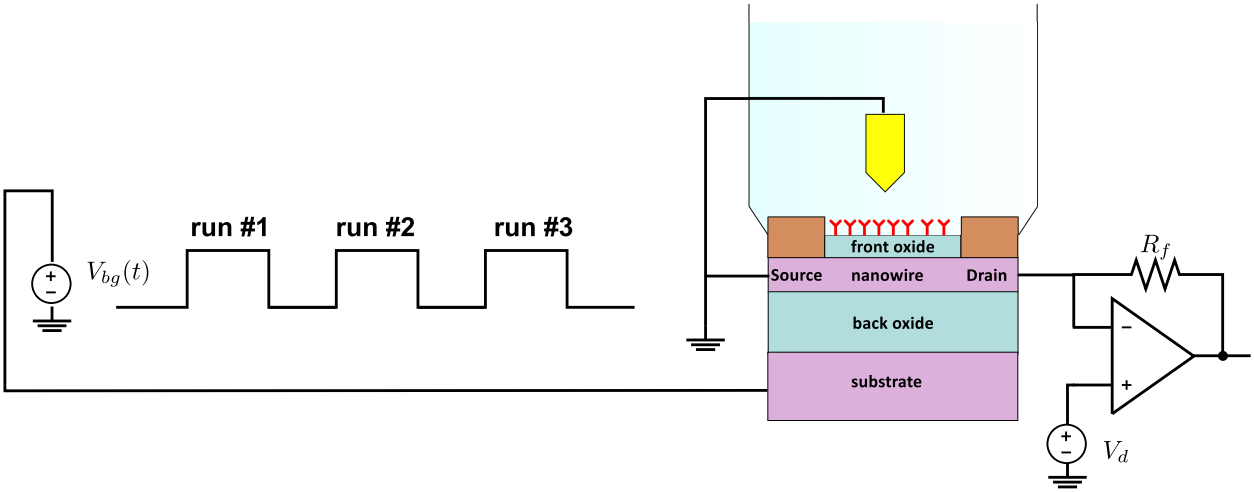

Figure 3.5: Schematic representation of the normal time-domain measurement. The device was biased in its linear regime with a positive back-gate DC voltage during the measurement phases and in the off-state in between with the back-gate terminal being grounded. Repeated measurements are labeled with different run numbers.

We illustrate a normal time-domain measurement in Fig. 3.5. The device was switched on and biased in its linear regime at the beginning of each measurement run with a high V_{bg} and a grounded front-gate through the reference electrode in the electrolyte. In between two consecutive measurement runs, the device was biased in the off-state with all its terminals connected to the ground. The device was biased above its threshold voltage to have a high signal gain during the measurement phases and biased in the off-state in between to avoid electrostatic discharge damage during the fluid transport, sample incubation, and washing processes. We, however, did not include them in this study to focus on instability behaviors associated with the device itself as they could further deteriorate the run-to-run variation. Diluted buffer solution (0.01xPBS) was supplied at a constant rate during the entire evaluation process.

Drain current instabilities were identified in the normal time-domain measurement as the signal drifting and irrepeatablility issues. The evaluation process consisted of multiple measurement runs defined by the back-gate biasing sequence, as illustrated in Fig. 3.6(a). Each run started at the rising edge of the V_{bg} and ended with its falling edge. Fig. 3.6(b) plots the measured drain currents in five consecutive runs, where the signal drifting was observed within each trace. The back-gate was biased with V_{bg}=15 V as the device had a typical back-gate threshold voltage around 7 V, as shown in Fig. 2.4 in the last chapter, and its drain terminal was biased to be 1 V. The time-dependent drain current change could be viewed as a combination of a fast and a slow response, which was similar to the previously reported ISFET instability behaviors [59, 102]. The initial current transient having a large magnitude became stabilized after a few tens seconds while the slow drifting persisted. We defined a sampling window of ten seconds at the end of each run and averaged the recorded current to be the sensor response of this particular measurement run, as marked in Fig. 3.6(b). Each measurement run had a duration of around a hundred seconds, which was determined as the current drifting within the sampling window fell within about 1% of its mean. The repeatability could be quantified with the spreading of these averaged current values among multiple runs, i.e., their run-to-run variation. The device could have achieved excellent repeatability even with a drifting signal if it presented the same transient in different runs, i.e., all traces overlapped together. Unfortunately, this was not the case as shown Fig. 3.6(b). We could, however, notice that the measured traces became more resembling its last preceding measurement with the increasing run numbers.

We hypothesized that the device characteristics changed due to the electric stress experienced in the measurement phases. We noticed that the drain current drifting was not continuous among multiple measurement runs and influenced by the removal of the high back-gate voltage. The drain current at the beginning of a following run was different from the end of the preceding one, which suggested that the device characteristics recovered, i.e., drifted in the opposite direction, when the back-gate terminal was grounded. The device

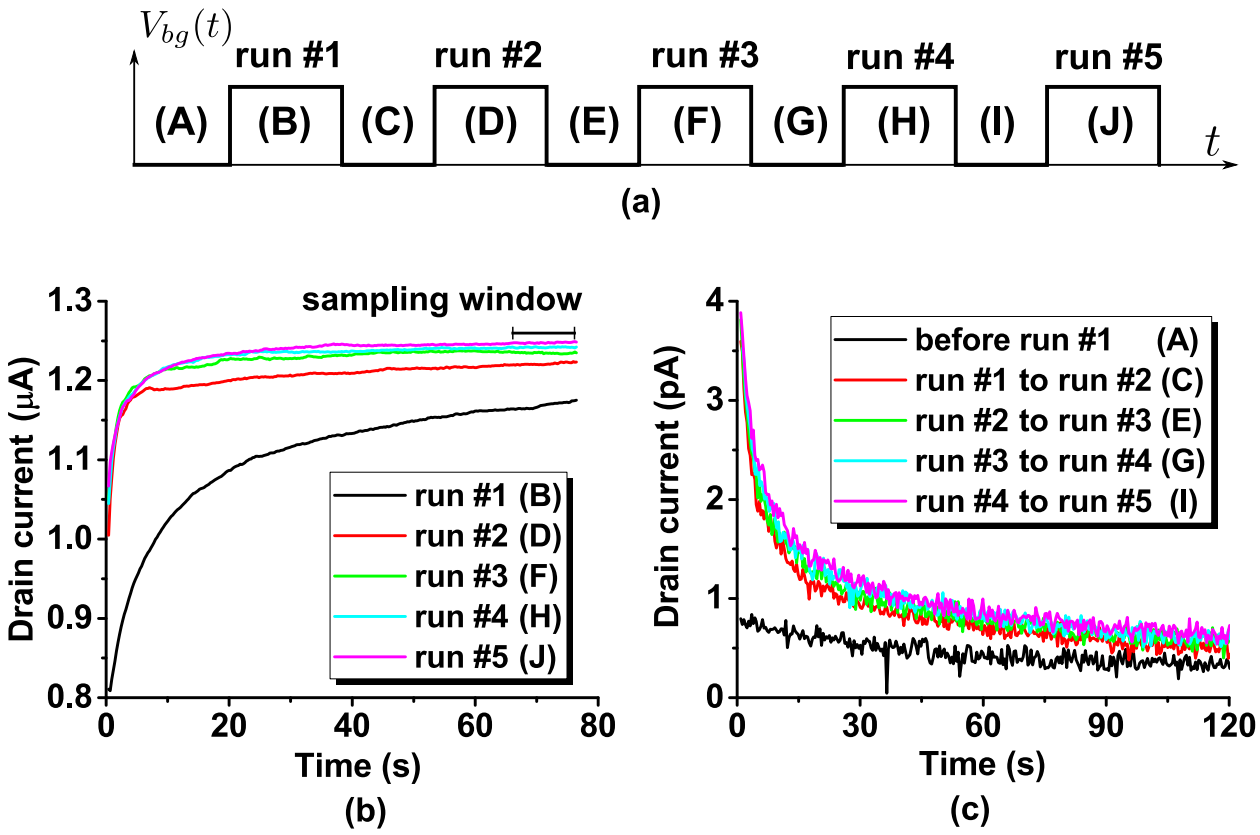

Figure 3.6: Typical drain current transients observed in the normal time-domain measurements: (a) Back-gate voltage timing diagram of an evaluation process consisting of five repeated measurement runs. The evaluation was divided into measurement and recovery phases by the V_{bg} and labeled with letters A to J. Measurement phases were also labeled with different run numbers. (b) Drain current instabilities in consecutive measurement runs showing both signal drifting and repeatability issues. (c) The drain currents recorded in between two runs (period C, E, G, and I) were considerably larger than the current measured before the first run (period A). The time-varying off-currents suggested that the device threshold voltage also drifted after each measurement run when the back-gate was grounded. The drain currents in (b) and (c) were measured within the labeled periods A-J as defined in (a).

could only partially recover before the subsequent measurement, leading to a different current level. To confirm the existence of a recovery process and observe its time scale, we applied a small drain voltage of 50 mV instead of 0 V in the normal time-domain measurement in between two runs and before the first run, measured its drain off-current, and plotted in Fig. 3.6(c). We observed a transient off-current having a similar time scale as of the on-currents in Fig. 3.6(b). The drain currents recorded in between two runs (period C, E, G, and I) were considerably larger than the current measured before the first run (period A), which clearly showed the existence of a recovery process.

3.3.2 Drain Current Responses to the Front- and Back-gate Biasing Changes

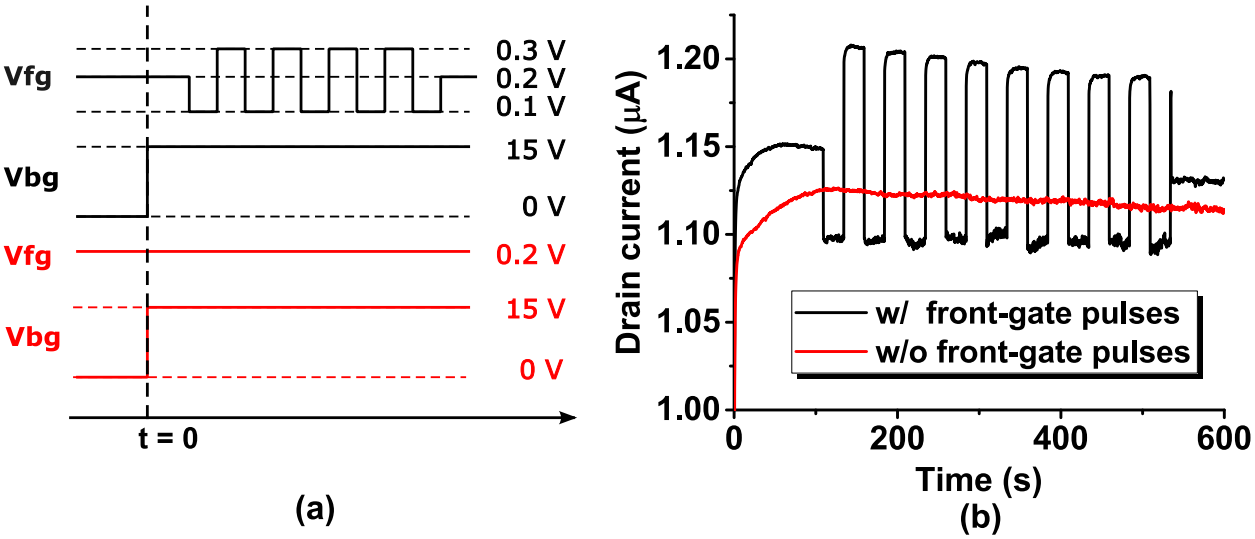

Figure 3.7: Drain current transients in response to gate bias steps: (a) The timing diagram of the gate biasing sequences. The back-gate voltages were changed at the beginning of the measurement, and a front-gate voltage pulse train was applied in one case (black) but not in the other (red). (b) Drain current responses recorded with and without front-gate pulses, showing that the transient associated with the back-gate voltage change took a longer time to settle down.

We examined the drain current response to a step-voltage change in the back-gate and the

front-gate biasing to identify the role of two gates in the observed instability behaviors. The drain currents were measured with the same back-gate bias and with or without a varying front-gate biasing sequence. Fig 3.7(a) illustrated the applied gate voltages. The back-gate voltage was changed from 0 V to 15 V at the beginning of the recording. We applied a constant $V_{fg} = 0.2$ V in one case and an voltage pulse train having a magnitude of 0.2 V after 100 seconds at the front-gate terminal in the other case. The drain current response to the front-gate voltage pulses was found superimposed onto a slower drifting due to the back-gate voltage change, which was also observed in the data measured without the pulse train V_{fg}, as shown in Fig. 3.7(b). They suggested that the biasing changes in two gates individually contributed to the drain current instability. The transient associated with the back-gate voltage change had a much longer time constant, which was more similar to what we had observed in the normal measurement. We, therefore, hypothesized that the back-gate biasing had a more critical role in the observed drain current instability.

3.3.3 Back-gate Current Transients

We further investigated the transient of the back-gate current in response to step-voltage changes to identify the physical mechanism responsible for the device instability. The back-gate current responses were first measured in the electrolyte solution. We applied a voltage step at the back-gate from 0 to V_{bg} at time zero and measured the gate current using the Keithley 4200 with the reference electrode being grounded, as illustrated in Fig. 3.8(a). Fig. 3.8(b) plots the measured back-gate and reference electrode current with $\Delta V_{bg} = 10$ V. We observed transient currents of opposite polarity on the reference electrode and back-gate lasted for tens of seconds. They together charged the capacitor formed by the electrolyte, back-gate insulator, and the substrate. We measured the back-gate current transients with different ΔV_{bg} and plotted results in Fig. 3.8(c) and (d). We found that the transient gate currents consistently showed a power-law time dependence decay, i.e., $i_{bg} \propto t^{-\alpha}$, where $\alpha \approx 0.7$ with all ΔV_{bg}. The traces labeled with $\Delta V_{bg} = 0$ V were recorded with no back-gate

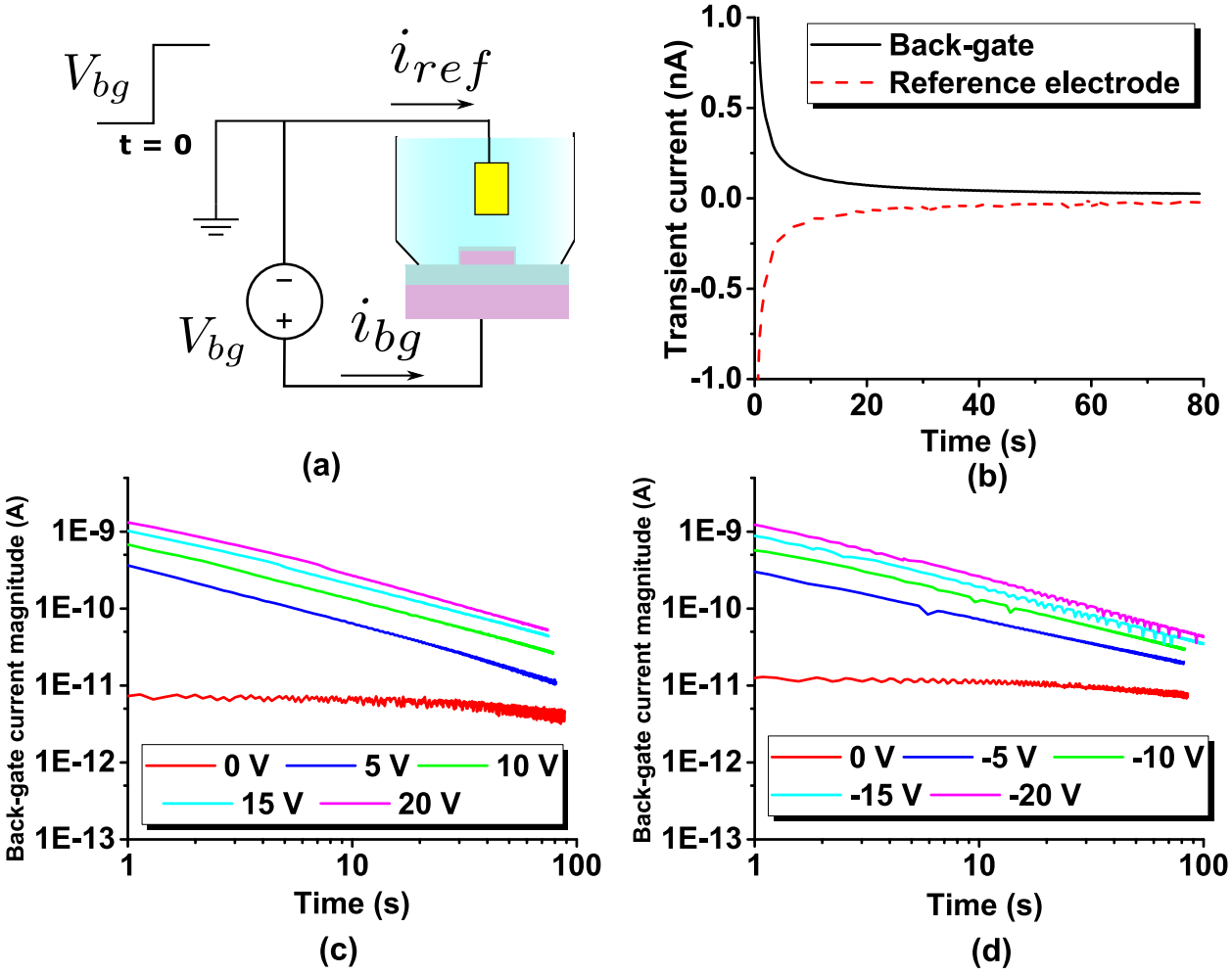

Figure 3.8: Back-gate current transients measured in the electrolyte: (a) Schematic representation of the measurement setup; (b) Opposite charging currents were observed in the back-gate and the reference electrode terminals; A power-law time dependence was observed with both (c) positive and (d) negative V_{bg}, suggesting the dispersive proton transport inside the back-gate oxide. The back-gate current magnitudes $|i_{bg}|$ were plotted in (c) and (d). Positive and negative ΔV_{bg} led to positive and negative back-gate currents with the current direction defined in (a).

Table 3.1: Parameters to estimate transient time constant associated with the electrolyte bulk resistance and the substrate resistance.

Notation	Value	Parameter
A_{open}	320 μm^2	Area exposed to the electrolyte
T_{BOX}	145 nm	Back-gate oxide thickness
$C_{bg,open}$	76 fF	Estimated back-gate capacitance
ρ_{sub}	8 Ω-cm	Substrate resistivity
T_{sub}	750 μm	Substrate thickness
R_{sub}	750 kΩ	Estimated substrate resistance
S_{ele}	0.015 S/m	Conductivity of 0.01x PBS
R_{ele}	44 MΩ	Estimated electrolyte bulk resistance

voltage change and indicated the limit of our electrical measurement system. The transient gate current magnitudes increased but not in proportion with the applied back-gate voltage, saturating at high $|\Delta V_{bg}|$.

Applied back-gate biasings established a vertical electric field in the back-gate oxide, changed the charge distribution of the electrolyte-(back-gate)-oxide-silicon stack, and induced the observed transient back-gate current. The slow decay gate current lasted tens of seconds and could be reasonably suspected as a result of charge redistribution associated with the oxide layer. Alternatively hypothesized rate-limiting mechanisms include ion transport inside the bulk electrolyte and the high resistance of the silicon substrate. They could be modeled with a RC model which predicted an exponential decay with the estimated time constant of 3.4 μs with $\tau = C_{bg,open}(R_{ele} + R_{sub})$ using values listed in Table 3.1. The nonexponential power-law time dependence suggested that the instability was associated with a trap-limited transport mechanism, known as dispersive transport, where the movement of the related species was controlled by traps having an exponential band-tail, which will be elaborated in the following section, and lead to a power-law time dependent

equivalent diffusivity [116]. Dispersive transport have been broadly observed in disordered materials [116–118, 120] and recognized as a signature of proton transportation in ISFET instability studies [100, 102, 119]. As similar V_{bg} were applied in the normal time-domain measurement, we would expect the same physical process happened and contributed to the drain current drifting as well.

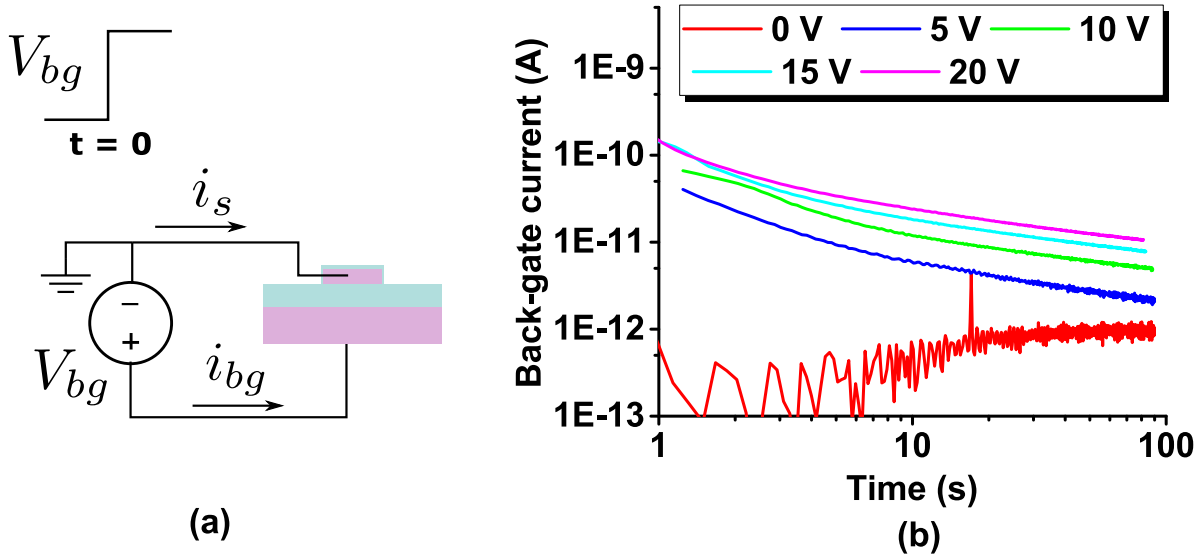

Figure 3.9: Back-gate current transients measured in dry condition: (a) Schematic representation of the measurement setup; (b) Measured back-gate currents with different V_{bg} showing again power-law time dependence.

We also measured the back-gate current transients in dry condition, where the FET source terminal was connected to the ground, as illustrated in Fig. 3.9(a). Measured back-gate currents with different ΔV_{bg} were plotted in Fig. 3.9(b). We observed again a power-law time dependence with $t > 5$ s. It suggested that the suspected protons were contained within the dielectric layer. instead of being driven into the dielectric from the electrolyte during the measurement phases. We suspected that protons were incorporated into the back-gate oxide during their exposure to water during the chip preparation and packaging processes. A faster decaying appeared at the beginning of the measurement ($t < 5$ s) whose origin was not completely clear. We suspected that it was the artifact from the instrument circuitry in

measuring such small current levels. We could notice that the trace measured with $V_{bg} = 0$ V in Fig. 3.9 presented abnormal fluctuations in the same period of time, which was not observed in Fig. 3.8(c) and (d).

3.3.4 Reference Electrode Stability

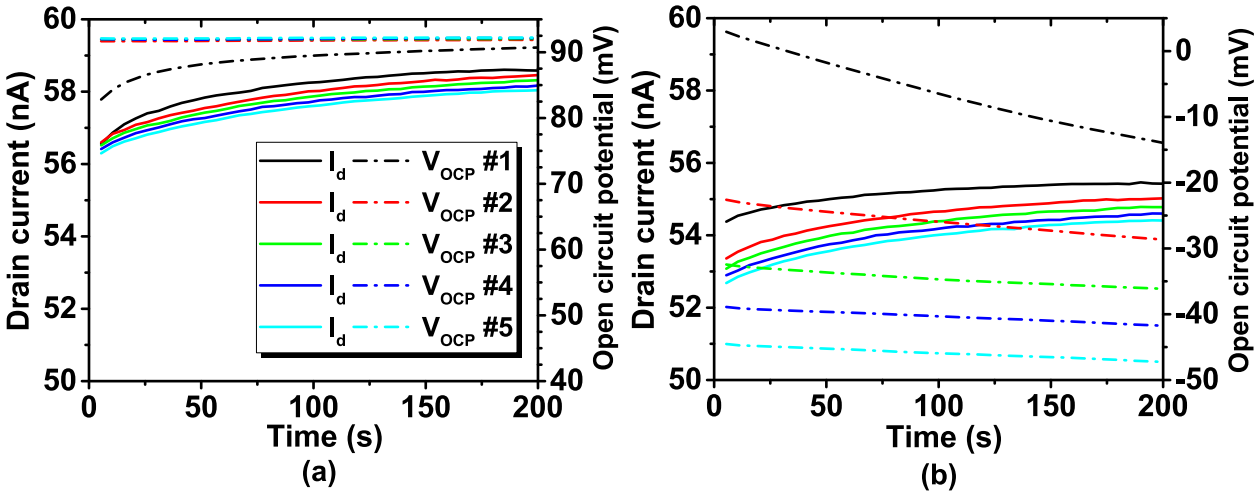

Figure 3.10: Stability of the reference electrode: Measured FET sensor drain current and the reference electrode open circuit potential (OCP) using (a) the employed Ag/AgCl electrode and (b) a Pt electrode. The employed Ag/AgCl electrode showed minimal drifting from the second measurement run, while the FET current showed transients having similar magnitudes in all five runs. Such uncorrelated behaviors between the reference electrode OCP and FET current drifting suggested that the reference electrode drifting was not the dominant instability mechanism in the studied devices.

Many have reported that the reference electrode drift was a significant contributor to the FET-based biochemical sensor instability [57, 104, 105]. We, therefore, evaluated the drifting of our reference electrode. We measured the open circuit potential (OCP) of the employed reference electrode using a second Ag/AgCl reference electrode (Basi MF-2052, United States) along with the FET drain current. The FET drain terminal was biased with $V_d = 0.1$ V. As shown in Fig. 3.10(a), the Ag/AgCl electrode OCP presented a prominent

transient in the first run but only drifted minimally (within 3 mV) in the following measurements. FET currents, at the same time, presented similar transients in every measurement run. Such uncorrelated behaviors suggested that the reference electrode drifting was not the dominant reason of the observed FET current instability.

Figure 3.10(b) plots the same evaluation performed with the same device and a Pt pseudo reference electrode. We observed a more severe drifting in the measured solution potential V_{OCP} as well as worse drifting in the FET current. The transients of the FET current still resembled those observed with the Ag/AgCl electrode suggesting again that the drift of the reference electrode was not the dominant instability source in our system. The reference electrode, however, could lead to a more significantly different current transient in the first measurement run from the remaining runs.

3.3.5 Instability Mechanism Analysis

We summarize here the instability behaviors observed in our dual-gated FET silicon biochemical sensors. A transient having a time scale of tens to a few hundred seconds was observed in the drain current in time-domain measurements. The measured transient had the most different behavior in the first measurement compared with the following runs, and they became more repeatable as we kept increasing the number of measurements. The drain current showed a transient response to either a front- or back-gate biasing change, and the transients associated with the back-gate voltage change was found to be slower. At the same time, a power-law time dependence was repeatably observed in the back-gate current transient on applying a step back-gate voltage change. The reference electrode also presented certain drifting and may contribute to the transient in the first measurement run. It, however, was determined not the dominant instability source.

Both the long time constant in the drain current transient and the power-law time dependence of the back-gate current transients suggested that the proton transport inside the back oxide played an important role in the studied device instabilities. Proton transporta-

tion in the oxide had been found a trap-assisted process [120], and their effective mobility was enhanced by rich defects close to the interface. It was hypothesized that these defects, i.e., proton traps, have a higher density near the electrolyte/dielectric interface because of the reactive ion etching employed in the fabrication process and its subsequent exposure to electrolyte [102]. The rich hydrogen distribution in the proximity of the interface had also been confirmed with the secondary-ion mass spectrometry (SIMS) and nuclear reaction analysis (NRA) profiling [121–123].

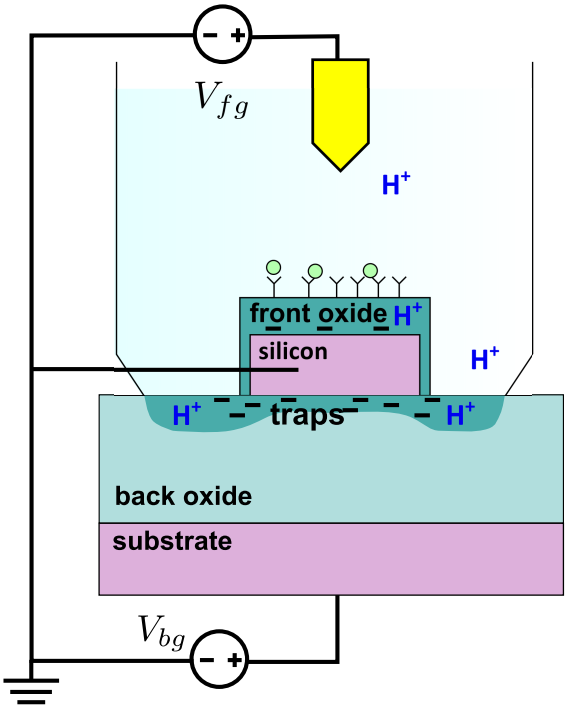

Figure 3.11: Schematic illustrating the hypothesized dielectric instability sources in the studied DG-FET structure. A hydrated defective oxide layer where protons could move with the assistant of rich traps was hypothesized in the back-gate oxide close to the electrolyte interface.

We hypothesized that such a defective layer could also form in the back oxide of the DG-FET, as illustrated in Fig. 3.11. We focused on the dielectric instability associated with the back-gate as a large back-gate voltage was used to form the inversion layer at

the back-gate oxide/semiconductor interface in the normal time-domain measurement while the front-gate could be kept grounded. The change of V_{bg} redistributed protons inside the hypothesized defective layer, changed its back-gate threshold voltage, and induced the drain current drifting. The observed instability of FET sensors is inherently governed by such charge distributions and their dynamics. We estimated that a redistributed proton of 7.4×10^{10} cm^{-2} equivalent surface density was needed to induce the drain current drifting of 200 nA that was observed in Fig. 3.6(b). Between two measurement runs, the proton and trap occupations could only partially recover to the original distribution and lead to a different transient in the following runs, causing the run-to-run variation.

3.3.6 Modeling the Dielectric Instability Associated with the Back-gate

In examining proton redistribution inside the back-oxide under a varying back-gate voltage, we studied a simplified 1D structure shown in Fig. 3.12. The silicon body is grounded through the source terminal and back-gate voltage is applied at the substrate. We did not include the proton redistribution inside the defective front-oxide, assuming that the front-gate was kept grounded and the voltage across the front-gate oxide did not change over time. This was, though, not completely true because of the applied drain voltage, and its implication need further investigation with a more complete model in higher dimensions. The presented simplified 1D model described device channel region close to the source terminal and its results remained only qualitatively true. We represented the inversion charge with a sheet charge of Q_{inv} at the silicon/oxide interface and the accumulated gate charge with Q_g in the substrate. Q_{it} represents the charge associated with the interface traps and H denotes the volumetric proton density. Protons were assumed to only move inside the defective oxide layer [102, 103] from $x = 0$ to $x = T_d$, as shown in Fig. 3.12. We did not model the oxide hydroxylation and assumed that ϵ_{ox} and T_d were constants within the simulated time scale. The sensor drifting caused by such oxide hydroxylation has been reported to be irrecoverable and have a time constant of hours [100], which is much longer than what we observed and

attempted to model in this study.

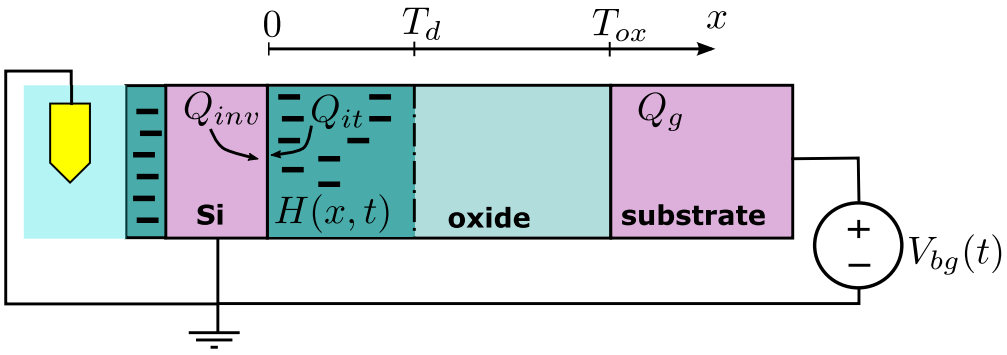

Figure 3.12: Schematic representation of the simplified 1D structure for simulating proton redistribution inside the back-oxide underneath the FET channel close to the source terminal. The effects of the defective front-oxide was not included assuming that the front-gate was grounded all the time. T_d represented the thickness of the hydrated defective oxide layer and T_{ox} was the total thickness of the back-gate oxide. Q_{inv}, Q_{it} and Q_g was inversion charge, interface trap charge, and gate charge respectively. Proton $H(x,t)$ redistribution was limited in the defective oxide layer, assuming that they had significantly smaller mobility in the intact oxide layer.

Assuming the device is operated as an enhancement-mode transistor, the drain current is proportional to Q_{inv} at the dielectric-semiconductor interface. The electrostatics in the oxide is governed by the Poisson equation and the following boundary conditions

$$\frac{\partial E_{ox}}{\partial x} = \frac{qH(x)}{\epsilon_{ox}} \tag{3.1}$$

$$\int_0^{T_{ox}} E_{ox} dx = -V_{bg} \tag{3.2}$$

$$Q_{inv} + Q_{it} = \epsilon_{ox} E_{ox}|_{x=0}. \tag{3.3}$$

Under a constant gate voltage bias, the effective back-gate FET threshold change ΔV_{th} could

be written as

$$\begin{aligned}\Delta V_{th} &= -\frac{\Delta Q_{inv}}{C_{ox}} \\ &= -\frac{\Delta Q_{it}(t)}{C_{ox}} - \frac{T_{ox}}{\epsilon_{ox}}\frac{1}{T_{ox}}\int_0^{T_{ox}} dx \int_0^x dsq\Delta H(s,t) \\ &\equiv \Delta V_{th,it} + \Delta V_{th,H}, \end{aligned} \tag{3.4}$$

where ΔX denotes the change of a physical quantity X with the reference to its initial value X_0. The first and second term represents the instability caused by the interface traps ($\Delta V_{th,it}$) and the proton redistribution ($\Delta V_{th,H}$) respectively. The corresponding drain current change is

$$\Delta I_d = -g_{m,bg}\Delta V_{th}, \tag{3.5}$$

where $g_{m,bg}$ is the back-gate transconductance, which could be estimated as a constant when the device is biased in its linear regime as in our experiments.

In response to the charge redistribution inside the oxide, carriers inside the channel Q_{inv} and the accumulated charge inside the substrate Q_g quickly adjust themselves so that the total voltage across the oxide remains a constant. A transient gate current is induced by the slow charge redistribution inside the oxide, and could be written as

$$i_g = \frac{\partial Q_g}{\partial t} = -\frac{\partial [Q_{inv} + Q_{it}]}{\partial t}, \tag{3.6}$$

and it is actually

$$i_g = -C_{ox}\frac{\partial \Delta V_{th,H}}{\partial t}. \tag{3.7}$$

Eq. 3.7 suggests that the transient gate currents reflect the proton redistribution inside the dielectric without being affected by the interface traps. Assuming Q_{inv} and Q_{it} have the same location, whether an electron at the interface is trapped does not affect the electrostatics in the studied structure and, therefore, does not contribute to the gate transient current. In another word, their effects on the gate current is screened by the quickly responding inversion charge.

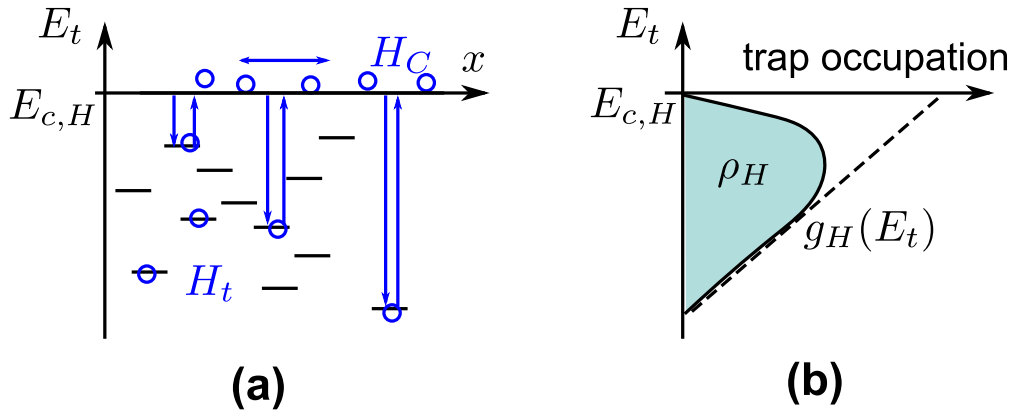

Figure 3.13: Schematic illustrations of the multiple-trapping model. (a) Protons consisted of free-moving conductive protons H_c and trapped protons H_t at different energy levels. The conductive protons with energy $E_{c,H}$ are assumed to be able to move in space by the drift and diffusion. Trapped protons redistribute through an energy-dependent trapping and de-trapping process. (b) Illustrated energy distribution of H_t. The total available proton traps are described by an equivalent density of states $g_H(E_t)$ and the energy distribution of trapped protons is represented by the trap occupancy ρ_H.

The transport of the proton was found a trap-controlled process featuring a dispersive behavior [124, 125]. We described the proton transport with the Multiple-trapping (MT) model following Grasser *et al.* [126]. In MT model, $H(x,t)$ consists of two components, conductive proton $H_c(x,t)$, which could move freely inside the dielectric, and those being trapped, $H_t(x,t)$, as illustrated in Fig. 3.13(a). Proton traps were assumed to have an energy distribution described by an equivalent density-of-state $g_H(E_t)$, and its occupancy ρ_H described the energy distribution of local H_t, as illustrated in Fig. 3.13(b). We could therefore write the total proton concentration $H(x,t)$ as

$$H(x,t) = H_c(x,t) + \int \rho_H(x, E_t, t) dE_t. \tag{3.8}$$

The dynamics of the trap occupation is governed by an energy-dependent trapping and

de-trapping process whose rates are given by the following equation

$$\begin{aligned}\frac{\partial \rho_H(E_t)}{\partial t} = \quad & \frac{\nu_H}{N_H}(g_H(E_t) - \rho_H(E_t))H_c \\ & -\nu_H \exp(-\frac{E_{c,H} - E_t}{k_B T_L})\rho_H(E_t),\end{aligned} \tag{3.9}$$

where ν_H is the attempt frequency, N_H is the effective hydrogen density-of-state, and $E_{c,H}$ is the energy level of the conductive protons. An exponential density-of-states is assumed

$$g_H(E_t) = \frac{N_{t,H}}{E_{0,H}} \exp\left(-\frac{E_{c,H} - E_t}{E_{0,H}}\right), \tag{3.10}$$

where $N_{t,H}$ is the total volumetric trap density and $E_{0,H}$ is its characteristic energy span. The transport of the conductive protons is governed by the following continuity equation

$$\frac{\partial H_c}{\partial t} = -\nabla \cdot F H_c + G_c, \tag{3.11}$$

where F is the flux operator and G_c is the generation rate. The flux of the conductive protons follows the drift and diffusion equation and its generation rate G_c could be evaluated by integrating Eq. 3.9 over the energy. After a long enough time, the local volumetric trapped proton density will, in theory, become in equilibrium with the conductive hydrogen H_c, and its density could be estimated as

$$\begin{aligned}H_{t,est} &= \int_{-\infty}^{E_{d,est}} g_H(E_t) dE_t \\ &\quad + \int_{E_{d,est}}^{E_{c,H}} \frac{H_c}{N_H} g_H(E_t) \exp(\frac{E_{c,H} - E_t}{k_B T_L}) dE_t \\ &= N_{t,H} \exp(-\frac{E_{c,H} - E_{d,est}}{E_{0,H}}) + \\ &\quad \frac{H_c}{N_H} \frac{N_{t,H}}{1-\alpha} \left\{ \exp\left[(1-\alpha)\frac{E_{c,H} - E_{d,est}}{E_{0,H}}\right] - 1 \right\},\end{aligned} \tag{3.12}$$

where $\alpha = k_B T_L / E_{0,H}$, and $E_{d,est}$ is the estimated equilibrium demarcation energy given by

$$E_{d,est} = E_{c,H} - k_B T_L \ln(N_H / H_c). \tag{3.13}$$

Above estimation was a convenient tool to set up the initial condition in our simulation as shown in the following section.

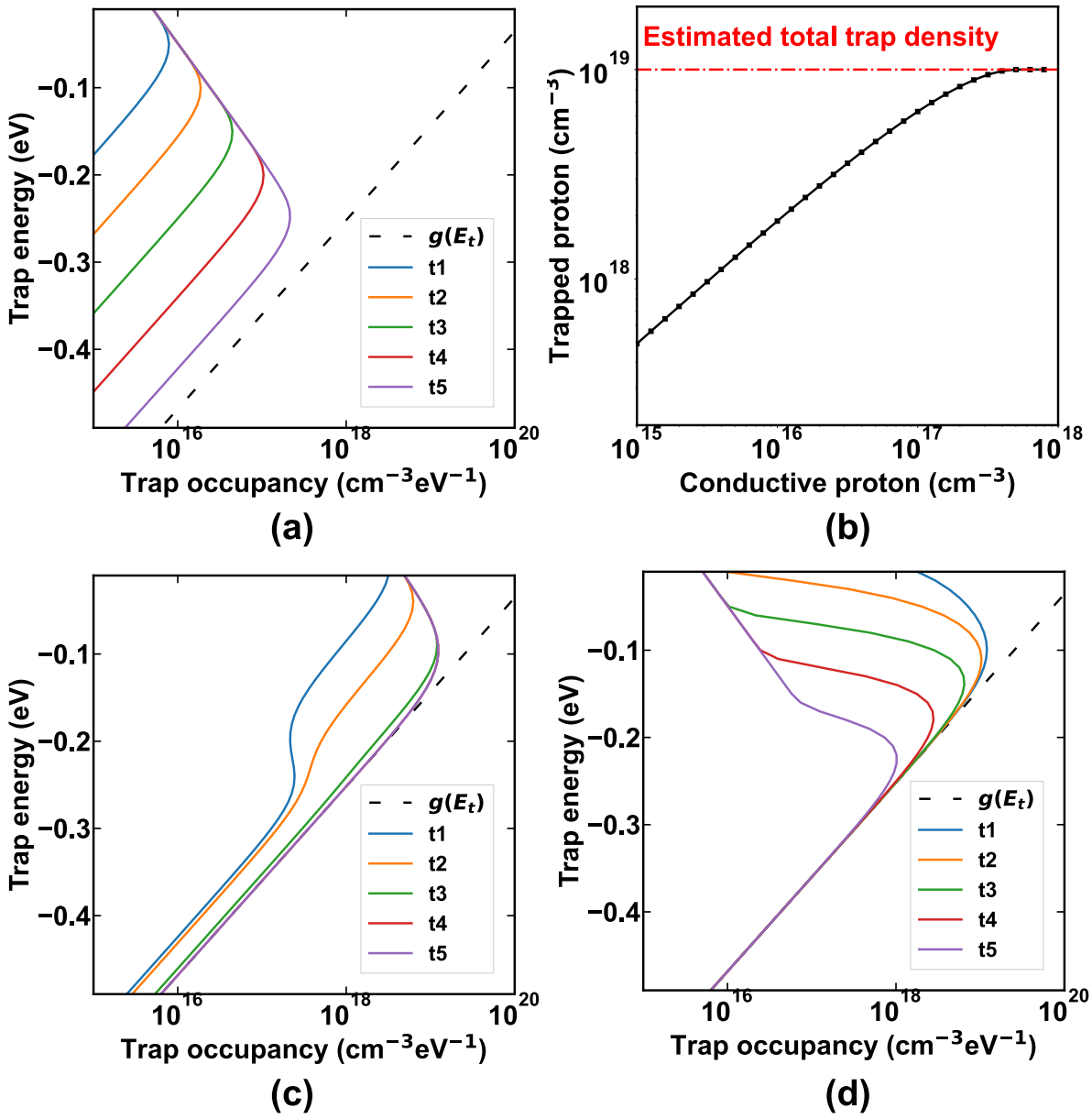

Figure 3.14: Dynamics of the proton traps in the simulated defective oxide: (a) Evolution of the trap occupation in charging empty traps with a constant H_c of 1×10^{13} cm^{-3}. Trap occupation forms a peak because of the energy-dependent trapping and de-trapping rate. (b) Estimated equilibrium trapped proton density $H_{t,est}$ as a function of H_c. The red dashed line showed the assumed total trap density. Evolution of ρ_H with a H_c step-change (c) from 1×10^{13} cm^{-3} to 1×10^{16} cm^{-3}, and (d) from 1×10^{16} cm^{-3} back to 1×10^{13} cm^{-3}. t_1 to t_5 are increasing time stamps after H_c changes.

We first examined the dynamics of proton trapping and de-trapping process with a change in H_c. Fig. 3.14(a) shows how traps are occupied from an initially all empty state with a constant conductive proton concentration H_c of 1×10^{13} cm^{-3}. The energy distribution of trapped protons are plotted at increasing time stamps from t_1 to t_5 along with the proton trap density of states as the dashed line. Trap occupancy forms a peak in its energy distribution due to the energy-dependent capture and release rate, which divides the traps into deep and shallow traps. Shallow traps have an increasing occupancy with deeper energy levels for a certain conductive proton concentration H_c as the capturing and releasing processes are balanced at different E_t. Deep traps, in contrast, have significantly higher capture rate than the release rate because of their large energy difference $|E_t - E_{c,H}|$, and therefore have an occupancy following the shape of $g_H(E_t)$. The trapped protons ultimately become equilibrium for each local conductive proton density H_c. The total trapped proton densities with different H_c was estimated with Eq. 3.12 and plotted in Fig. 3.14(b). $H_{t,est}$ follows H_c until all available trap states are filled, which is marked with the red horizontal line in Fig. 3.14(b). On increasing and decreasing of the H_c, H_t and its energy distribution change accordingly. Fig. 3.14(c) and (d) plot the evolution of the trap occupation in an up-step and down-step H_c change, showing ρ_H peak moves up and down. We could observe that the shallow traps are more responsive to the instantaneous H_c changes, while deep traps had slow responses and distorted the ρ_H. The transport of the proton in oxide is prominently affected by these traps, leading to a dispersive behavior. Though proton traps are immobile, H_t could still be spatially redistributed under different biasing conditions as the conductive proton spatial distribution changes promote above trapping and de-trapping processes.

We then simulated the dynamics of the proton redistribution in response to the back-gate bias change in the studied structure using the FDTD Method. At each time step, we updated $H_c(x,t)$ and $\rho_H(x,t,E_t)$ according to their changing rate and evaluated the effective back threshold voltage changes. Referring to Fig. 3.12, we assumed the defective layer has a thickness of 5 nm and zero flux at two boundaries. The Scharfetter-Gummel discretization

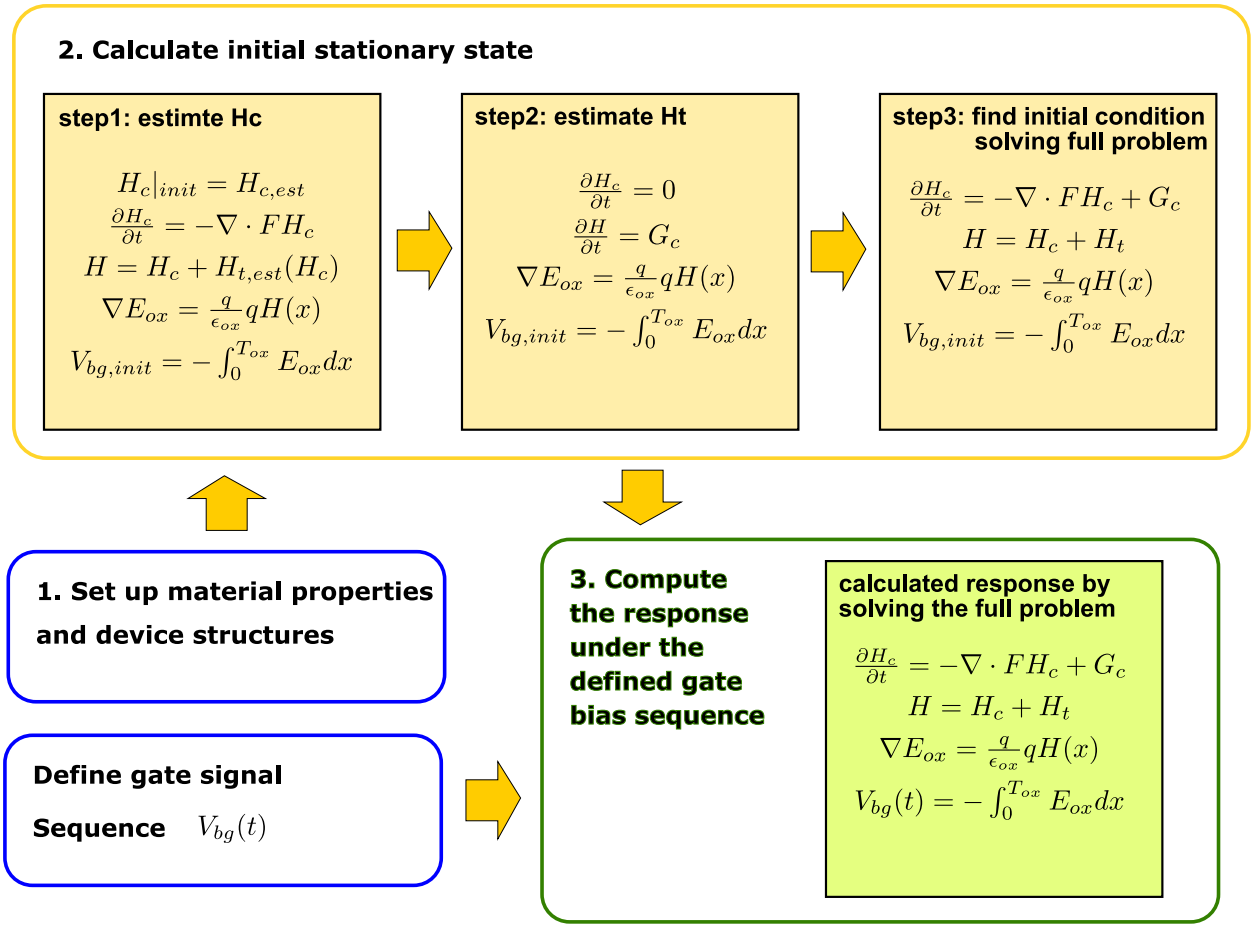

Figure 3.15: Schematic showing the FDTD simulation flow.

was implemented to evaluate conductive proton flux governed by the drift and diffusion equations. Fig. 3.15 shows the detailed simulation steps to obtain the self-consistent solution of the coupled equations. After setting up material properties, the simulator first attempted to find a stationary state under the initial bias before the measurement, assuming $V_{bg} = 0$ V. We divided this process into three separate steps as direct solving the full problem was challenging and did not converge. We first calculated a $H_c(x)$ distribution with the estimated H_t from Eq. 3.12, where $H_{t,est}$ helped to approximate the correct electrostatic inside the back-oxide. In the second step, we obtained a better estimation of the trapped proton ignoring any conductive proton flux. The energy distribution of the trapped protons was also constructed at this step. We then solved the full problem with above estimated $H_c(x)$ and $\rho_H(x, E_t)$

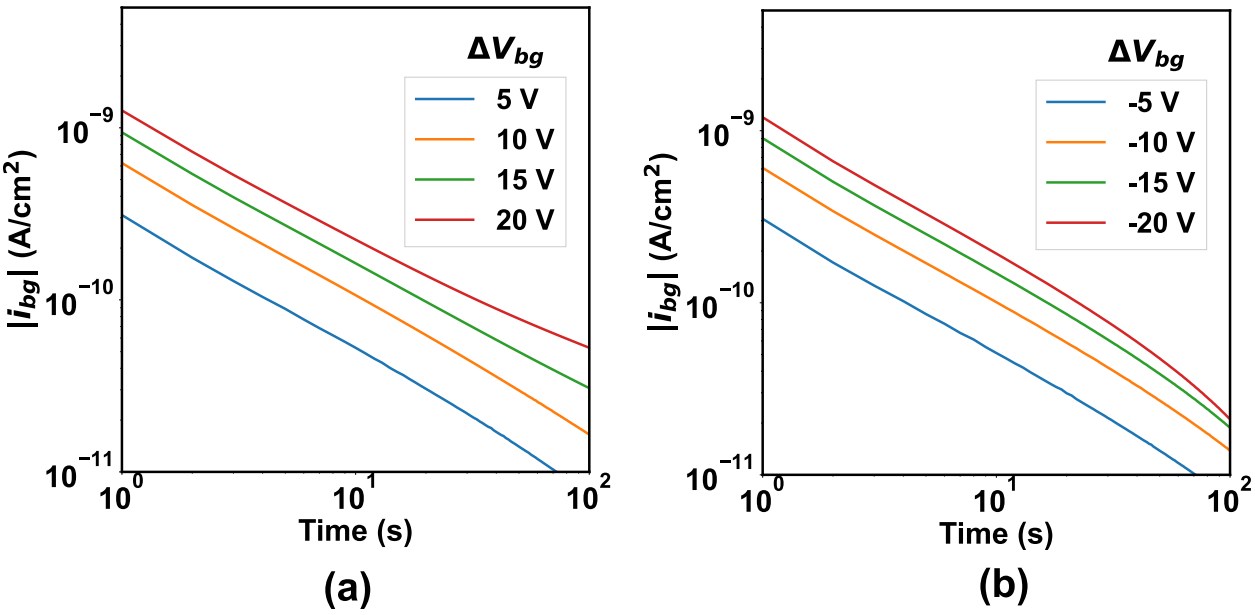

Figure 3.16: Simulated back-gate current transients due to proton redistribution inside the defective oxide layer under (a) positive and (b) negative back-gate step-voltage change, showing power-law time dependence as observed in the experimental data.

as the initial condition. We monitored the change rate of the effective threshold voltage under the initial biasing condition until it reduced to a negligible magnitude. Following such a procedure, we found the stabilized state corresponding to the situation where the device under test had been connected to the ground for an extended period of time.

We first simulated the back-gate current transients in response to the back-gate step-voltage changes to check the capability of our simulator. We assumed a constant voltage of V_{bg} from time zero in the simulation and tracked the proton redistribution. This was equivalently to applying a step voltage change ΔV_{bg} as the initial solution was established with $V_{bg} = 0$ V. The equivalent back-gate threshold voltage change due to proton distribution was evaluated at each time stamp, and the back-gate current was proportional to its changing rate and obtained with Eq. 3.7. We plotted the simulated back-gate current magnitudes in Fig. 3.16. The simulator was able to reproduce the observed power-law time dependence for both positive and negative ΔV_{bg}. On applying V_{bg}, conductive protons were moved by

the applied electric field. The varied local H_c disturbed the trap occupations at different locations in a process similar to what was shown in Fig. 3.14(c) and (d), and changed the total proton (H_c and H_t) spatial distribution. Gate-current transient in response to positive and negative ΔV_{bg} had similar magnitudes as the proton redistribution was assumed to be inside the defective oxide with zero flux boundary conditions at both interfaces. An opposite V_{bg} polarity inverted the electric field and the direction of the subsequent proton redistribution process, but had limited effect on the proton redistribution dynamics. We should point out that the simulated structure in Fig. 3.12 was different from the two-terminal measurement set-up in Fig. 3.8(a), where the electrolyte was used as the ground terminal instead of the silicon channel. As the dominant physical mechanism, proton redistribution, happened inside the oxide, such a difference shall not affect the qualitative behavior of the simulation results.

We proceeded to simulate the drain current transient due to proton redistribution under a back-gate bias sequence mimicking the applied biasing during the normal time-domain measurement. Fig. 3.17(a) show the assumed back-gate voltage biasing sequence, which sets $V_{bg} = 15$ V during the measurement phases. We assumed that measurement runs last for 100 s and are separated by 100 s as well. We loaded the established initial proton distribution and the trap occupation into the simulator and tracked their evolution under the assumed back-gate biasing sequence. The effective back-gate threshold voltage change $\Delta V_{th,H}$ was evaluated at each time step. Fig. 3.17(b) to (d) show the snapshots of the simulated total proton densities, conductive proton densities, and electrostatic potential in the defective oxide layer at the beginning of the first run, the end of the first run, and the beginning of the second run, respectively. The varying electric field changes both the conductive and trapped proton distributions. Comparing Fig. 3.17(d) with (b), we could notice that the conductive proton failed to recover to its initial profile as trapped protons did not respond fast enough during the recovery period and, therefore, changed the electrostatics.

We calculated the drain current change in five measurement runs from the simulated $\Delta V_{th,H}$ using Eq. 3.5, and plotted the results in Fig. 3.18. We assumed that the device was

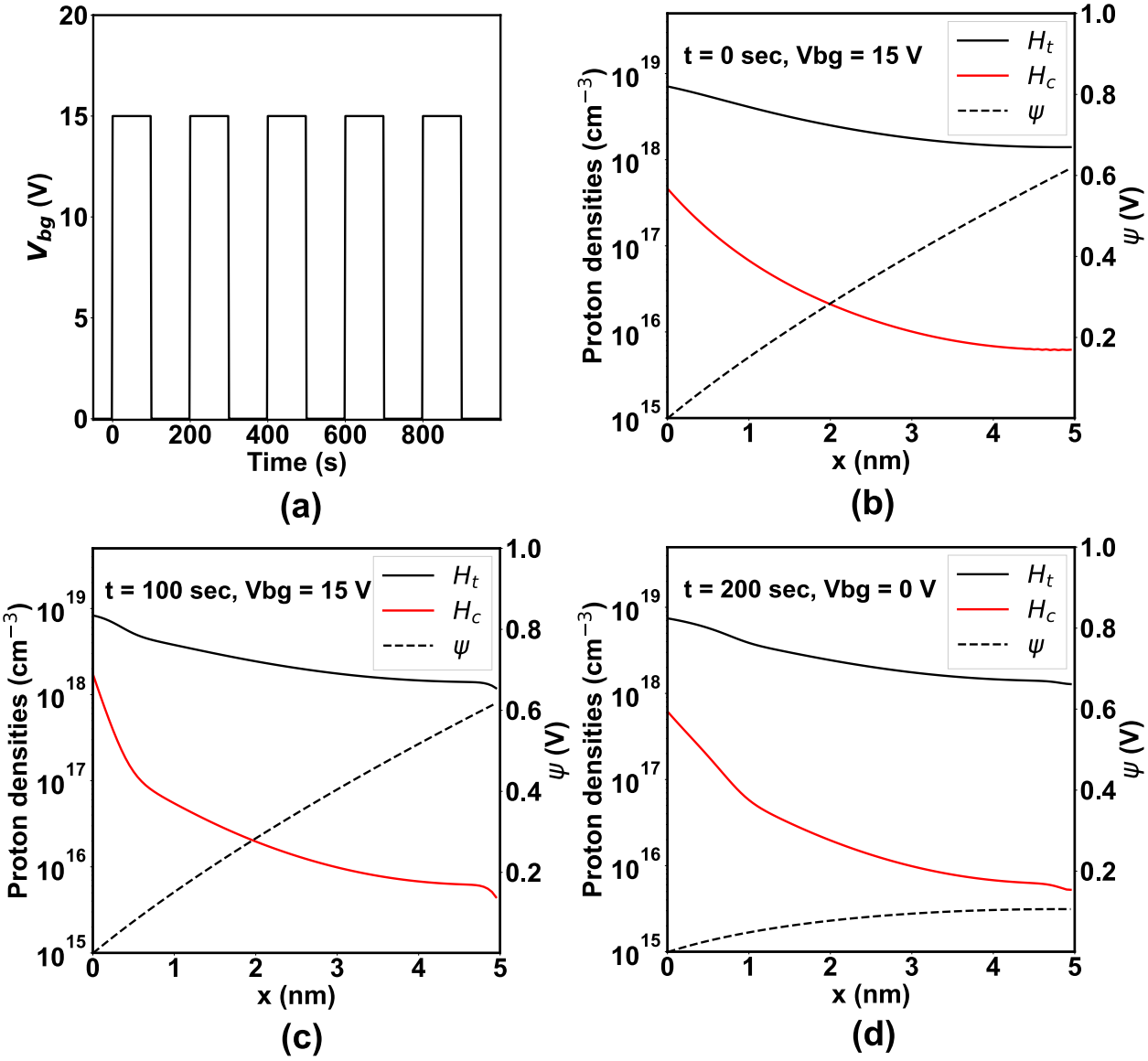

Figure 3.17: Simulated proton redistribution inside the defective layer under the varying back-gate biasing voltages: (a) The timing diagram of the back-gate voltages used in the simulation. V_{bg} was assumed to be 15 V during the measurement phases and 0 V in between two runs. Measurements were assumed to last for 100 s and separated by 100 s. Simulated trapped proton H_t and conductive proton H_c distribution and electrostatic potential ψ at (b) the beginning of the first measurement run (t=0 s), (c) after the first run (t=100 s), and (d) at the beginning of the second measurement run (t=200 s). Notice the difference of H_c and H_t in (b) and (d), illustrating that the system did not recover in time.

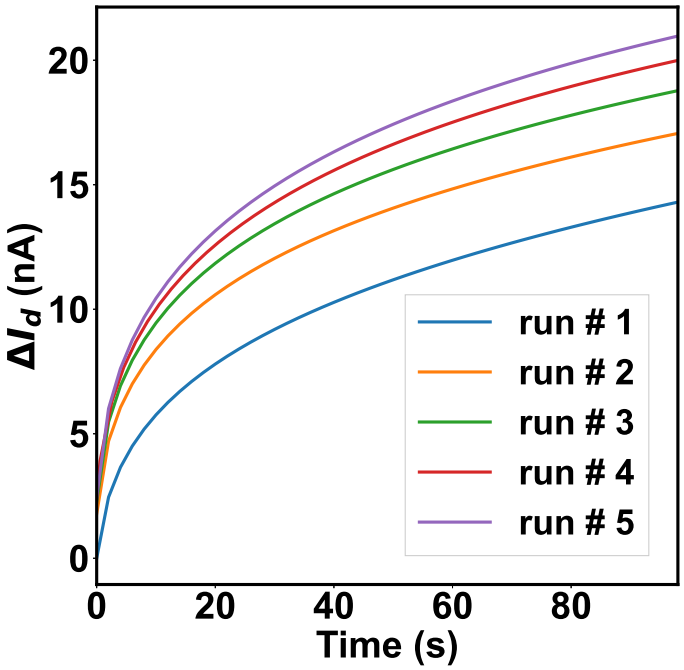

Figure 3.18: Simulated drain current drifting due to the proton redistribution. It showed more resembling transients in later measurement runs, a behavior similarly identified in the experimental data.

biased in its linear regime and had a typical back-gate transconductance of 400 nA/V. We observed that the first transient curve was the mostly different from the remaining runs, but they become increasingly resembled among the following runs as in the experiment data in Fig. 3.6(b). The system did not recover back to the very initial state before the second measurement run, and, therefore, generated a different transient, as illustrated in Fig. 3.17(b) and (d). However, under a periodic biasing, the proton density would ultimately evolve between two specific spatial distributions, which could be both different from its initial profile and generate repeatable transients during the measurement phases because the transients were determined by its evolution over time. The system could then be considered in a periodic steady state. The increasingly resembling transient was a result of the system being gradually driven into such a periodic steady state.

3.3.7 Strategies to Mitigate the Effects of the Instability

The observed instability of FET sensors is inherently governed by the charge distribution in the dielectrics and their dynamics under the varying biasing conditions. In theory, a stationary state, where the drifting is minimal, does exist under each DC biasing. Reaching these stabilized states, however, requires a long waiting time in both the measurement and recovery phases. They could significantly prolong the total assay time. Besides, the waiting time period to stabilize the FET senor varies from one device to another, and it is hard to decide the exact waiting time during a specific sensing experiment. A dynamic biasing using pulses could be a better choice compared with the normal measurements using DC biasing. A time-varying biasing during the measurement phase could drive the system into a periodic steady state in a shorter time, and provide opportunities to both reduce the drifting and run-to-run variations. We explored two pulse biasing techniques and demonstrated their effectiveness in counteracting the device instability in the following sections.

3.3.7.1 Pulsed IV Measurement

We first examined the pulsed IV measurement. The device under test was biased with a pulse train having short pulse width and small duty cycles at the back-gate terminal, as illustrated in Fig. 3.19. We recorded the FET drain current with a much higher sampling rate than the pulse repetition frequencies using the pulsed IV system described in the previous experimental methods section. We calculated a representative current signal for a single pulse by averaging the last ten measured current values before its falling edge. This averaged current was recorded over time and equivalently formed a time-domain measurement, as illustrated in Fig. 3.19. We expected that the system presented little drifting as the pulsed back-gate voltage minimally disturbed the charge distribution from its initial state. The dielectric experienced electrical stresses only with a fractional of the total measurement time compared with the normal DC time-domain measurement. A small duty cycle also helped

its recovery.

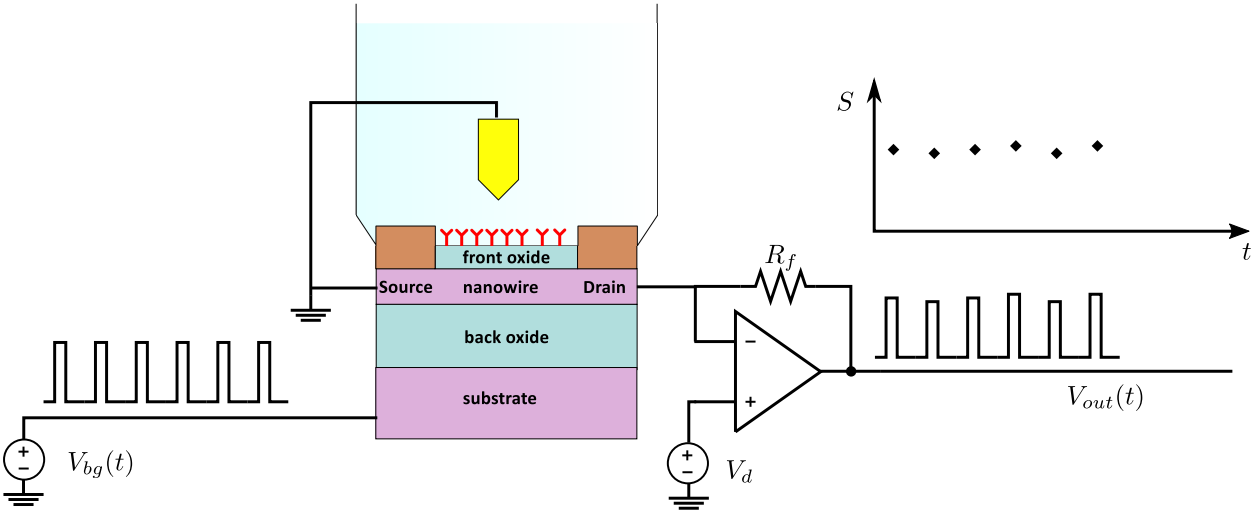

Figure 3.19: Schematic representation of the pulsed IV measurement: A pulse train was applied at the back-gate of the device, and the FET current response to each pulse was used to calculate a single data point in the output signal. These values formed an equivalent time-domain measurement having a sampling rate of the applied pulse repetition frequency.

We first measured the drain current response to the single back-gate pulse in the dry condition. We applied pulses having the pulse width from 200 μs to 20 ms and the total period of 200 ms. The device had a turn-on transient of a few milliseconds regardless of the applied pulse widths, as shown Fig. 3.20(a). Pulse widths longer than 2 ms were therefore preferred as the averaged current would be more vulnerable to the phase noise in the driving gate signal when smaller pulse widths were used. We show the time-domain measurement results using different pulse widths in Fig. 3.20(b). Little transient was observed in every trace, indicating that the charge could recover from the minimal disturbance even with the maximal applied pulse width of 20 ms. It was also interesting to notice that a non-drifting signal could be obtained even with short pulse widths (e.g. pulse widths less than 2 ms) where the instantaneous signal was not stabilized within each individual pulse. It is worth noting that the absence of the drifting was not because they were measured in dry

condition. Reported devices had been exposed to the electrolyte and showed drifting drain currents when measured with DC back-gate biasing.

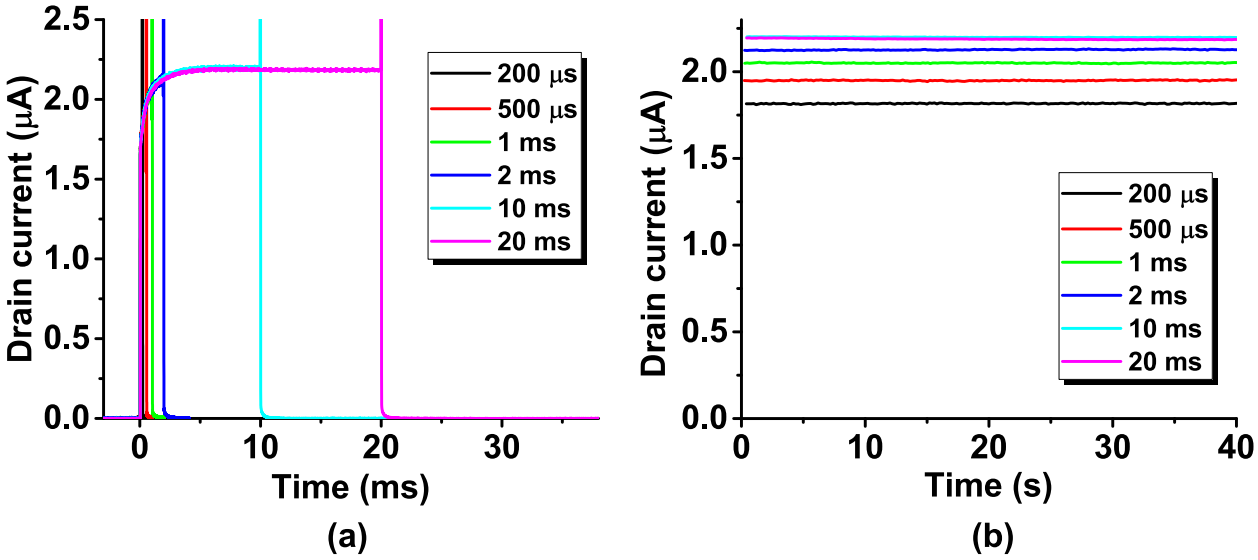

Figure 3.20: Pulsed IV measurement results in dry condition: (a) Typical FET current responses to a singe pulse of the labeled pulse width. (b) The equivalent time-domain current signal measured with the back-gate pulse train having the labeled pulse width and a repetition rate of 5 Hz, showing minimal drifting. Each data point in (b) was obtained by averaging the last 10 sampled data points in FET drain current response to each single pulse in the applied pulse train before the V_{bg} falling edge.

We then proceeded to measure the pulse responses in aqueous condition. Fig. 3.21(a) shows the current responses to a single back-gate pulse having different pulse widths. The drain current also showed a turn-on transient of a few milliseconds as in the dry condition measurement. The presented device, however, showed a current overshoot. Such behavior was only observed in only some of the tested devices. While its physical origin need further investigations, we suspected that it was related to the traps and leakage of the front-gate oxide, whose quality varied among different tested devices. The averaged equivalent time-domain pulsed IV measurement results are plotted in Fig. 3.21(b). We also measured the same device under the same DC back-gate voltage and plotted its drain current as the

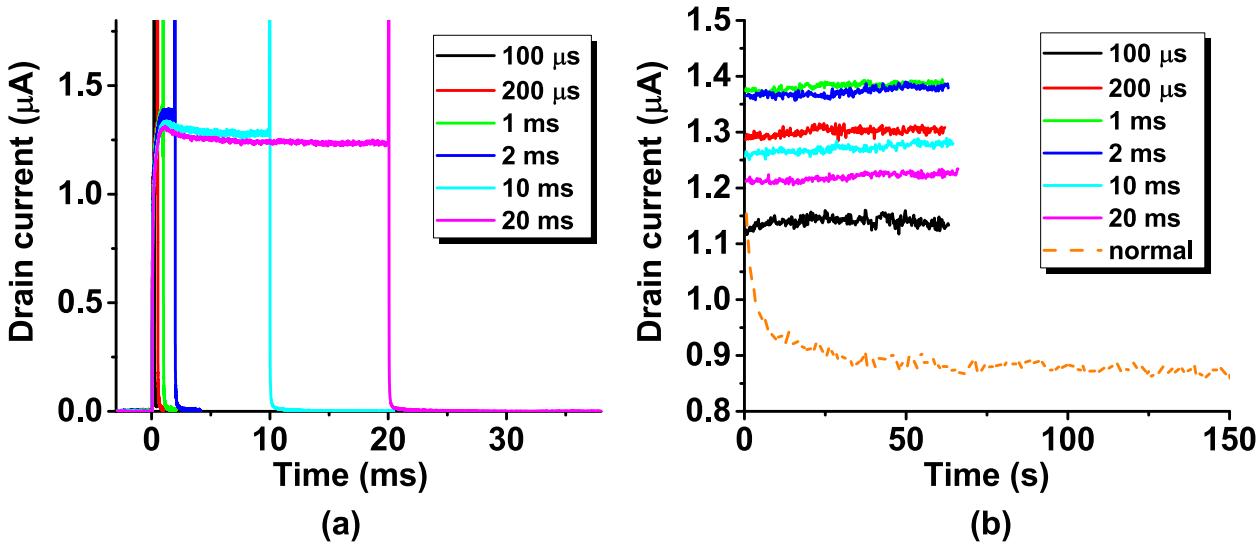

Figure 3.21: Pulsed IV measurement results in aqueous condition: (a) Typical FET current responses to a singe pulse of the labeled pulse width. (b) The equivalent time-domain current signal measured with the back-gate pulse train having the labeled pulse width and a repetition rate of 5 Hz along with a normal DC-biased measurement shown as the dashed line, showing that the pulsed IV measurement significantly reduced the current transient. Each data point in (b) was obtained by averaging the last 10 sampled data points in FET drain current response to each single pulse in the applied pulse train before the V_{bg} falling edge.

dashed line in Fig. 3.21(b) among the pulsed IV measurement results. We observed that the pulsed IV measurement significantly suppressed the current transients and drifting. Such drifting reductions corroborated our hypothesis that the charge redistribution is the major mechanism for the observed instability behaviors.

3.3.7.2 Pulse Resetting

The second measurement technique used a pulse sequence preceding a normal time-domain measurement to reset the system. As illustrated in Fig. 3.22, we applied a pulse back-gate sequence and performed a normal DC-biased time-domain measurement immediately

afterward. We expected that the alternating back-gate bias could quickly drive the charge distribution into a particular periodic steady state so that a more repeatable transient could be obtained in the following normal measurement.

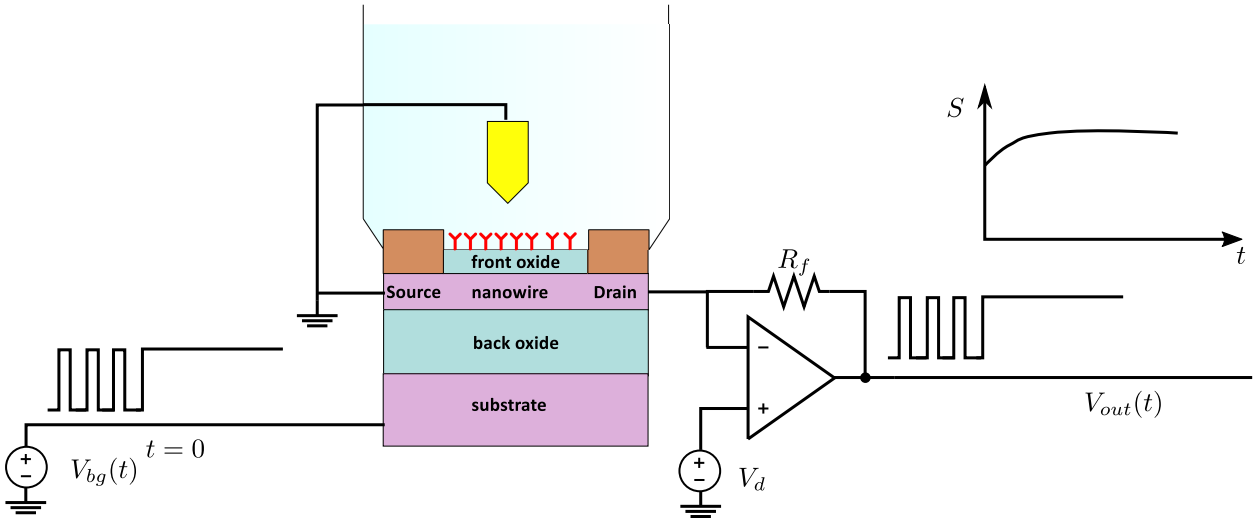

Figure 3.22: The schematic representation of the pulse resetting. A pulse train was applied before a normal time-domain measurement as a resetting sequence. The FET current was recorded from the last step-up change of V_{bg} in each measurement run. The same resetting was repeated for multiple measurement runs.

We validated the effectiveness of the pulse resetting by measuring devices multiple times in 0.01xPBS with and without the pulse resetting, and summarized results in Fig. 3.23. In measurement without the resetting, we measured the device for 160 seconds with a 200 seconds resting period in between for five times and plotted the drain current transients in Fig. 3.23(a). The same device was then measured under the same DC biasing voltage but with a pulse resetting sequence before each measurement run. The measured transients were plotted in Fig. 3.23(b). We noticed that current transients measured from run 2 to 5 became more repeatable and almost overlapped. The transient in the first run, though, was still very different, which was attributed to the reference electrode instability. We compared their run-to-run variations by calculating the standard deviations among the last four runs.

We again extracted the averaged current in the last 10 s as the signal for each single run and plotted these values in Fig. 3.23(c). The error bars represented the standard deviation of these averaged drain currents, which was equivalently the baseline fluctuation in blank sample measurements. It clearly showed that the standard deviation was reduced thanks to the pulse resetting technique. We repeated the same evaluation with another three devices and showed the extracted standard deviations in Fig. 3.23(d). We found the pulse resetting technique consistently reduced their run-to-run variations and improved the repeatability.

3.4 Summary

To summarize, we have studied the instability of our DG-FET biosensor. We found the dominant instability source associated with the back-gate biasing change and hypothesized it was a result of charge redistribution inside a defective layer of the back oxide. We simulated the threshold voltage instability using a macroscopic model describing the dispersive proton transportation under different electric bias and compared its results with the experimental observation. Our analysis suggested that the signal drifting could arise from the proton redistribution, and its failure to recover to the original state could cause the repeatability problem. We proposed to use pulse biasing schemes to improve the device stability and reduce their effects in the measurement uncertainties. We explored two different biasing strategies: pulsed IV measurement and pulse resetting. We demonstrated that the pulsed IV measurement significantly suppressed the drain current drifting during the measurement phase and the pulse resetting reduced the run-to-run variations among multiple measurement runs.

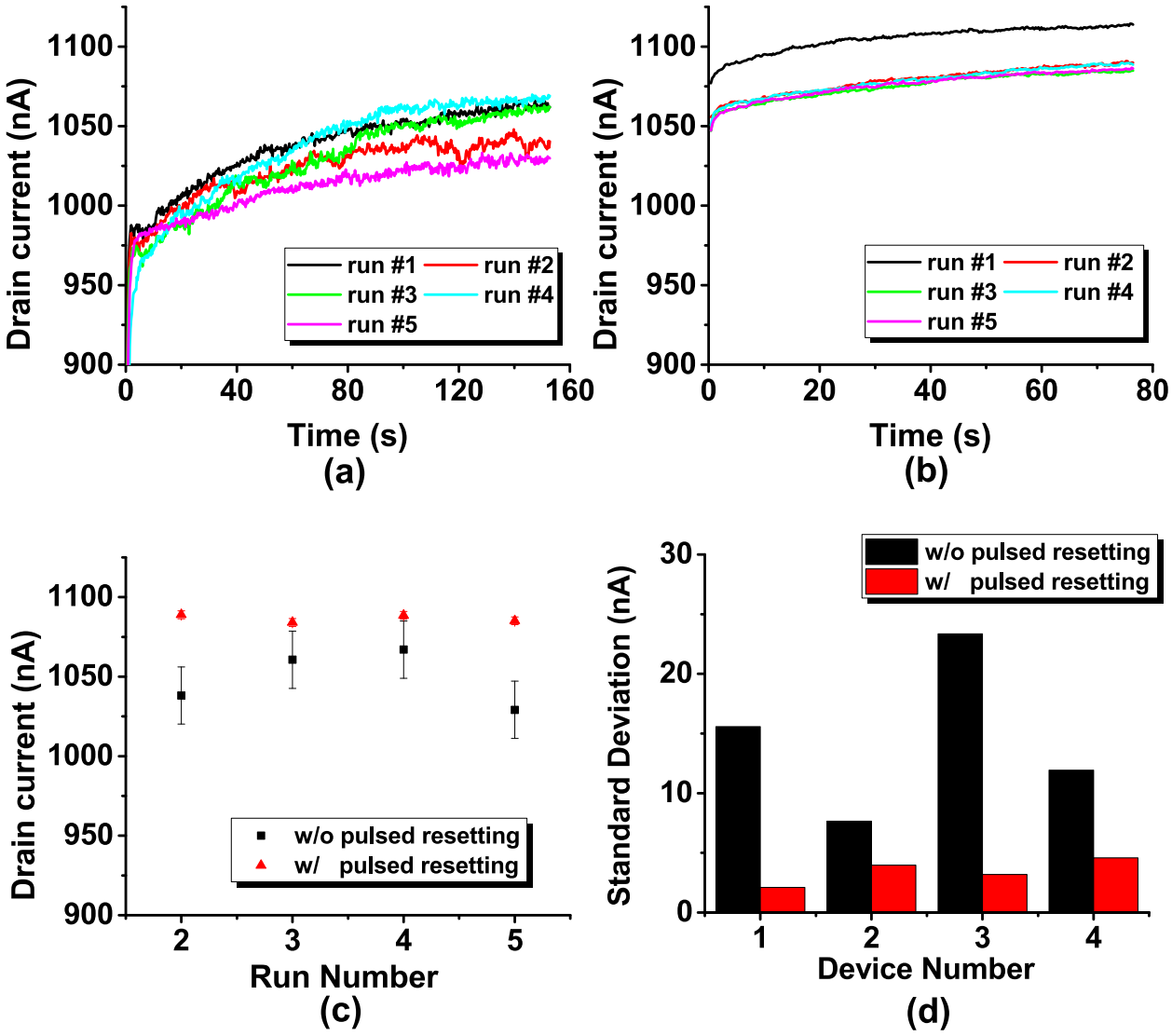

Figure 3.23: Experiment validation of the pulse resetting: Measured time-domain FET drain current in multiple runs (a) without and (b) with the pulse resetting using the same device. The measured transients became more repeatable with the pulse resetting. (c) Baseline signal calculated from traces of the time-domain data from the second run. They were obtained by averaging the drain current measured in the last 10 s of each run. The plotted error bars were standard deviations of these averaged signals among different runs, which represented the run-to-run variation. (d) Standard deviations evaluated among four devices showing the pulse resetting consistently reducing the run-to-run variation in multiple measurements.

CHAPTER 4

On Nonlinearity in FET based Ligand Binding Assay Response

4.1 Overview

Binding assays measure interactions between two molecules and are essential for biological and pharmaceutical studies [127]. A common strategy is to mix different concentrations of one soluble reactant (target analyte, T) with another (receptor probe, P) and measure the resultant complex (TP) in equilibrium using different sensing methodologies such as radio-isotopic labels [128], enzymatic chemical reactions [129], fluorescence [130], and surface plasmon resonance [131]. The affinity properties of the analyte-receptor pair are then extracted from the measured dose-response curve. A field-effect transistor (FET) is a novel class of biosensors when coupled with receptor probes on its gate terminal without an electrode. FET-based biosensors have demonstrated high sensitivity in quantifying proteins [15, 22, 132], nucleotides [133, 134], and small molecules [135]. One convenient assumption in conventional labeled binding assays is that the sensor response is linearly proportional to the quantity of bound labeled targets. However, its validity for FET-based assay is unclear as such assay detects the intrinsic charge of biomolecules, and its sensitivity may vary. Theoretical analyses suggested an intricate relation between FET sensor response and bound charge [39, 51, 136, 137]. Meanwhile, many FET-based binding assays assuming a linear transduction relation reported seemingly good results [46, 138, 139]. We need a better understanding of the nonlinearity in FET-based binding assay to explain this puzzling

phenomenon.

We here investigate the influence of nonlinear transduction mechanisms on the measured FET-based binding assay response. We find that its significance depends on both the absolute charge associated with the target analytes and its ratio to the receptor charges. We analyze the dose-response curves behavior, assuming that the sensor operates in the nonlinear screening regime. Our analysis further corroborated with published experimental data shows that the nonlinear transduction mechanism of FET sensors does play an important role in the measured results.

4.2 Theoretical Analysis

The response of a FET-based binding assay is determined by the analyte-receptor reaction and its signal transduction. Following the Langmuir–Freundlich isotherm [39], we can quantify the binding reaction with the fractional occupation of receptors Θ as

$$\Theta(c_T) = \frac{(c_T/K_D)^h}{1 + (c_T/K_D)^h}, \tag{4.1}$$

where c_T is the analyte concentration, K_D is the equilibrium dissociation constant, and h is the Hill coefficient describing the surface heterogeneity: the receptor binding activity being enhanced (suppressed) by the formed complex, which is reflected with an h larger (smaller) than one. It becomes the Langmuir isotherm with $h = 1$, which assumes that the activity of each receptor is independent. It is worth noting that both K_D and h are constant for a specific receptor-analyte pair.

We consider the flatband voltage changes ΔV_{FB} of the sensing gate as the FET response, which is well-defined for analytical calculations and also closely follows the measurable threshold voltages change ΔV_T. We consider an electrolyte-insulator interface with receptors immobilized at the dielectric surface. Two mean-field models, the charge-plane (CP) model [51, 136, 137] and the membrane model [39, 136, 137], have been developed to calculate the FET sensor response as illustrated in Fig. 4.1.

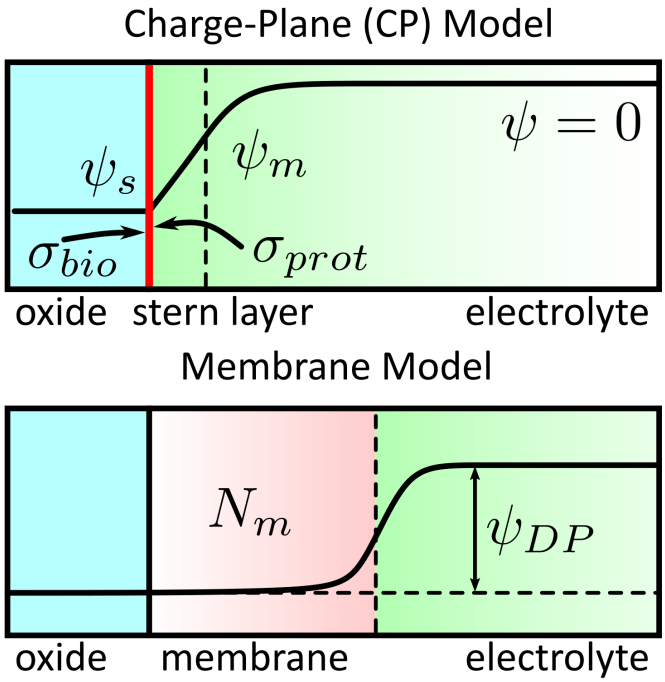

Figure 4.1: Schematics of mean-field models describing the oxide-electrolyte interface.

In the CP model, the surface electrostatic potential change $\Delta\psi_s$ is calculated with different surface charge induced by the biomolecules σ_{bio} along with other charges: titratable surface groups equilibrated with local hydrogen ions forming σ_{prot} and ions stored in electrical double layer (EDL) close to the interface represented by σ_{dl}. In calculating V_{FB}, we assume that an electric field in the oxide is zero and, from the Gauss's law, can write

$$\sigma_{bio} + \sigma_{prot} + \sigma_{dl} = 0. \tag{4.2}$$

We assume in this study an oxide surface silanized with (3-Aminopropyl)triethoxysilane, which has been widely employed in FET sensors [132]. Its protonation charge originates from the surface hydroxyl group and amine group which can be described as

$$\sigma_{prot} = \sigma_{OH} + \sigma_{NH3} \tag{4.3a}$$

$$\sigma_{OH} = q(1-p)N_s \frac{a_{H_s^+}^2 - K_1K_2}{a_{H_s^+}^2 + K_2 a_{H_s^+} + K_1K_2} \tag{4.3b}$$

$$\sigma_{NH3} = qpN_s \frac{a_{H_s^+}}{K_3 + a_{H_s^+}}, \tag{4.3c}$$

where N_s is the total hydroxyl site density of a pristine oxide surface, p is the fraction of hydroxyl groups replaced by the amine group during silanization, $a_{H_s^+}$ is the local hydrogen ion activity, and K_i denotes hydrogen dissociation coefficients [39, 140]. The local hydrogen ion activity $a_{H_s^+}$ is further related to the surface potential ψ_s and bulk hydrogen activity $a_{H_B^+}$ as

$$a_{H_s^+} = a_{H_B^+} \exp \frac{-q\psi_s}{kT}. \tag{4.4}$$

The screening charge σ_{dl} is described by the Gouy-Chapman-Stern model

$$\sigma_{dl} = \sqrt{8kT\epsilon_w n_0} \sinh\left(\frac{q\psi_m}{2kT}\right), \tag{4.5}$$

where ψ_m is the potential at the outer Helmholtz plane and n_0 is bulk electrolyte ion concentration. The surface potential ψ_s could be numerically solved from Eqs. (4.2)-(4.5).

In the membrane model, the signal arises from the dipole built-in potential change between the membrane and electrolyte as illustrated in Fig. 4.1(b). When the membrane is thick enough that the electric field does not reach the oxide, one can use the Donann potential [137] to track ΔV_{FB} at different volumetric biomolecules charge densities N_m as

$$\psi_{DP} = \frac{kT}{q} arcsinh \frac{N_m}{2n_0}, \tag{4.6}$$

where n_0 is the bulk electrolyte ion concentration.

Since there still lacks a universal preference on two models and the significance of titratable surface groups in FET biosensor response, we evaluated ΔV_{FB} using the CP model with both high [137] (5×10^{14} cm^{-2}) and negligible (5×10^{10} cm^{-2}) hydroxyl groups, as well as using the membrane model. We assume that the sensor is operated in a 0.01x diluted phosphate buffer saline having a pH of 7.4 and n_0 of 1.37 mM. In the assumed condition, surface residue groups (de)protonation induces a negative σ_{prot}, and ΔV_{FB} will depend on the polarities with a high N_s. We need to calculate ΔV_{FB} with positive and negative σ_{bio} separately. We also assume a membrane thickness of 10 nm in the membrane model calculation in plotting its result with the CP model.

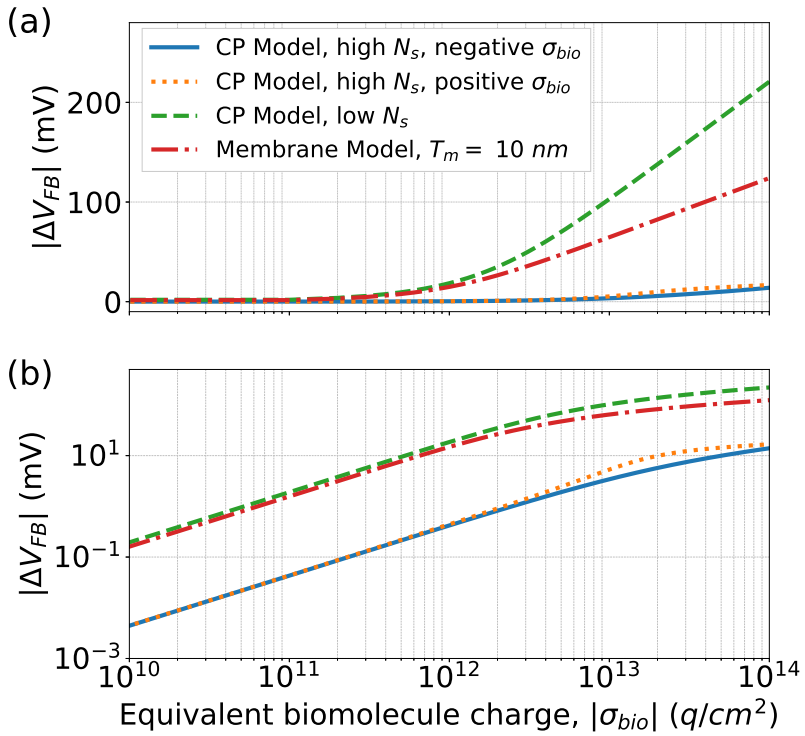

Figure 4.2: Flatband voltage change (ΔV_{FB}) vs equivalent biomolecule charge density (σ_{bio}) plotted in (a) log-linear and (b) log-log scales calculated with labeled models and conditions in the legend.

Figure 4.2 plots the calculated FET flatband voltage response ΔV_{FB} vs σ_{bio} in log-linear and log-log scales. We observe a logarithmic dependence once σ_{bio} exceeds a critical value [Fig. 4.2(a)], which is referred to as a nonlinear screening regime. A linear dependence is expected at the low σ_{bio} due to the small perturbation [Fig. 4.2(b)]. The logarithmic dependence arises from the nonlinear counter ions screening in EDL and has been reported as a screening-limited response [51].

We then study how such nonlinearity affects FET-based binding assay dose-response curves, assuming that the sensor is operated in the nonlinear screening regime. We may write

$$\Delta V_{FB} = S_\sigma \ln(\sigma_{bio}), \tag{4.7}$$

where S_σ is a model-dependent logarithmic charge sensitivity. We divide σ_{bio} into those associated with analyte binding σ_{ana} and receptor probes σ_{prob}, write $\sigma_{bio} = \sigma_{prob}(1 + \beta\Theta)$, where β is defined as the ratio of σ_{bio} when receptors are fully occupied to when they are empty, and derive the normalized response $\overline{\Delta V_{FB}}$ as a function of Θ:

$$\overline{\Delta V_{FB}}(\Theta) = \frac{1}{\ln(1+\beta)} \ln(1 + \beta\Theta). \tag{4.8}$$

We notice that the charge sensitivity S_σ is no longer present in Eq. (4.8) as being canceled out during the normalization. Equation (4.8) reduces to Θ when $\beta \ll 1$, which suggests that FET binding assay could still faithfully register the surface reaction in the nonlinear screening regime as long as the charge density induced by the analyte binding being much smaller than initial charge density associated with receptors.

4.3 Results and Discussion

4.3.1 Apparent FET sensor Calibration Curve

We plot the normalized responses calculated with different h in its linear screening regime in Fig. 4.3(a) and with $h = 1$ and different β in the nonlinear screening regime along with a linear response result with $h = 1$ in Fig. 4.3(b). Two sets of response curves closely resemble each other: both possess a sigmoid shape and an apparent logarithmic concentration dependence about the sensitive c_T range. Within the linear screening regime, the logarithmic concentration dependence comes from the symmetry of the surface coverage in Eq. (4.1), i.e.,

$$\Theta(c_T/K_D) = 1 - \Theta(K_D/c_T). \tag{4.9}$$

While both features have been routinely reported in FET sensing experimental data, these similarities lead to ambiguity in interpreting measurement results and recognizing the significance of FET nonlinear transduction mechanisms. Neither can the observed sigmoid-shape response justify the linear transduction assumption, nor can the logarithmic concentration

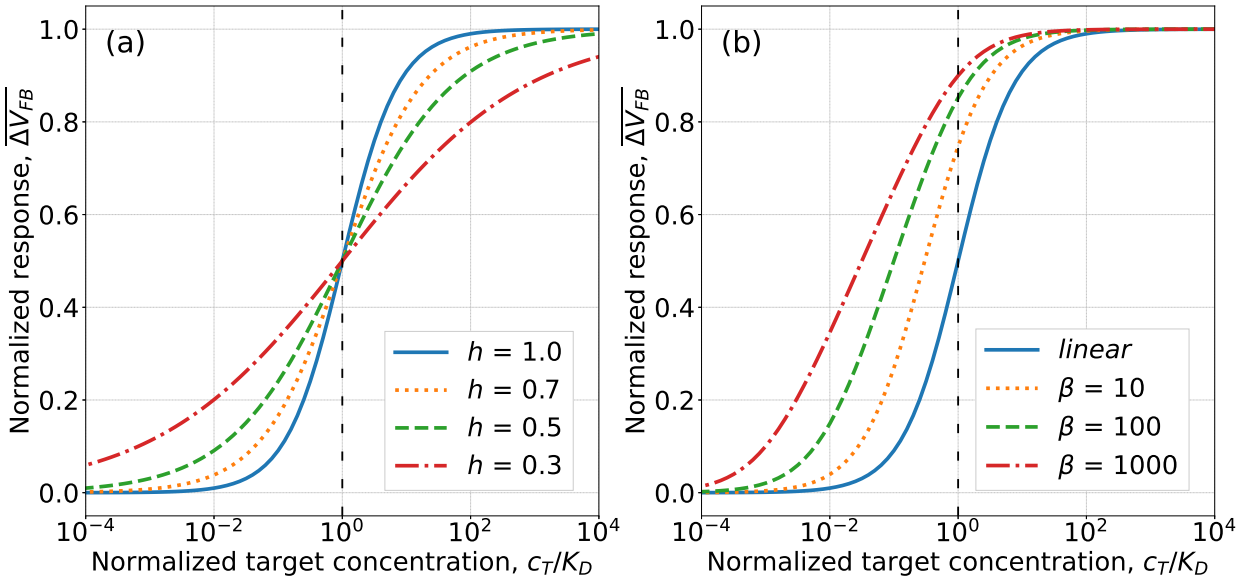

Figure 4.3: Normalized FET flatband voltage response assuming that the sensor is operated (a) in the linear screening regime with different Hill parameter h and (b) in the nonlinear screening regime with different β and $h = 1$. The dashed vertical line marks $c_T/K_D = 1$.

dependence prove the sensor to operate in its screening-limited regime.

We summarize in Table 4.1 the apparent characteristics of two sigmoid-shaped curves. The slope of the normalized response in the linear regime is purely determined by the surface heterogeneity [39], and an increased heterogeneity (smaller h) leads to a more flattened curve and larger dynamic range. The same could also arise from the nonlinearity of the FET sensor, as shown in Fig. 4.3(b) where h equals 1 in all curves. More importantly, the assay response with the linear screening regime always has its half-maximal response concentration and maximum slope both at $c_T = K_D$ regardless of h, which makes it a convenient practice to read the equilibrium dissociation constant K_D at this point in binding assay results. However, the curve may start rolling off closer to $c_T = K_D$ due to the nonlinear screening in FET sensors. At large β, the maximum slope also coincides with the half-maximal response at the concentration roughly $1/2h \times \log_{10}(1 + \beta)$ orders of magnitude lower than K_D.

Two response curves closely resemble each other especially when the true affinity parame-

Table 4.1: Apparent dose-response curve characteristics with linear and logarithmic (non-linear) FET transduction relation.

	linear	logarithmic
maximum slope	$\frac{\ln(10)}{4}h$	$\frac{h}{\log_{10}(1+\beta)}\frac{\beta}{(1+\sqrt{1+\beta})^2}$
c_T with $\overline{\Delta V_{FB}} = 0.5$	K_D	$(\frac{1}{\sqrt{1+\beta}})^{1/h}K_D$
slope at $c_T = K_D$	$\frac{\ln(10)}{4}h$	$\frac{h}{4\log_{10}(1+\beta)}\frac{\beta}{1+\beta/2}$

ters like K_D and h are not known, which unfortunately happens in most reported experiment data. Nakatsuka [44] and Cheung [45] *et al.* recently reported aptamer-FET sensors using receptor probes whose K_D was well characterized with fluorescence assays. Device threshold voltage change was over wide range target concentrations and complete response was registered. Fig. 4.4 shows the normalized FET response to various biomolecules, which clearly resemble more to nonlinear model prediction in Fig. 4.3(b). They rolled off close to K_D and the maximum slope appeared orders of magnitudes below K_D. Such corroboration of experiment data obtained with multiple analyte-receptor pairs having K_D from 100 nM to 10 μM provides strong evidence that the screen-limited nonlinearity in FET based immunosensors does play an important role in shaping their calibration curve. The logarithmic relation shifts the apparent sensitive range from K_D to lower range giving them advantages to quantify low concentration samples. Besides, its dynamic range and could also be extended by boosting β in addition to increasing the surface heterogeneity [39]. This could be achieved by minimizing the charge near the sensing surface when only receptor probes are presented.

The key to identifying the above differences is an a priori knowledge of genuine surface reaction K_D and h. Nakatsuka *et al.* and Cheung *et al.* recently reported FET sensors with synthesized aptamer receptor probes whose K_D was characterized with fluorescence

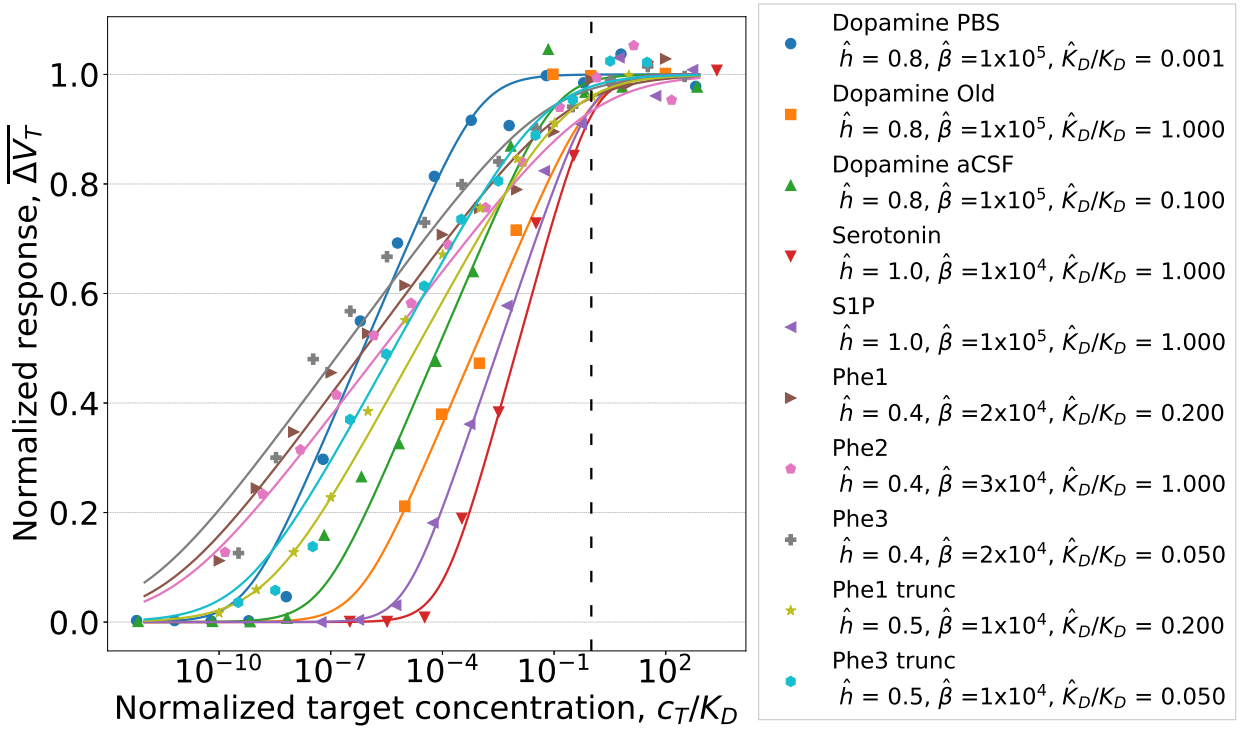

Figure 4.4: Normalized FET-based binding assay dose-response curves extracted from Refs. 20 and 21. Fitted parameters are listed in the legend. The dashed vertical line marks $c_T/K_D = 1$.

assays [44, 45]. Device threshold voltage change was measured over a wide range of target analyte concentrations in high conductivity buffers, including undiluted phosphate buffers (PBS) and artificial cerebrospinal fluid (aCSF). The employed aptamers are highly charged oligonucleotides consisting of about 70 bases, which could possibly induce σ_{bio} on the order of 10^{14} q/cm^2 and drive the FET sensor well into the nonlinear screening regime. In capturing/releasing the target analytes, aptamers undergo a conformation change that moves the highly charged phosphate backbones closer or further to the sensing surface that could effectively modulate σ_{bio} with a large β as charges away from the surface being quickly screened out in high conductivity buffers. Figure 4.4 shows the normalized FET ΔV_T from their reports with different analyte-receptor pairs. It clearly resembles more to nonlinear prediction in Fig. 4.3(b): They roll off close to K_D, and have the maximum slope appeared

orders of magnitudes below K_D. Such corroboration of experimental data provides convincing evidence that the nonlinearity of FET sensors does play an important role in shaping its ultimate dose-response curves. The screening-limited transduction relation shifts the sensitive range to lower concentrations and helps to expand the assay dynamic range. Interpreting FET bind assay data without the awareness of the sensor nonlinearity is prone to underestimate K_D and h.

4.3.2 Estimating critical charge density

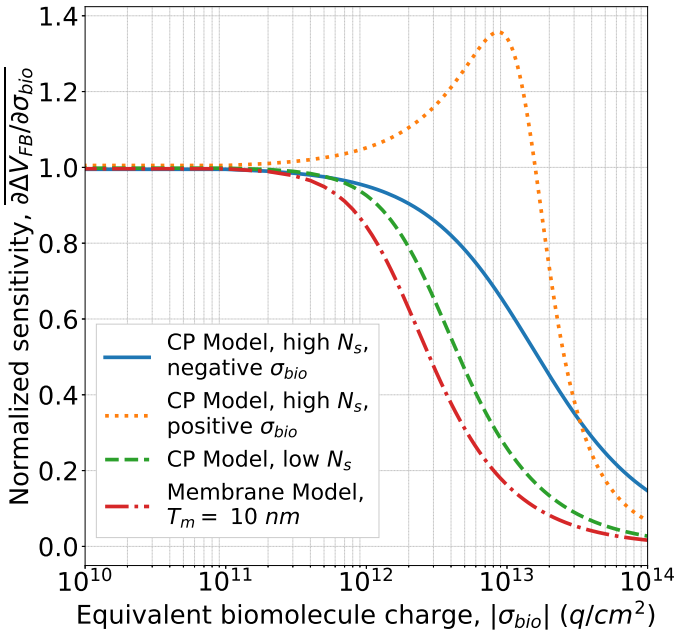

Figure 4.5: Normalized charge sensitivity vs surface charge density with the labeled models.

To gain practical insight on the difference in the chosen models, we estimate critical surface charge densities dividing the linear and nonlinear screening regimes with the above-mentioned conditions. We plot in Fig. 4.5 the charge sensitivity ($\partial \Delta V_{FB}/\partial \sigma_{bio}$) normalized with its value at infinitesimally small σ_{bio}, which stays a constant in the linear screening

regime. Our calculations suggest the nonlinear screening appears with a moderate σ_{bio} of $\sim 10^{12}$ q/cm^2 ,which corresponds to fully packed proteins having the size of 10 nm and 1 q charge. Moreover, the linear screening range is expanded with higher N_s as titratable surface groups act as an additional buffering mechanism and temper the nonlinear EDL screening. When they have the opposite charge as σ_{bio}, the charge sensitivity peaks when σ_{bio} completely compensates σ_{prot} as shown in Fig. 4.5. This could be intuitively understood as the screening from counter ions in EDL is weakest with a net neutral sensing interface where $\sigma_{dl} = 0$, leading to a maximal FET charge sensitivity [40].

4.4 Summary

In summary, we have studied the nonlinearity in FET-based binding assay response. We have found that the nonlinear transduction relation may distort its dose-response curves, leading to (1) its high sensitivity range and the half-maximal response concentration shifted toward lower concentrations, and (2) an expanded dynamic range. Our results raise the awareness of the nonlinear transduction mechanism in designing FET-based binding assay and interpreting its measurement results.

CHAPTER 5

Conclusions

5.1 Summary

In this dissertation, we have examined three nonideal factors affecting the measurement uncertainties in FET-based biological sensors: noise, instability and, nonlinearity.

1. In Chapter 2, we have examined the low-frequency noise characteristics of dual-gated-FET biosensors with Schottky contacts. We identified its optimal biasing strategy and found the flicker noise arising from traps with a nonuniform energy distribution at the sensing front gate to be the major noise source. We have found dual-gated FET biosensors are advantageous over their single-gated counterparts on noise immunity when traps at the sensing interface having nonuniform energy distribution: dual-gated FET biosenosrs could avoid biasing the trappy front interface towards band edge as a mean to provide sufficient signal gain. They therefore can offer a larger signal gain at its optimal bias for noise performance.

2. In Chapter 3, we have investigated the instability behaviors in the same dual-gated silicon FET biochemical sensor. We found the dominant instability source associated with the back-gate biasing change and hypothesized it resulted from the charge re-distribution inside the back oxide. We explored alternating biasing strategies using pulses with dual-gated devices other than a constant voltage to alleviate effects of their instability. We showed that a pulsed IV measurement scheme, which uses a pulse train having short pulse width and a small duty cycle to bias the back-gate terminal,

significantly reduced the output current signal drifting in the studied devices. We also proposed a novel pulse resetting measurement scheme. A pulse train voltage back-gate biasing sequence was applied before a normal measurement. It led to more repeatable transient behaviors and reduced run-to-run variations, and, therefore, mitigated the repeatability issue caused by the device instability.

3. In Chapter 4, we have studied the nonlinearity in FET-based binding assay response. We found that the nonlinear transduction relation may distort its dose-response curves, leading to its high sensitivity range and the half-maximal response concentration shifted toward lower concentrations and an expanded dynamic range. Corroborated with experiment data, we have found that the signal transduction of FET sensors plays an important role in shaping their dose-response curves. Negligence of such nonlinearity would introduce errors in the extracted affinity properties of the analyte-receptor pair.

5.2 Contributions of this work

Measurement uncertainties directly determine the Lower Limit of Detection in a bioanalytical assay. Understanding and minimizing measurement uncertainties is a critical task in developing FET-based biosensors. FETs have emerged as an intriguing transducer in biological sensing systems which have been demonstrated to have promising sensitivities against a wide range of clinically relevant targets. However, a good understanding of nonideal factors that may produce measurement uncertainties in such transducers is still lagging, becoming a hurdle in achieving a lower LLOD and developing them into reliable bioanalytical assays. This dissertation has contributed to advancing the understanding of measurement uncertainties in FET-based biosensors and developing techniques to mitigate them.

In chapter 2, we examined the low-frequency noise characteristics of Schottky contacted dual-gated silicon FET biosensors. Dual-gated FET biosensors have been of great interest because of their ubiquitous signal amplifying capability. Their low-frequency noise perfor-

mance is an important factor to understand as it intrinsically governs the sensors' lowest detection limit. Previous noise studies of dual-gated FET biosensors have often overlooked the possible energy distribution of the interface trap density states and assumed simple uniform distribution. Such assumption may not be reasonable for FET biosensors which are operated inside the electrolyte and have a more versatile biasing scheme compared with transistors used in conventional analog circuits. Our noise measurement data analysis has suggested a nonuniform trap energy distribution at the sensing gate. In such systems, we showed that dual-gated FET-based biosensors have advantages over their single-gated counterparts. One could bias the trappy sensing interface at the middle of the bandgap where the trap density is low and maintain a considerable signal gain with carriers at the other interface. Our results provided insights on how to use a multi-gate structure to achieve a high signal gain and high signal-to-noise ratio at the same time. In addition, we also showed that the noise contribution from employed Schottky contacts to be minimal around the optimum bias regime for the lowest detection limit.

In chapter 3, we analyzed the instability behaviors of our dual-gated FET biochemical sensor and hypothesized that it was a result of charge redistribution inside the back-gate dielectric layer under the varying electric field. We have proposed and demonstrated two novel measurement schemes, pulsed IV and pulse resetting, in mitigating their effects. Our results provided strategies to work with FET biosensors that are inherently subjected to drifting and repeatability issues. Instability behaviors have been commonly observed in FET biosensors due to their salty aqueous working environment. Some instability sources like the dielectric instability are inherently associated with the sensor itself and challenging to be completely eliminated. Our work showed that their effects could be counteracted with smart biasing strategies. We have shown that the device current drifting was significantly reduced by driving its gate with pulses having a small duty cycle in the pulsed IV measurement. We also demonstrated that the same current transient could be repeatably obtained with the pulse resetting, which reduced the run-to-run variations and, therefore, its measurement uncer-

tainties when the sensor need to be measured multiple times. Previous instability studies have focused primarily on reducing the current drifting in a continuous measurement, and few have addressed the repeatability problem, which is more critical in developing analytical assays in the authors' view.

In chapter 4, we examined the nonlinear screening in FET-based sensors and its impacts on their measured results. We showed that the nonlinear transduction mechanism of FET sensors has an important role in forming the dose-response curves. FET-based biosensors have been well known for their label-free detection capability to detect the intrinsic charge from the analytes other than signal generating tags. One potential pitfall is that its signal may not be linearly proportional to the captured biomolecules amount. The role of transduction nonlinearity has been ambiguous and puzzling for a long time. Our analyses corroborated with experimental data provide convincing evidence for the role of nonlinear signal transduction in FET-based biosensors. Besides, our results raised awareness of the impact of sensors in FET-based sensing results, especially in interpreting its bio-affinity attributes. Many FET-sensing experiments have reported that employed biomolecule receptor probes have improved bio-affinity towards targets when immobilized on a FET sensor surface, which is hard to understand. Receptors in the solid phase are generally expected to have more degraded bio-affinity than in the solution phase. Some binding sites become inaccessible and blocked. Our results showed a physically feasible explanation: the apparent higher affinity could result from distortion of the underlying FET sensor.

5.3 Recommendations for future work

To build upon the work performed in this dissertation, we recommend further research in the following subjects:

1. Developing novel FET measurement schemes, including new biasing strategies and sensing front-ends. FET biosensors have been primarily measured as individual de-

vices with conventional methods, for example, measuring the drain current change with constant voltage biasing or its transfer characteristics shifts. Commonly used output signals are the measured drain current change, extracted threshold voltage change, normalized current change, etc. Though these strategies fit well in investigating the detection principles, they may not be the optimal choice in a bioanalytical assay. We have shown in this dissertation that employing a periodic alternating pulsed biasing could suppress the drifting, and using a pulse resetting could reduce run-to-run variation caused by the inherent instability sources. Likewise, other biasing strategies shall be explored to improve both the sensor's sensitivities and stabilities. Besides, incorporating FET into a sensing front-end circuit block could further benefit its performance than using them as individual transistors. One convenient example is that using ISFETs in a differential pair rejected drifting from an external reference electrode. Another is to use the FET sensor in a ring oscillator to convey the drain current signal to oscillation frequencies. Knowledge from circuit design shall be incorporated in building novel FET biosensing front-ends. A potentially valuable subject could be introducing feedback into the transducer to counteract the device instability with possibly sacrificing its signal gain.

2. Developing an automated sample-in-answer-out FET-based sensing system. This dissertation addressed the measurement uncertainties at the device level. System-level nonideal factors may introduce additional measurement uncertainties in an analytical assay, including device-to-device variation, batch-to-batch variation in sensor surface treatment, sensor storage, sample pre-processing, etc. A complete sample-in-answer-out sensing system is necessary to evaluate these factors and minimize their impacts systematically. The sensing system should be able to follow a pre-determined protocol to complete the sample transfer, pre-processing, sensor calibration, data acquisition, and data processing automatically to minimize the influences from the assay operator. The ultimate measurement uncertainties should also be evaluated with the real clinic

samples.

3. Numerical modeling of the biomolecule-induced signal at the electrolyte-dielectric interface. It is critical to have an accurate quantitative model describing the voltage signal induced by the bonded biomolecules to optimize the surface biochemistry in FET-based biosensors. Existing theories often treat biomolecules as a homogenized layer over the sensing interface. Despite tremendous insights they have been provided in developing FET biosensors, such models lack the following two features, which the author would see to improve in the future. First, they do not include any information on biomolecules' chemical structures, charge distribution, and orientations. Such information have been accumulated with the rapid development of the spectroscopy capabilities and molecular dynamic simulations, and a predictive model incorporating these information would greatly facilitate designing design and optimizing the surface biochemistry of the FET biosensor. Second, existing models lack abilities to describe the dynamics of the bonded molecules under an alternating electric field, which is essential in designing the FET biosensors with a time-varying bias.

REFERENCES

[1] J. Tamaoka and K. Komagata, "Determination of DNA base composition by reversed-phase high-performance liquid chromatography," *FEMS Microbiology Letters*, vol. 25, no. 1, pp. 125–128, 1984.

[2] B. Johnsson, S. Löfås, and G. Lindquist, "Immobilization of proteins to a carboxymethyldextran-modified gold surface for biospecific interaction analysis in surface plasmon resonance sensors," *Analytical Biochemistry*, vol. 198, no. 2, pp. 268–277, 1991.

[3] Y. Tang, X. Zeng, and J. Liang, "Surface plasmon resonance: an introduction to a surface spectroscopy technique," *Journal of Chemical Education*, vol. 87, no. 7, pp. 742–746, 2010.

[4] C. A. Heid, J. Stevens, K. J. Livak, and P. M. Williams, "Real time quantitative PCR," *Genome Research*, vol. 6, no. 10, pp. 986–994, 1996.

[5] A. Warsinke, A. Benkert, and F. W. Scheller, "Electrochemical immunoassays," *Fresenius' Journal of Analytical Chemistry*, vol. 366, no. 6-7, pp. 622–634, 2000.

[6] M. Kronick and P. D. Grossman, "Immunoassay techniques with fluorescent phycobiliprotein conjugates," *Clinical Chemistry*, vol. 29, no. 9, pp. 1582–1586, 1983.

[7] R. M. Lequin, "Enzyme immunoassay (EIA)/enzyme-linked immunosorbent assay (ELISA)," *Clinical Chemistry*, vol. 51, no. 12, pp. 2415–2418, 2005.

[8] V. C. Romao, S. A. Martins, J. Germano, F. A. Cardoso, S. Cardoso, and P. P. Freitas, "Lab-on-chip devices: gaining ground losing size," *ACS Nano*, vol. 11, no. 11, pp. 10659–10664, 2017.

[9] P. Bergveld, R. Van Hal, and J. C. Eijkel, "The remarkable similarity between the acid-base properties of ISFETs and proteins and the consequences for the design of ISFET biosensors," *Biosensors and Bioelectronics*, vol. 10, no. 5, pp. 405–414, 1995.

[10] N. Clément, K. Nishiguchi, J. Dufreche, D. Guerin, A. Fujiwara, and D. Vuillaume, "A silicon nanowire ion-sensitive field-effect transistor with elementary charge sensitivity," *Applied Physics Letters*, vol. 98, no. 1, p. 014104, 2011.

[11] P. Bergveld, "Development, operation, and application of the ion-sensitive field-effect transistor as a tool for electrophysiology," *IEEE Transactions on Biomedical Engineering*, vol. BME-19, no. 5, pp. 342–351, 1972.

[12] J. Schenck, *Technical difficulties remaining to the application of ISFET devices.* CRC Press Inc, 1978.

[13] M. Gotoh, M. Suzuki, I. Kubo, E. Tamiya, and I. Karube, "Immuno-FET sensor," *Journal of Molecular Catalysis*, vol. 53, no. 3, pp. 285–292, 1989.

[14] R. Schasfoort, P. Bergveld, R. Kooyman, and J. Greve, "Possibilities and limitations of direct detection of protein charges by means of an immunological field-effect transistor," *Analytica Chimica Acta*, vol. 238, p. 323–329, 1990.

[15] Y. Cui, Q. Wei, H. Park, and C. M. Lieber, "Nanowire nanosensors for highly sensitive and selective detection of biological and chemical species," *Science*, vol. 293, no. 5533, pp. 1289–1292, 2001.

[16] X. P. Gao, G. Zheng, and C. M. Lieber, "Subthreshold regime has the optimal sensitivity for nanowire FET biosensors," *Nano Letters*, vol. 10, no. 2, pp. 547–552, 2010.

[17] K. Shoorideh and C. O. Chui, "On the origin of enhanced sensitivity in nanoscale fet-based biosensors," *Proceedings of the National Academy of Sciences*, vol. 111, no. 14, pp. 5111–5116, 2014.

[18] J.-i. Hahm and C. M. Lieber, "Direct ultrasensitive electrical detection of DNA and DNA sequence variations using nanowire nanosensors," *Nano Letters*, vol. 4, no. 1, pp. 51–54, 2004.

[19] T. Adam and U. Hashim, "Highly sensitive silicon nanowire biosensor with novel liquid gate control for detection of specific single-stranded DNA molecules," *Biosensors and Bioelectronics*, vol. 67, pp. 656–661, 2015.

[20] F. Patolsky, G. Zheng, O. Hayden, M. Lakadamyali, X. Zhuang, and C. M. Lieber, "Electrical detection of single viruses," *Proceedings of the National Academy of Sciences*, vol. 101, no. 39, pp. 14017–14022, 2004.

[21] G.-J. Zhang, L. Zhang, M. J. Huang, Z. H. H. Luo, G. K. I. Tay, E.-J. A. Lim, T. G. Kang, and Y. Chen, "Silicon nanowire biosensor for highly sensitive and rapid detection of Dengue virus," *Sensors and Actuators B: Chemical*, vol. 146, no. 1, pp. 138–144, 2010.

[22] E. Stern, J. F. Klemic, D. A. Routenberg, P. N. Wyrembak, D. B. Turner-Evans, A. D. Hamilton, D. A. LaVan, T. M. Fahmy, and M. A. Reed, "Label-free Immunodetection with CMOS-compatible Semiconducting Nanowires," *Nature*, vol. 445, no. 7127, p. 519, 2007.

[23] K. Kim, C. Park, D. Kwon, D. Kim, M. Meyyappan, S. Jeon, and J.-S. Lee, "Silicon nanowire biosensors for detection of cardiac troponin I (cTnI) with high sensitivity," *Biosensors and Bioelectronics*, vol. 77, pp. 695–701, 2016.

[24] Y. Mao, K.-S. Shin, X. Wang, Z. Ji, H. Meng, and C. O. Chui, "Semiconductor electronic label-free assay for predictive toxicology," *Scientific Reports*, vol. 6, p. 24982, Apr. 2016. doi:10.1038/srep24982.

[25] N. Elfstroem, A. E. Karlstroem, and J. Linnros, "Silicon nanoribbons for electrical detection of biomolecules," *Nano letters*, vol. 8, p. 945–949, Mar 2008.

[26] L. Mu, I. A. Droujinine, K. Rajan, Nitin, S. D. Sawtelle, and M. A. Reed, "Direct, rapid, and label-free detection of enzyme–substrate interactions in physiological buffers using cmos-compatible nanoribbon sensors," *Nano Letters*, vol. 14, p. 5315–5322, Sep 2014.

[27] M. Kamahori, Y. Ishige, and M. Shimoda, "A novel enzyme immunoassay based on potentiometric measurement of molecular adsorption events by an extended-gate field-effect transistor sensor," *Biosensors and Bioelectronics*, vol. 22, p. 3080–3085, Jun 2007.

[28] J. Zhang, M. Rupakula, F. Bellando, E. G. Cordero, J. Longo, F. Wildhaber, G. Herment, H. Guérin, and A. M. Ionescu, "Sweat biomarker sensor incorporating picowatt, three-dimensional extended metal gate ion sensitive field effect transistors," *ACS Sensors*, vol. 4, no. 8, p. 2039–2047, 2019.

[29] S. Pud, J. Li, V. Sibiliev, M. Petrychuk, V. Kovalenko, A. Offenhausser, and S. Vitusevich, "Liquid and back gate coupling effect: toward biosensing with lowest detection limit," *Nano Letters*, vol. 14, no. 2, pp. 578–584, 2014.

[30] L. Capua, Y. Sprunger, H. Elettro, F. Risch, A. Grammoustianou, R. Midahuen, T. Ernst, S. Barraud, R. Gill, and A. M. Ionescu, "Label-free c-reactive protein si nanowire fet sensor arrays with super-nernstian back-gate operation," *IEEE Transactions on Electron Devices*, vol. PP, no. 99, p. 1–7, 2022.

[31] P. K. Ang, W. Chen, A. T. S. Wee, and K. P. Loh, "Solution-gated epitaxial graphene as ph sensor," *Journal of the American Chemical Society*, vol. 130, p. 14392–14393, Nov 2008.

[32] N. Gao, T. Gao, X. Yang, X. Dai, W. Zhou, A. Zhang, and C. M. Lieber, "Specific detection of biomolecules in physiological solutions using graphene transistor biosensors," *Proceedings of the National Academy of Sciences*, vol. 113, p. 14633–14638, Dec 2016.

[33] A. Ganguli, V. Faramarzi, A. Mostafa, M. T. Hwang, S. You, and R. Bashir, "High sensitivity graphene field effect transistor-based detection of dna amplification," *Advanced Functional Materials*, vol. 30, p. 2001031, May 2020.

[34] R. Narang, M. Saxena, R. S. Gupta, and M. Gupta, "Dielectric modulated tunnel field-effect transistor—a biomolecule sensor," *IEEE Electron Device Letters*, vol. 33, no. 2, p. 266–268, 2012.

[35] A. Gao, N. Lu, Y. Wang, and T. Li, "Robust ultrasensitive tunneling-fet biosensor for point-of-care diagnostics," *Scientific Reports*, vol. 6, p. 22554, Mar 2016.

[36] F. Bellando, C. K. Dabhi, A. Saeidi, C. Gastaldi, Y. S. Chauhan, and A. M. Ionescu, "Subthermionic negative capacitance ion sensitive field-effect transistor," *Applied Physics Letters*, vol. 116, p. 173503, Apr 2020.

[37] G. Zheng, F. Patolsky, Y. Cui, W. U. Wang, and C. M. Lieber, "Multiplexed electrical detection of cancer markers with nanowire sensor arrays," *Nature Biotechnology*, vol. 23, p. 1294–1301, Oct 2005.

[38] A. D. McNaught, A. Wilkinson, *et al.*, *Compendium of chemical terminology*, vol. 1669. Blackwell Science Oxford, 1997.

[39] Y. Liu and R. W. Dutton, "Effects of charge screening and surface properties on signal transduction in field effect nanowire biosensors," *Journal of Applied Physics*, vol. 106, no. 1, p. 014701, 2009.

[40] K. Shoorideh and C. O. Chui, "Optimization of the sensitivity of fet-based biosensors via biasing and surface charge engineering," *IEEE Transactions on Electron Devices*, vol. 59, no. 11, pp. 3104–3110, 2012.

[41] R. Elnathan, M. Kwiat, A. Pevzner, Y. Engel, L. Burstein, A. Khatchtourints, A. Lichtenstein, R. Kantaev, and F. Patolsky, "Biorecognition layer engineering: overcoming screening limitations of nanowire-based FET devices," *Nano Letters*, vol. 12, no. 10, pp. 5245–5254, 2012.

[42] N. Gao, W. Zhou, X. Jiang, G. Hong, T.-M. Fu, and C. M. Lieber, "General strategy for biodetection in high ionic strength solutions using transistor-based nanoelectronic sensors," *Nano Letters*, vol. 15, no. 3, pp. 2143–2148, 2015.

[43] L. Mu, I. A. Droujinine, J. Lee, M. Wipf, P. Davis, C. Adams, J. Hannant, and M. A. Reed, "Nanoelectronic platform for ultrasensitive detection of protein biomarkers in serum using DNA amplification," *Analytical Chemistry*, vol. 89, no. 21, pp. 11325–11331, 2017.

[44] N. Nakatsuka, K.-A. Yang, J. M. Abendroth, K. M. Cheung, X. Xu, H. Yang, C. Zhao, B. Zhu, Y. S. Rim, Y. Yang, *et al.*, "Aptamer-field-effect transistors overcome debye length limitations for small-molecule sensing," *Science*, vol. 362, no. 6412, pp. 319–324, 2018.

[45] K. M. Cheung, K.-A. Yang, N. Nakatsuka, C. Zhao, M. Ye, M. E. Jung, H. Yang, P. S. Weiss, M. Stojanovic, and A. M. Andrews, "Phenylalanine monitoring via aptamer-field-effect transistor sensors," *ACS Sensors*, vol. 4, no. 12, pp. 3308–3317, 2019.

[46] S. Ma, X. Li, Y.-K. Lee, and A. Zhang, "Direct label-free protein detection in high ionic strength solution and human plasma using dual-gate nanoribbon-based ion-sensitive field-effect transistor biosensor," *Biosensors and Bioelectronics*, vol. 117, pp. 276–282, 2018.

[47] M. Deen, M. Shinwari, J. Ranuárez, and D. Landheer, "Noise considerations in field-effect biosensors," *Journal of Applied Physics*, vol. 100, no. 7, p. 074703, 2006.

[48] N. K. Rajan, D. A. Routenberg, J. Chen, and M. A. Reed, "1/f noise of silicon nanowire biofets," *IEEE Electron Device Letters*, vol. 31, no. 6, pp. 615–617, 2010.

[49] N. K. Rajan, X. Duan, A. Vacic, D. A. Routenberg, and M. A. Reed, "Limits of detection for silicon nanowire BioFETs," in *70th Device Research Conference*, pp. 91–92, IEEE, 2012.

[50] E. Stern, R. Wagner, F. J. Sigworth, R. Breaker, T. M. Fahmy, and M. A. Reed, "Importance of the debye screening length on nanowire field effect transistor sensors," *Nano Letters*, vol. 7, no. 11, pp. 3405–3409, 2007.

[51] P. R. Nair and M. A. Alam, "Screening-limited response of nanobiosensors," *Nano Letters*, vol. 8, no. 5, pp. 1281–1285, 2008.

[52] Y. Mao, K.-S. Shin, X. Wang, Z. Ji, H. Meng, and C. O. Chui, "Semiconductor electronic label-free assay for predictive toxicology," *Scientific Reports*, vol. 6, p. 24982, 2016.

[53] A. Ganguli, Y. Watanabe, M. T. Hwang, J.-C. Huang, and R. Bashir, "Robust label-free microRNA detection using one million ISFET array," *Biomedical Microdevices*, vol. 20, no. 2, p. 45, 2018.

[54] W.-C. Kuo, I. Sarangadharan, A. K. Pulikkathodi, P.-H. Chen, S.-L. Wang, C.-R. Wu, and Y.-L. Wang, "Investigation of electrical stability and sensitivity of electric double layer gated field-effect transistors (FETs) for miRNA detection," *Sensors*, vol. 19, no. 7, p. 1484, 2019.

[55] P. Zang, Y. Liang, and W. W. Hu, "Improved hydrolytic stability and repeatability: pH sensing with APTES-coated silicon nanowire bio-FETs," *IEEE Nanotechnology Magazine*, vol. 9, no. 4, pp. 19–28, 2015.

[56] D. W. Kwon, R. Lee, S. Kim, H.-S. Mo, D. H. Kim, and B.-G. Park, "A novel fabrication method for co-integrating ISFET with damage-free sensing oxide and threshold voltage-tunable CMOS read-out circuits," *Sensors and Actuators B: Chemical*, vol. 260, pp. 627–634, 2018.

[57] T. Rim, K. Kim, N. Hong, W. Ko, C.-K. Baek, S. Jeon, M. J. Deen, M. Meyyappan, Y.-H. Jeong, and J.-S. Lee, "Investigation of the electrical stability of Si-nanowire biologically sensitive field-effect transistors with embedded Ag/AgCl pseudo reference electrode," *RSC Advances*, vol. 3, no. 21, pp. 7963–7969, 2013.

[58] J. Lee, M. Wipf, L. Mu, C. Adams, J. Hannant, and M. A. Reed, "Metal-coated microfluidic channels: An approach to eliminate streaming potential effects in nano biosensors," *Biosensors and Bioelectronics*, vol. 87, pp. 447–452, 2017.

[59] D. Kwon, J. H. Lee, S. Kim, R. Lee, H. Mo, J. Park, D. H. Kim, and B.-G. Park, "Drift-free pH detection with silicon nanowire field-effect transistors," *IEEE Electron Device Letters*, vol. 37, no. 5, pp. 652–655, 2016.

[60] S. Zafar, C. D'Emic, A. Jagtiani, E. Kratschmer, X. Miao, Y. Zhu, R. Mo, N. Sosa, H. Hamann, G. Shahidi, *et al.*, "Silicon nanowire field effect transistor sensors with minimal sensor-to-sensor variations and enhanced sensing characteristics," *ACS Nano*, vol. 12, no. 7, pp. 6577–6587, 2018.

[61] K. Martens, S. Santermans, M. Gupta, G. Hellings, R. Wuytens, B. Du Bois, E. Dupuy, E. Altamirano-Sanchez, K. Jans, R. Vos, T. Stakenborg, L. Lagae, M. Heyns, S. Severi, and W. V. Roy, "BioFET Technology: Aggressively Scaled pMOS FinFET as Biosensor," in *2019 IEEE International Electron Devices Meeting (IEDM)*, pp. 18–6, IEEE, 2019.

[62] J. M. Rothberg, W. Hinz, T. M. Rearick, J. Schultz, W. Mileski, M. Davey, J. H. Leamon, K. Johnson, M. J. Milgrew, M. Edwards, J. Hoon, J. F. Simons, D. Marran, J. W. Myers, J. F. Davidson, A. Branting, J. R. Nobile, B. P. Puc, D. Light, T. A. Clark, M. Huber, J. T. Branciforte, I. B. Stoner, S. E. Cawley, M. Lyons, Y. Fu, N. Homer, M. Sedova, X. Miao, B. Reed, J. Sabina, E. Feierstein, M. Schorn, M. Alanjary, E. Dimalanta, D. Dressman, R. Kasinskas, T. Sokolsky, J. A. Fidanza, E. Namsaraev, K. J. McKernan, A. Williams, G. T. Roth, and J. Bustillo, "An integrated semiconductor device enabling non-optical genome sequencing," *Nature*, vol. 475, pp. 348–352, July 2011.

[63] S. Ma, X. Li, Y.-K. Lee, and A. Zhang, "Direct label-free protein detection in high ionic strength solution and human plasma using dual-gate nanoribbon-based ion-sensitive field-effect transistor biosensor," *Biosensors and Bioelectronics*, vol. 117, pp. 276–282, Oct. 2018.

[64] Y. Zhang, J. Clausmeyer, B. Babakinejad, A. L. Córdoba, T. Ali, A. Shevchuk, Y. Takahashi, P. Novak, C. Edwards, M. Lab, S. Gopal, C. Chiappini, U. Anand, L. Magnani, R. C. Coombes, J. Gorelik, T. Matsue, W. Schuhmann, D. Klenerman, E. V. Sviderskaya, and Y. Korchev, "Spearhead nanometric field-effect transistor sensors for single-cell analysis," *ACS Nano*, vol. 10, pp. 3214–3221, Mar. 2016.

[65] I. Fakih, O. Durnan, F. Mahvash, I. Napal, A. Centeno, A. Zurutuza, V. Yargeau, and T. Szkopek, "Selective ion sensing with high resolution large area graphene field effect transistor arrays," *Nature Communications*, vol. 11, pp. 1–12, June 2020.

[66] X. Duan, Y. Li, N. K. Rajan, D. A. Routenberg, Y. Modis, and M. A. Reed, "Quantification of the affinities and kinetics of protein interactions using silicon nanowire biosensors," *Nature Nanotechnology*, vol. 7, pp. 401–407, May 2012.

[67] N. K. Rajan, D. A. Routenberg, and M. A. Reed, "Optimal signal-to-noise ratio for silicon nanowire biochemical sensors," *Applied Physics Letters*, vol. 98, no. 26, p. 264107, 2011.

[68] N. K. Rajan, K. Brower, X. Duan, and M. A. Reed, "Limit of detection of field effect transistor biosensors: Effects of surface modification and size dependence," *Applied Physics Letters*, vol. 104, no. 8, p. 084106, 2014.

[69] T. Rim, K. Kim, H. Cho, W. Jeong, J.-S. Yoon, Y. Kim, M. Meyyappan, and C.-K. Baek, "Electrical characteristics of doped silicon nanowire channel field-effect transistor biosensors," *IEEE Sensors Journal*, vol. 17, pp. 667–673, Dec. 2016.

[70] O. Knopfmacher, A. Tarasov, W. Fu, M. Wipf, B. Niesen, M. Calame, and C. Schönenberger, "Nernst limit in dual-gated Si-nanowire FET sensors," *Nano Letters*, vol. 10, pp. 2268–2274, June 2010.

[71] R. A. Chapman, P. G. Fernandes, O. Seitz, O. Seitz, H. J. Stiegler, H.-C. Wen, Y. J. Chabal, and E. M. Vogel, "Comparison of methods to bias fully depleted SOI-based MOSFET nanoribbon pH sensors," *IEEE Transactions on Electron Devices*, vol. 58, pp. 1752–1760, June 2011.

[72] J.-H. Ahn, B. Choi, and S.-J. Choi, "Understanding the signal amplification in dual-gate FET-based biosensors," *Journal of Applied Physics*, vol. 128, p. 184502, Nov. 2020.

[73] J. Go, P. R. Nair, and M. A. Alam, "Theory of signal and noise in double-gated nanoscale electronic pH sensors," *Journal of Applied Physics*, vol. 112, no. 3, p. 034516, 2012.

[74] T. Wu, A. Alharbi, K.-D. You, K. Kisslinger, E. A. Stach, and D. Shahrjerdi, "Experimental study of the detection limit in dual-gate biosensors using ultrathin silicon transistors," *ACS Nano*, vol. 11, no. 7, pp. 7142–7147, 2017.

[75] A. Tarasov, W. Fu, O. Knopfmacher, J. Brunner, M. Calame, and C. Schönenberger, "Signal-to-noise ratio in dual-gated silicon nanoribbon field-effect sensors," *Applied Physics Letters*, vol. 98, no. 1, p. 012114, 2011.

[76] K. Bedner, V. A. Guzenko, A. Tarasov, M. Wipf, R. L. Stoop, S. Rigante, J. Brunner, W. Fu, C. David, M. Calame, J. Gobrecht, and C. Schönenberger, "Investigation of the dominant 1/f noise source in silicon nanowire sensors," *Sensors and Actuators B: Chemical*, vol. 191, pp. 270–275, 2014.

[77] C. Jakobson and Y. Nemirovsky, "1/f noise in ion sensitive field effect transistors from subthreshold to saturation," *IEEE Transactions on Electron Devices*, vol. 46, no. 1, pp. 259–261, 1999.

[78] W. Henrion, M. Rebien, H. Angermann, and A. Röseler, "Spectroscopic investigations of hydrogen termination, oxide coverage, roughness, and surface state density of silicon during native oxidation in air," *Applied Surface Science*, vol. 202, pp. 199 –205, Dec. 2002.

[79] R. Jayaraman and C. G. Sodini, "A 1/f noise technique to extract the oxide trap density near the conduction band edge of silicon," *IEEE Transactions on Electron Devices*, vol. 36, no. 9, pp. 1773–1782, 1989.

[80] J. Diot, J. Joseph, J. Martin, and P. Clechet, "pH dependence of the Si/SiO2 interface state density for EOS systems: Quasi-static and AC conductance methods," *Journal of Electroanalytical Chemistry and Interfacial Electrochemistry*, vol. 193, pp. 75–88, Oct. 1985.

[81] S. Kalra, M. J. Kumar, and A. Dhawan, "Schottky Barrier FET Biosensor for Dual Polarity Detection: A Simulation Study," *IEEE Electron Device Letters*, vol. 38, pp. 1594–1597, Nov. 2017.

[82] K.-S. Shin, K. Lee, J.-H. Park, J. Y. Kang, and C. O. Chui, "Schottky contacted nanowire field-effect sensing device with intrinsic amplification," *IEEE Electron Device Letters*, vol. 31, no. 11, pp. 1317–1319, 2010.

[83] W. Liao, W. Wei, Y. Tong, A. Wong, W. K. Chim, and C. Zhu, "pH sensing and low-frequency noise characteristics of low temperature (400 c) p-channel SOI Schottky ISFETs," *IEEE Electron Device Letters*, vol. 38, no. 8, pp. 1146–1149, 2017.

[84] McWhorter and A. Louis, *1/f noise and related surface effects in germanium*. PhD thesis, Massachusetts Institute of Technology, 1955.

[85] E. Simoen, A. Mercha, C. Claeys, N. Lukyanchikova, and N. Garbar, "Critical discussion of the front-back gate coupling effect on the low-frequency noise in fully depleted SOI MOSFETs," *IEEE Transactions on Electron Devices*, vol. 51, no. 6, pp. 1008–1016, 2004.

[86] G. Petiau and A. Dupis, "Noise, temperature coefficient, and long time stability of electrodes for telluric observations," *Geophysical Prospecting*, vol. 28, no. 5, pp. 792–804, 1980.

[87] A. Hassibi, R. Navid, R. W. Dutton, and T. H. Lee, "Comprehensive study of noise processes in electrode electrolyte interfaces," *Journal of Applied Physics*, vol. 96, no. 2, pp. 1074–1082, 2004.

[88] K. Radulović, I. Jokić, M. Frantlović, and Z. Djurić, "Adsorption-desorption noise in nanowire fet biosensors," in *2012 28th International Conference on Microelectronics Proceedings*, pp. 203–206, IEEE, 2012.

[89] G. Zheng, X. P. Gao, and C. M. Lieber, "Frequency domain detection of biomolecules using silicon nanowire biosensors," *Nano Letters*, vol. 10, no. 8, pp. 3179–3183, 2010.

[90] K. Georgakopoulou, A. Birbas, and C. Spathis, "Modeling of fluctuation processes on the biochemically sensorial surface of silicon nanowire field-effect transistors," *Journal of Applied Physics*, vol. 117, p. 104505, Mar. 2015.

[91] Q. Guo, T. Kong, R. Su, Q. Zhang, and G. Cheng, "Noise spectroscopy as an equilibrium analysis tool for highly sensitive electrical biosensing," *Applied Physics Letters*, vol. 101, no. 9, p. 093704, 2012.

[92] S. Kim, T. Rim, K. Kim, U. Lee, E. Baek, H. Lee, C.-K. Baek, M. Meyyappan, M. J. Deen, and J.-S. Lee, "Silicon nanowire ion sensitive field effect transistor with integrated Ag/AgCl electrode: pH sensing and noise characteristics," *Analyst*, vol. 136, no. 23, pp. 5012–5016, 2011.

[93] N. Clément, K. Nishiguchi, J. Dufreche, D. Guerin, A. Fujiwara, and D. Vuillaume, "A silicon nanowire ion-sensitive field-effect transistor with elementary charge sensitivity," *Applied Physics Letters*, vol. 98, no. 1, p. 014104, 2011.

[94] Y. Nemirovsky, I. Brouk, and C. G. Jakobson, "1/f noise in cmos transistors for analog applications," *IEEE Transactions on Electron Devices*, vol. 48, no. 5, pp. 921–927, 2001.

[95] M. Crescentini, M. Bennati, M. Carminati, and M. Tartagni, "Noise limits of cmos current interfaces for biosensors: a review," *IEEE Transactions on Biomedical Circuits and Systems*, vol. 8, pp. 278–292, Apr. 2014.

[96] G. Ghibaudo, O. Roux, C. Nguyen-Duc, F. Balestra, and J. Brini, "Improved analysis of low frequency noise in field-effect MOS transistors," *Physica Status Solidi (a)*, vol. 124, pp. 571–581, Apr. 1991.

[97] N. Clément, G. Larrieu, and E. Dubois, "Low-frequency noise in Schottky-barrier-based nanoscale field-effect transistors," *IEEE Transactions on Electron Devices*, vol. 59, pp. 180–187, Jan. 2012.

[98] L. Mu, Y. Chang, S. D. Sawtelle, M. Wipf, X. Duan, and M. A. Reed, "Silicon nanowire field-effect transistors—a versatile class of potentiometric nanobiosensors," *IEEE Access*, vol. 3, pp. 287–302, 2015.

[99] A. Elyasi, M. Fouladian, and S. Jamasb, "Counteracting Threshold-Voltage Drift in Ion-Selective Field Effect Transistors (ISFETs) Using Threshold-Setting Ion Implantation," *IEEE Journal of the Electron Devices Society*, vol. 6, p. 747–754, Jan 2018.

[100] S. Jamasb, S. Collins, and R. L. Smith, "A physical model for drift in pH ISFETs," *Sensors and Actuators B: Chemical*, vol. 49, no. 1-2, pp. 146–155, 1998.

[101] P. Fernandes, O. Seitz, R. Chapman, H. Stiegler, H.-C. Wen, Y. Chabal, and E. Vogel, "Effect of mobile ions on ultrathin silicon-on-insulator-based sensors," *Applied Physics Letters*, vol. 97, no. 3, p. 034103, 2010.

[102] D. W. Kwon, S. Kim, R. Lee, H.-S. Mo, D. H. Kim, and B.-G. Park, "Macro modeling of ion sensitive field effect transistor with current drift," *Sensors and Actuators B: Chemical*, vol. 249, pp. 564–570, 2017.

[103] S. Kim, D. W. Kwon, S. Kim, R. Lee, T.-H. Kim, H.-S. Mo, D. H. Kim, and B.-G. Park, "Analysis of current drift on p-channel pH-Sensitive SiNW ISFET by capacitance measurement," *Current Applied Physics*, vol. 18, pp. S68–S74, 2018.

[104] C. Jakobson, M. Feinsod, and Y. Nemirovsky, "Low frequency noise and drift in ion sensitive field effect transistors," *Sensors and Actuators B: Chemical*, vol. 68, no. 1-3, pp. 134–139, 2000.

[105] S. Chen, L. Nyholm, N. Jokilaakso, A. E. Karlström, J. Linnros, U. Smith, and S.-L. Zhang, "Current instability for silicon nanowire field-effect sensors operating in electrolyte with platinum gate electrodes," *Electrochemical and Solid-state Letters*, vol. 14, no. 7, pp. J34–J37, 2011.

[106] A. Baldi, A. Bratov, R. Mas, and C. Dominguez, "Electrostatic discharge sensitivity tests for isfet sensors," *Sensors and Actuators B: Chemical*, vol. 80, no. 3, p. 255–260, 2001.

[107] H. Jang, J. Lee, J. H. Lee, S. Seo, B.-G. Park, D. M. Kim, D. H. Kim, and I.-Y. Chung, "Analysis of hysteresis characteristics of silicon nanowire biosensors in aqueous environment," *Applied Physics Letters*, vol. 99, no. 25, p. 252103, 2011.

[108] T. Kong, R. Su, B. Zhang, Q. Zhang, and G. Cheng, "CMOS-compatible, label-free silicon-nanowire biosensors to detect cardiac troponin I for acute myocardial infarction diagnosis," *Biosensors and Bioelectronics*, vol. 34, no. 1, pp. 267–272, 2012.

[109] G. Shalev, G. Landman, I. Amit, Y. Rosenwaks, and I. Levy, "Specific and label-free femtomolar biomarker detection with an electrostatically formed nanowire biosensor," *NPG Asia Materials*, vol. 5, no. 3, p. e41, 2013.

[110] S. Jamasb, "An analytical technique for counteracting drift in ion-selective field effect transistors (isfets)," *IEEE Sensors Journal*, vol. 4, p. 795–801, Dec 2004.

[111] D. Welch, S. Shah, S. Ozev, and J. B. Christen, "Experimental and simulated cycling of isfet electric fields for drift reset," *IEEE Electron Device Letters*, vol. 34, no. 3, p. 456–458, 2013.

[112] A. Errachid, J. Bausells, and N. Jaffrezic-Renault, "A simple REFET for pH detection in differential mode," *Sensors and Actuators B: Chemical*, vol. 60, no. 1, p. 43–48, 1999.

[113] M. Wipf, R. L. Stoop, A. Tarasov, K. Bedner, W. Fu, I. A. Wright, C. J. Martin, E. C. Constable, M. Calame, and C. Schönenberger, "Selective sodium sensing with gold-coated silicon nanowire field-Effect transistors in a differential setup," *ACS Nano*, vol. 7, p. 5978–5983, Jul 2013.

[114] Ó. Gutiérrez-Sanz, N. Haustein, M. Schroeter, T. Oelschlaegel, M. S. Filipiak, and A. Tarasov, "Transistor-based immunosensing in human serum samples without on-site calibration," *Sensors and Actuators B: Chemical*, vol. 295, p. 153–158, 2019.

[115] N. M. Hemed, A. Inberg, and Y. Shacham-Diamand, "On the stability of silicon field effect capacitors with phosphate buffered saline electrolytic gate and self assembled monolayer gate insulator," *Electrochimica Acta*, vol. 111, p. 720–728, 2013.

[116] E. A. Schiff, "Trap-controlled dispersive transport and exponential band tails in amorphous silicon," *Physical Review B*, vol. 24, no. 10, p. 6189–6192, 1981.

[117] A. I. Rudenko and V. I. Arkhipov, "Drift and diffusion in materials with traps," *Philosophical Magazine Part B*, vol. 45, no. 2, p. 177–187, 1982.

[118] J. Kakalios, R. A. Street, and W. B. Jackson, "Stretched-exponential relaxation arising from dispersive diffusion of hydrogen in amorphous silicon," *Physical Review Letters*, vol. 59, p. 1037–1040, Aug 1987.

[119] S. Jamasb, S. D. Collins, and R. L. Smith, "A physical model for threshold voltage instability in si/sub 3/n/sub 4/-gate h/sup+/-sensitive fet's (ph isfet's)," *IEEE Transactions on Electron Devices*, vol. 45, no. 6, pp. 1239–1245, 1998.

[120] A.-M. El-Sayed, Y. Wimmer, W. Goes, T. Grasser, V. V. Afanas' ev, and A. L. Shluger, "Theoretical models of hydrogen-induced defects in amorphous silicon dioxide," *Physical Review B*, vol. 92, no. 1, p. 014107, 2015.

[121] K. H. Beckmann and N. J. Harrick, "Hydrides and hydroxyls in thin silicon dioxide films," *Journal of The Electrochemical Society*, vol. 118, no. 4, p. 614, 1971.

[122] J. Z. Xie, S. P. Murarka, X. S. Guo, and W. A. Lanford, "Hydrogen concentration profiles in as-deposited and annealed phosphorus-doped silicon dioxide films," *Applied Physics Letters*, vol. 53, no. 21, p. 2036–2038, 1988.

[123] A. Marwick and D. Young, "Measurements of hydrogen in metal-oxide-semiconductor structures using nuclear reaction profiling," *Journal of Applied Physics*, vol. 63, no. 7, pp. 2291–2298, 1988.

[124] F. B. McLean and G. Ausman Jr, "Simple approximate solutions to continuous-time random-walk transport," *Physical Review B*, vol. 15, no. 2, p. 1052, 1977.

[125] J. Kakalios, R. Street, and W. Jackson, "Stretched-exponential relaxation arising from dispersive diffusion of hydrogen in amorphous silicon," *Physical Review Letters*, vol. 59, no. 9, p. 1037, 1987.

[126] T. Grasser, W. Gos, and B. Kaczer, "Dispersive transport and negative bias temperature instability: Boundary conditions, initial conditions, and transport models," *IEEE Transactions on Device and Materials Reliability*, vol. 8, no. 1, pp. 79–97, 2008.

[127] T. D. Pollard, "A guide to simple and informative binding assays," *Molecular Biology of the Cell*, vol. 21, no. 23, pp. 4061–4067, 2010.

[128] R. Lefkowitz, J. Roth, and I. Pastan, "Radioreceptor assay of adrenocorticotropic hormone: new approach to assay of polypeptide hormones in plasma," *Science*, vol. 170, no. 3958, pp. 633–635, 1970.

[129] A. Vieira, "ELISA-based assay for scatchard analysis of ligand-receptor interactions," *Molecular biotechnology*, vol. 10, no. 3, pp. 247–250, 1998.

[130] K. Stenroos, P. Hurskainen, S. Eriksson, I. Hemmilä, K. Blomberg, and C. Lindqvist, "Homogeneous time-resolved IL-2-IL-2Rα assay using fluorescence resonance energy transfer," *Cytokine*, vol. 10, no. 7, pp. 495–499, 1998.

[131] U. Jönsson, L. Fägerstam, B. Ivarsson, B. Johnsson, R. Karlsson, K. Lundh, S. Löfås, B. Persson, H. Roos, and I. Rönnberg, "Real-time biospecific interaction analysis using surface plasmon resonance and a sensor chip technology," *Biotechniques*, vol. 11, no. 5, pp. 620–627, 1991.

[132] Y. Mao, K.-S. Shin, X. Wang, Z. Ji, H. Meng, and C. O. Chui, "Semiconductor electronic label-free assay for predictive toxicology," *Scientific Reports*, vol. 6, p. 24982, Apr 2016.

[133] B. R. Dorvel, B. Reddy Jr, J. Go, C. Duarte Guevara, E. Salm, M. A. Alam, and R. Bashir, "Silicon nanowires with high-k hafnium oxide dielectrics for sensitive detection of small nucleic acid oligomers," *ACS Nano*, vol. 6, no. 7, pp. 6150–6164, 2012.

[134] A. Gao, N. Lu, Y. Wang, P. Dai, T. Li, X. Gao, Y. Wang, and C. Fan, "Enhanced sensing of nucleic acids with silicon nanowire field effect transistor biosensors," *Nano Letters*, vol. 12, no. 10, pp. 5262–5268, 2012.

[135] K. Maehashi, T. Katsura, K. Kerman, Y. Takamura, K. Matsumoto, and E. Tamiya, "Label-free protein biosensor based on aptamer-modified carbon nanotube field-effect transistors," *Analytical Chemistry*, vol. 79, no. 2, pp. 782–787, 2007.

[136] B. Wunderlich, P. Neff, and A. Bausch, "Mechanism and sensitivity of the intrinsic charge detection of biomolecular interactions by field effect devices," *Applied Physics Letters*, vol. 91, no. 8, p. 83904, 2007.

[137] W. McKinnon, D. Landheer, and G. Aers, "Sensitivity of field-effect biosensors to charge, pH, and ion concentration in a membrane model," *Journal of Applied Physics*, vol. 104, no. 12, p. 124701, 2008.

[138] X. Duan, Y. Li, N. K. Rajan, D. A. Routenberg, Y. Modis, and M. A. Reed, "Quantification of the affinities and kinetics of protein interactions using silicon nanowire biosensors," *Nature Nanotechnology*, vol. 7, no. 6, p. 401, 2012.

[139] M. Wipf, R. L. Stoop, G. Navarra, S. Rabbani, B. Ernst, K. Bedner, C. Schönenberger, and M. Calame, "Label-Free FimH protein interaction analysis using silicon nanoribbon bioFETs," *ACS Sensors*, vol. 1, no. 6, pp. 781–788, 2016.

[140] N. Hong, C. Park, D. Kim, K.-S. Jeong, J.-S. Yoon, B. Jin, M. Meyyappan, and J.-S. Lee, "Buffer effects of two functional groups against pH variation at aminosilanized Electrolyte-Oxide-Semiconductor (EOS) capacitor," *Sensors and Actuators B: Chemical*, vol. 242, pp. 324–331, 2017.